

Low Sweep Transonic Wing Design

by Implementing Shock Control Bumps using Multidisciplinary Design Optimization

Bram Timmer

Low Sweep Transonic Wing Design

by Implementing Shock Control Bumps using Multidisciplinary Design Optimization

by

Bram Timmer

in partial fulfilment of the requirements for the degree of

Master of Science
in Aerospace Engineering

at the Delft University of Technology.

Supervisor:	Dr. A. Elham
Thesis committee:	Prof. dr. ir. L.L.M. Veldhuis Dr. R.P. Dwight

Date:	24-11-2016
Thesis registration number:	095#16#MT#FPP
Student number:	4019601

An electronic version of this thesis is available at <http://repository.tudelft.nl/>.

Summary

The goal of this thesis is to assess the feasibility of using the wave drag reduction properties of the shock control bump concept to reduce the sweep angle of a transonic wing while maintaining its original flight conditions. This will be done by performing a multi-disciplinary design optimization on a transonic wing design with the minimization of the associated maximum take-off weight as the objective function. For this optimization, the sweep angle, angle of attack, and shock control bump shape parameters are defined as design variables and the reference flight conditions are set as constraints. Ultimately, greater understanding of the potential of the shock control bump concept will be gained while also contributing to the on-going efforts towards reducing the greenhouse gasses produced by the aerospace industry.

For the aerodynamic analysis, the tool SU² is used. SU², short for Stanford University Unstructured, determines the flow properties of a given mesh under specified flow conditions. This tool is used to solve the Euler equations for the flow, compared to solving the Reynolds-averaged Navier-Stokes equations this offers a significant decrease in computational cost at only a marginal cost in accuracy of the results. The loss in accuracy is only minor as the viscous drag, which is not accounted for in the Euler equations, can be assumed constant and the change in friction drag due to the addition of the shock control bump is minimal. Additionally, the software has a continuous adjoint solver build-in which is capable of determining the sensitivity information of the model at relatively low computational cost when compared to using the finite difference method. This information can be used for shape optimization and to this purpose the tool also utilizes the Free-Form Deformation parameterization technique to allow the deformation of the original mesh based on the sensitivity information.

The structural analysis tool EMWET is used to estimate the wing weight. EMWET, which stands for Elham Modified Weight Estimation Tool, estimates the wing structural weight using equivalent panel thicknesses and empirical data. The loads acting on the wing are determined using the tool AVL in a quasi-three-dimensional approach. The weight of the structure for a given load case is based on the summation of the equivalent panel weight and empirical data. The load case considered in this research is a 2.5g pull-up manoeuvre, which is assumed to be the critical load case.

The performance analysis determines the total fuel weight by using the Breguet range equation. In order to determine the fuel weight, the total flight mission is split into seven distinct phases which each have their own mass fraction. The mass fractions are constant for all phases except the cruise phase, the mass fraction for the cruise phase is determined using the Breguet range equation. This approach includes both the aerodynamic performance of the design, as the only varying parameter in the range equation is the lift-to-drag ratio, as well as the associated MTOW (and thus the wing structural weight), as the fuel weight is a fraction of the MTOW.

A series of gradient-based optimization are performed using the build-in Sequential Quadratic Programming algorithm in the MATLAB function *fmincon*. The optimization is set-up according to the Individual Design Feasible architecture which utilizes surrogate variable to decouple the disciplines, increasing the convergence rate of the process. The objective function is the surrogate variable for the MTOW. The design vector consists of the surrogate variables for MTOW and fuel weight, sweep angle, angle of attack, and the shock control bump shape variables. The bump shape variables are bound such that no thinning of the wing can occur. Additionally, the design constraints are set such that the drag coefficient is equal to, or lesser than, the original drag coefficient and the generated lift is equal to the design weight in order to ensure steady horizontal flight at the design point. Lastly, the surrogate variables are each accompanied by consistency constraints which state that they are equal to their respective counterpart.

The results showed that the used geometry parameterization is capable of successfully producing both 3-D and 2-D bump shapes. This was done by excluding the sweep variable from the optimizations definition, hence optimizing purely for bump shapes, and the largest contributor to the maximum take-off weight reduction of 1.2% is the fuel weight reduction of 4.2%. When including the sweep variable in the definition of a single-point optimization, the sweep angle was reduced such that the optimized wing had a straight leading edge. This resulted in a 3.1% reduction in objective function, where the wing structural weight was the dominant factor with over 20% weight reduction. By running a similar optimization with a fixed sweep angle reduction, it was shown that a fixed reduction shows improved bump placement at a higher optimization efficacy while the resulting weight reductions are similar. Ultimately, a multi-point variant of the variable sweep optimization showed that, when considering a range of design points, the sweep angle was reduced by a more realistic 11 degrees. This resulted in a maximum take-off weight reduction of 1.24%. It is suggested that the lowest considered lift coefficient was driving in the lower reduction in wing sweep. Lastly, in this research the 2-D shapes outperformed the 3-D shapes for all single-point cases, in contrast to what is found in literature. It is concluded that this is likely due to restrictions in potential shapes for the 3-D designs.

Preface

This master thesis was accomplished within the faculty of aerospace engineering at the Technical University of Delft. For this thesis, an optimization is set-up to design a low sweep transonic wing using the concept of shock control bumps to reduce the associated increase in wave drag. The optimization provides an indication of the weight reduction that can be achieved by applying shock control bumps to unlock, and reduce, the sweep angle of the wing as a design variable, while maintaining the original cruise flight conditions.

This thesis would not have been possible without the guidance of Dr. A. Elham whose knowledge of the different aspects involved never ceased to amaze me. The assistance and support from my friends, family, and girlfriend were, of course, also paramount in helping me write this thesis. Hence, I would like to thank all of them dearly.

*Bram Timmer
Delft, November 2016*

Contents

Summary	i
Preface	iii
List of Figures	vii
List of Tables	ix
Nomenclature	xi
1 Introduction	1
1.1 The Shock Control Bump	2
1.1.1 Historical Background	2
1.1.2 Working Principle	2
1.1.3 Geometry	3
1.1.4 Basic Flow Physics	3
1.1.5 Performance	4
1.2 Prior Efforts in Low Sweep Wing Design using Shock Control Bumps	4
1.3 Research Objective	5
1.4 Thesis Outline	6
2 Aerodynamic Analysis	9
2.1 Stanford University Unstructured Computational Fluid Dynamics	9
2.2 Geometry Parameterization: Free-Form Deformation	10
2.3 Sensitivity Analysis: Continuous Adjoint Method	14
3 Structural Analysis	19
3.1 Elham Modified Weight Estimation Technique	19
3.2 Load Determination	19
3.3 Validation of EMWET	19
3.4 Application	20
4 Performance Analysis	23
4.1 Mass Fractions Method and the Breguet Range Equation	23
4.2 Design Point Weight	24
4.3 Fuel Weight	25
4.4 Sensitivity Analysis: Automatic Differentiation	26
5 Optimization Setup	29
5.1 Multi-disciplinary Design Optimization Architectures	29
5.1.1 All-At-Once	29
5.1.2 Simultaneous Analysis and Design	32
5.1.3 Individual Discipline Feasible	32
5.1.4 Multi-Disciplinary Feasible	33
5.2 Optimization Problem Formulation	34
5.2.1 Architecture Choice	35
5.2.2 Mathematical Definition	35
5.2.3 Objective Function	35
5.2.4 Design Variables	36

5.2.5 Design Constraints	37
5.2.6 Consistency Constraints.....	37
5.2.7 Extended Design Structure Matrix	38
5.2.8 Optimizer	38
5.3 Sensitivity Analysis	40
6 Test Case Application	43
6.1 Test Case Aircraft.....	43
6.1.1 Aircraft Characteristics	43
6.1.2 Baseline Wing.....	43
6.1.3 Wing box Dimensions	44
6.1.4 Surface & Volume Mesh	45
6.2 Optimization Formulations	46
6.2.1 Shock Control Bump Shape Optimization	46
6.2.2 Single-point Low Sweep Design Optimizations.....	47
6.2.3 Multi-point Low Sweep Design Optimization	48
6.3 Optimization Results	48
6.3.1 Shock Control Bump Shape Optimizations.....	48
6.3.2 Variable Sweep Optimizations	53
6.3.3 Fixed Sweep Optimizations.....	56
6.3.4 Multi-Point Low Sweep Design Optimization	59
7 Conclusions and Recommendations	65
7.1 Conclusions	65
7.2 Recommendations	67
References	69

List of Figures

Figure 1.1: Illustration of the snowball effect.....	1
Figure 1.2 Illustration of the different shock structures produced by a SCB: (a) Shock created in the uncontrolled case, source: Bruce & Colliss [6]; (b) compression waves produced by a smooth contour-shaped bump, source: Birkemeyer, et al. [27]; (c) λ -shock structure produced by a wedge-shaped bump, source: Ogawa & Babinsky [28].	3
Figure 1.3: Illustration of different SCB configurations on a wing: (left) continuous 2-D SCB; (right) array of 3-D SCBs. Source: Bruce & Colliss [6]	3
Figure 1.4: Low sweep wing without (left) and with (right) an array of optimized 3-D SCBs. Source: Qin [32]	4
Figure 1.5: Illustration of lowering of the sweep angle by an array of optimized 3-D SCBs. Reproduced from Deng, et al., [33].	5
Figure 1.6: Lift coefficient vs. angle of attack at Mach 0.2. Source: Deng, et al., [33].	5
Figure 2.1: From sphere to blended wing body using the FFD method. Reproduced from Gagnon & Zingg [59].	11
Figure 2.2: Initial and deformed surfaces. Source: Gagnon & Zingg [59]	11
Figure 2.3: Initial and deformed grid using a grid-point-based method. Source: Gagnon & Zingg [41]	11
Figure 2.4: Initial and deformed grid using the spring-based volume movement method. Source: Palacios et al. [43]	12
Figure 2.5: Top view of the planform FFD box.	12
Figure 2.6: Deformation using the planform FFD box.	12
Figure 2.7: Illustration of the SCB box control point layout (top) and example 3-D SCBs (middle) and 2-D SCB (bottom) shapes.	13
Figure 2.8: Top view of all 20 SCB boxes, only corner control points are shown.	13
Figure 2.9: Illustration of the mesh adjoint method. Source: Zhu & Qin [44]	14
Figure 3.1: EMWET validation. Source: [47].	20
Figure 4.1: Typical mission profile for a commercial transonic passenger aircraft.	23
Figure 5.1: XDSM of the AAO architecture. Source: Martins & Lambe [51]	31
Figure 5.2: XDSM of the SAND architecture. Source: Martins & Lambe [51]	32
Figure 5.3: XDSM of the IDF architecture. Source: Martins & Lambe [51].	33
Figure 5.4: XDSM of the MDF architecture, reproduced from Martins & Lambe [51].	34
Figure 5.5: XDSM of the MTOW optimization as used for this research.	38
Figure 6.1: Planform of the reference A320 wing, dimensions in meter.	44
Figure 6.2: Airfoil shapes of the reference A320 wing at four spanwise stations.	44
Figure 6.3: Illustration of the volume mesh, dimensions in meter.	45
Figure 6.4: Cross-section of the volume mesh at the root.	45
Figure 6.5: Cross-section of the volume mesh at the tip.	45
Figure 6.6: Top view of the upper surface mesh.	46
Figure 6.7: Bottom view of the lower surface mesh.	46
Figure 6.8: Side view of the tip surface mesh.	46
Figure 6.9: Load distribution for the baseline, 2-D SCB, and 3-D SCB wings from the SCB shape optimizations.	50
Figure 6.10: Mach-distributions of the initial and optimized designs from the SCB shape optimizations.	50
Figure 6.11: Performance of the initial and optimized designs from the SCB shape optimizations.	51
Figure 6.12: Performance near the design lift coefficient of the initial and optimized designs from the SCB shape optimizations.	51
Figure 6.13: Pressure distributions (bottom), airfoil shapes (middle), and SCB shapes (top) for the baseline, 3-D SCBs, and 2-D SCB wings, from the SCB shape optimizations at four spanwise sections.	52

Figure 6.14: Load distribution for the baseline, straight, 2-D SCB, and 3-D SCB wings from the variable sweep optimizations.	54
Figure 6.15: Pressure distributions (bottom), airfoil shapes (middle), and SCB shapes (top) for the straight, 3-D SCBs, and 2-D SCB wings from the variable sweep optimization at four spanwise sections.	55
Figure 6.16: Mach-distributions of the variable sweep wings.	56
Figure 6.17: Mach distributions of the fixed sweep wings.	56
Figure 6.18: Pressure distributions (bottom), airfoil shapes (middle), and SCB shapes (top) for the straight, 3-D SCBs, and 2-D SCB wings from the fixed sweep optimization at four spanwise sections.	58
Figure 6.19: Performance of the various designs related to the sweep optimizations.	59
Figure 6.20: Performance near the design lift coefficient of the various designs related to the sweep optimizations.	59
Figure 6.21: Mach distributions of the optimized multi-point wing, with and without SCBs.....	61
Figure 6.22: Performance of the initial and optimized designs from the multi-point optimizations.	61
Figure 6.23: Performance near the design lift coefficients of the initial and optimized designs from the multi-point optimizations.....	61
Figure 6.24: Airfoil (bottom) and SCB (top) shapes for the initial and optimized designs from the multi-point optimization.	63
Figure 6.25: Pressure distributions for the sweep only wing, and the optimized wing at the three design points, for four spanwise sections.	63

List of Tables

Table 2.1: Verification of the continuous adjoint sensitivities.	16
Table 3.1: EMWET validation data. [47].....	20
Table 4.1: Flight phases and their respective mass fractions. [49]	24
Table 4.2: Verification of the automatic differentiation sensitivities.	26
Table 6.1: Characteristics of the Airbus A320. [63] [64]	43
Table 6.2: Geometric definition of the A320 wing. [63]	44
Table 6.3: CST coefficients defining the airfoil shapes at four span-wise stations.	44
Table 6.4: Chord-wise position of the front and rear spar.	45
Table 6.5: Convergence results for the 2-D SCB shape optimization.	49
Table 6.6: Convergence results for the 3-D SCBs shape optimization.....	49
Table 6.7: Characteristics of the initial and optimized designs from the SCB shape optimizations.	49
Table 6.8: Convergence results for the 2-D SCB variable sweep optimization.....	53
Table 6.9: Convergence results for the 3-D SCBs variable sweep optimization.	53
Table 6.10: Characteristics of the initial and optimized designs from the variable sweep optimizations.	53
Table 6.11: Convergence results for the 2-D SCB fixed sweep optimization.	56
Table 6.12: Convergence results for the 3-D SCB fixed sweep optimization.	56
Table 6.13: Characteristics of the optimized designs from the variable and fixed sweep optimizations.	57
Table 6.14: Convergence results for the multi-point optimization.	59
Table 6.15: Characteristics of the initial and optimized design from the multi-point optimization.	60

Nomenclature

Latin Symbols

Variable	Description	Unit
C	Inequality constraint	[-]
C^c	Equality/consistency constraint	[-]
C_D	Total drag coefficient	[-]
C_{D_f}	Friction drag component coefficient	[-]
C_{D_r}	Rest drag component coefficient	[-]
C_{D_w}	Wave drag component coefficient	[-]
C_L	Total lift coefficient	[-]
C_D^W	Wing drag coefficient	[-]
C_L^W	Wing lift coefficient	[-]
D	Total drag force	[N]
e_{ij}	Unit vector in the direction that connects node i and j	[]
F	Objective function	[-]
$f_{5,n}$	Fuel fraction component n of the cruise phase	[-]
f_i	Fuel fraction for phase i	[-]
$f_{reserve}$	Reserve fuel fraction	[-]
f_{total}	Total fuel fraction (excluding reserve fuel)	[-]
h_{cr}	Cruise Altitude	[m]
K_{ij}	Stiffness matrix	[]
L	Auxiliary Lagrangian function	[-]
L	Total lift force	[N]
M	Mach number	[-]
M_{cr}	Cruise Mach number	[-]
$N(i)$	Set of neighboring points to node i	[-]
n_D	Number of design points	[-]
p	Pressure	[]
R	Aircraft cruise range	[m]
R_i	Residuals of discipline i	[-]
SFC	Specific fuel consumption	[g/N · s]
S_{wing}	Wing wetted surface area	[m ²]
u_i	Volume mesh displacement at node i	[]
u_j	Surface displacement at node j	[]
V_{cr}	Cruise velocity	[m/s]
W_{a-w}	Weight of aircraft minus fuel and wing weight	[N]
W_{D_n}	Design weight at point n	[N]
W_F	Fuel weight	[N]
W_M	MTOW	[N]
W_W	Wing structural weight	[N]
X	Design variables vector	[-]
Y	State variables vector	[-]

Greek Symbols

Variable	Description	Unit
α	Angle of attack	[deg]
η	Spanwise position	[-]
Λ	Sweep angle	[deg]
ρ	Density of air	[kg/m ³]

1

Introduction

Modern commercial civil air transport operates in the transonic flight speed regime as it is still infeasible, from a fuel economy standpoint, to operate in the supersonic speed regime. In the transonic regime, the efficiency of aero-engines increases for increasing flight speeds. However, when increasing the flight speed, eventually shock waves will start to form on the upper surface of the wing and these shock waves generate a significant amount of wave drag. Above a certain flight speed, the drag divergence Mach number, the strength of these shock waves will increase rapidly with increasing Mach number. This will eventually result in boundary layer separation and stall, effectively constraining the flight boundaries of the aircraft.

The conventional approach to satisfying the need for flying at high transonic Mach numbers is to consider a swept and thin wing design, as these characteristics delay the drag divergence Mach number. However, large sweep angles and thin airfoils affect the wing structure negatively. Satisfying structural requirements - such as aileron effectiveness and flutter - for highly swept thin wings will result in a huge weight penalty [1], which adversely affects the overall aircraft performance. Some designs have been suggested with low sweep and relatively high thickness, but these alternative solutions come at the price of a reduced cruise Mach number; reducing the cruise Mach number has a negative effect on the direct operating cost (DOC) of the aircraft. [2]

In order to further improve the aircraft performance under the previously mentioned limitations, while also considering the increasingly strict requirements on the environmental impact of aircraft due to the increasing awareness of global warming [3] [4], it may be beneficial to look towards novel or alternative design solutions for existing challenges. One such concept is the so-called Shock Control Bump (SCB). The SCB is a form of shock control which, under appropriate circumstances, can significantly reduce the wave drag on an aerodynamic surface experiencing strong shockwaves, e.g. the upper surface of a transonic wing.

The wave drag reducing property of SCBs has proven to increase the lift-to-drag ratio of a wing or airfoil by a substantial amount, improving the aerodynamic performance. However, it can also be used to counteract the increase in wave drag that would occur when decreasing the sweep angle of an existing wing design, where decreasing the sweep angle will result in a reduction of the wing structural weight. Both these approaches have the potential to reduce the maximum take-off weight (MTOW) of passenger aircraft through the snowball effect, as is illustrated in Figure 1.1. Ultimately, a reduction in MTOW results in a reduction of the DOC [5].

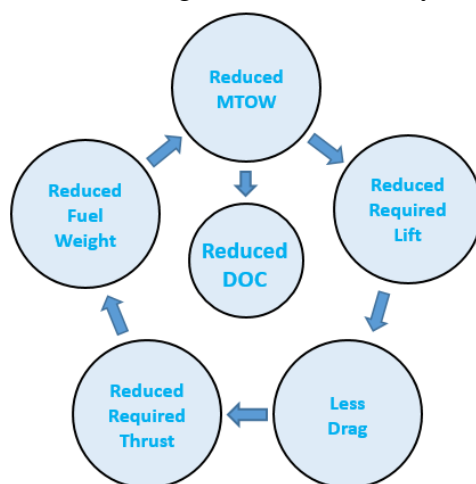


Figure 1.1: Illustration of the snowball effect.

The aim of this thesis is to contribute to the everlasting need of reducing the DOC of commercial civil air transport by optimizing a transonic wing design, with the addition of SCBs, in a multi-disciplinary design optimization (MDO) in which the sweep angle is part of the design vector. The objective of this optimization is to minimize the MTOW while maintaining the flight characteristics of the original wing design. The main novelty of this research is the inclusion of the structural and performance disciplines in the SCB wing design analysis while also considering the multi-disciplinary effects this introduces to the process. Additionally, the sweep variable will be included as a design variable rather than considering a fixed reduction in sweep angle.

1.1 The Shock Control Bump

The SCB is a promising concept for reducing the transonic drag of an aircraft, without increasing the sweep angle and without lowering the flight Mach number. It is a form of shock control and is most commonly used on the top surface of airfoils/wings. This section provides a review of research that has been done on the topic of SCBs up to now, reproducing and building on the extensive review by Bruce & Colliss [6]. It aims to establish what research areas are relevant and what the current understanding is.

First, a short overview of the historical background is given. Then, the working principle is discussed followed by the general geometry. Lastly, the flow physics and the performance of SCBs are covered. The prior efforts combining SCB with low sweep wing design will be discussed in the next section, Section 1.2.

1.1.1 Historical Background

The origin of using a geometrical bump on the upper side of an airfoil for beneficial effect can be traced back to 1977, where Tai [7] investigated a humped transonic airfoil with the aim to increase the drag divergence Mach number and to reduce the effects caused by strong shock waves.

The results from Tai [7] were confirmed in the 1980s by experiments which showed improvements in delaying buffet and increasing the drag divergence Mach number. Additionally, the results also showed potential for significant further improvement in performance. [8]

During the 1990s the first to consider SCBs as a means to reduce wave drag on laminar-flow airfoils were Ashill et al. [9]. Their research inspired major projects in both Europe [10] and the United States [11] to dedicate considerable resources into research focusing on the potential of SCBs.

More recent studies, from the past decade, have successfully confirmed the improved performance that can be facilitated by implementing SCBs. [12] [13] [14] [15] Consequently, over the last decade of research the focus has shifted. In order to optimize the performance and integration in current and future aircraft, the detailed flow physics that SCBs produce have become of greater interest. More specifically, recent computational studies have greatly attributed to the understanding in the form of high quality results [16] [17] and experimental studies have shifted from validation-type research to higher resolution local measurements in the form of more fundamental experiments in carefully controlled environments. [18] [19] [20] Additionally, numerous joint experimental and numerical research papers were published covering the topics of SCB validation and flow physics. [21] [22] [23] [24] [25]

1.1.2 Working Principle

The concept of the SCB consists of placing a bump on top of a flat surface where a normal shock wave would occur, or is expected to occur, in the uncontrolled situation. Hence, the most common application is on the upper surface of an airfoil or wing where strong shock waves are expected to occur and wave drag reductions are desirable. Although less common, significant research has also focused on using SCBs inside the inlets of aero-engines. [16] [26] [27]

The main functionality of SCBs in the application on airfoils or wings is the reduction of wave drag. This is achieved by the beneficial smearing effect they have on the shock wave, where the presence of the bump causes a more isentropic reduction in shock wave strength compared to the uncontrolled case.

1.1.3 Geometry

In general, a distinction is made between a wedge-shaped bump, featuring relatively sharp corners, and a smoothly contoured bump. Both are illustrated in Figure 1.2. In this illustration, it can also be seen that a wedge-shaped bump achieves its shock wave smearing effect by generating a lambda-shock structure whereas a smooth contour bump achieves it through the generation of a series of compression waves. [27] [28]

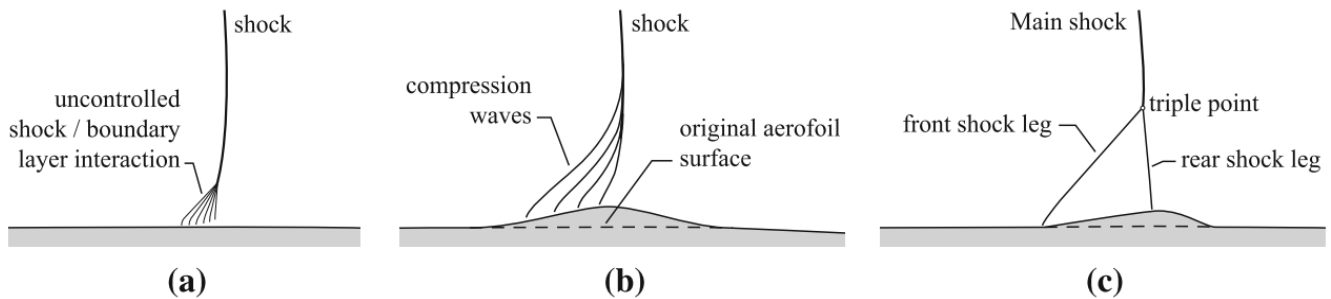


Figure 1.2 Illustration of the different shock structures produced by a SCB: (a) Shock created in the uncontrolled case, source: Bruce & Colliss [6]; (b) compression waves produced by a smooth contour-shaped bump, source: Birkemeyer, et al. [27]; (c) λ -shock structure produced by a wedge-shaped bump, source: Ogawa & Babinsky [28].

Besides making a distinction between the smooth contoured bump and wedge shaped bump there is also the option of considering a two-dimensional or a three-dimensional configuration when considering a bump design for a wing. Here, a 2-D SCB consists of a single continuous bump profile along a section of the wing span and the 3-D SCB design consists of an array of finite width SCBs placed along the wing in spanwise direction, these two configurations are illustrated in Figure 1.3.

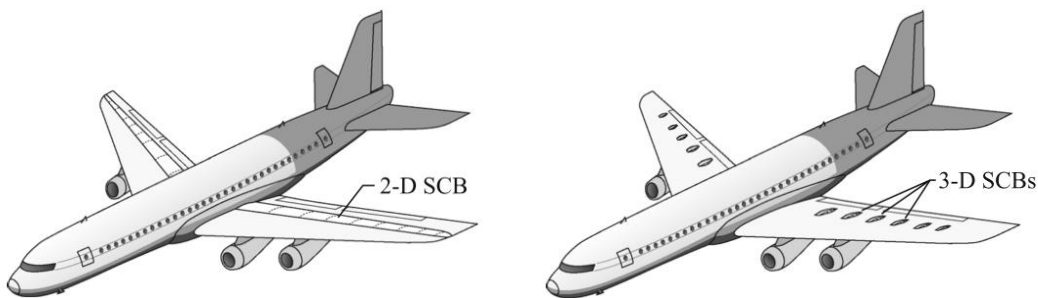


Figure 1.3: Illustration of different SCB configurations on a wing: (left) continuous 2-D SCB; (right) array of 3-D SCBs. Source: Bruce & Colliss [6]

In all bump designs, the geometry of a typical SCB can be divided into three distinct sections, namely: the ramp, the crest, and the tail. The ramp is the region responsible for decelerating the flow in a more isentropic manner than the uncontrolled case, effectively reducing the wave drag. The crest is the tallest region of the bump and consequently the region where a near-normal shock wave returns the flow to subsonic conditions. The tail region is shaped such that the post-shock flow is returned to the original surface as efficient as possible. [4]

1.1.4 Basic Flow Physics

The flow structures generated by SCBs are sensitive to shock-wave position w.r.t. the bump and the incoming boundary layer state. The 3-D SCBs are often considered to be a better alternative to 2-D designs as they generally offer improved robustness to shock position, i.e. improved off-design performance, at a minor degradation in on-design performance. [13] [28] [29] Here, off-design performance is defined as the main shock being situated upstream, or downstream, of the optimal position. [30] In order to assess the practical performance potential of SCBs they are generally analysed over a range of operating conditions, as opposed to a single point analysis, in order to incorporate the off-design characteristics.

1.1.5 Performance

The performance of SCBs is usually assessed as the improvement in lift-to-drag ratio over the performance envelope of the wing, as well as changes to the boundaries on this envelope (e.g. buffet onset and drag divergence Mach number). This provides an indication of the achieved drag reduction while including the associated off-design performance.

Essentially, SCB performance is a trade-off between the reduction in wave drag and the negative effects, e.g. increases in viscous drag and the appearance of secondary shock structures. From the previously performed research it is clear that the application of the SCB results in significant reduction in wave drag for transonic airfoils [13] [31] as well as for transonic wings [13] [28] [32] while the mentioned detrimental effects are kept to a minimum.

1.2 Prior Efforts in Low Sweep Wing Design using Shock Control Bumps

In terms of previous research combining the wave drag reduction provided by SCBs with low sweep transonic wing design, the publications of Qin [32] and Deng et al. [33] are most notable. Both focus on the aerodynamic analysis and comparison of a transonic wing design with an identical wing design which has a reduced sweep angle. Ultimately, the version of the wing with a reduced sweep angle has a series of 3-D SCBs positioned on the upper wing surface which are then optimized for maximum lift-to-drag ratio.

Qin [32] explores the potential of unlocking wing sweep by implementing 3-D SCBs for drag reduction on natural laminar flow (NLF) wings. The possibility to reduce wing sweepback to 20° or less, while maintaining the original flight conditions, is investigated. First, the potential drag reduction for an infinite swept NLF wing with a 20° sweep angle is determined through SCB shape optimization; the result is a 24% reduction in total drag. Second, the potential drag reduction for a 3-D NLF wing with low sweep is investigated. The conditions for this analysis are set such that they mimic the problem of reducing wing sweep from 30° to 20° while maintain a constant cruise Mach number of $M = 0.85$. For a fixed incidence, a 12% improvement in lift-to-drag ratio was found, the initial and optimized wings with 20° sweep are shown in Figure 1.4. The reduced sweep is concluded to result in two major benefits; the possibility to enable NLF wing design and a potential structural weight reduction due to the reduced sweep.

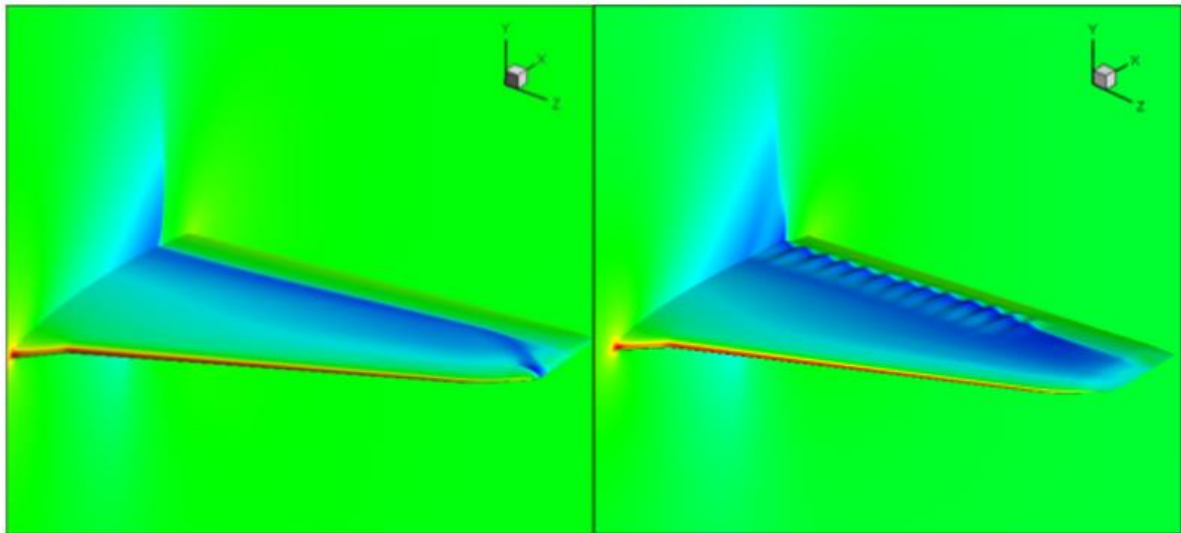


Figure 1.4: Low sweep wing without (left) and with (right) an array of optimized 3-D SCBs. Source: Qin [32]

Deng et al. [33] initially designed a traditional transonic wing with a quarter chord sweep angle of 24.5° . Then they designed a wing with reduced sweep on which 3-D SCBs were implemented and optimized, the quarter chord sweep angle of this wing is 16.0° . Figure 1.5 provides an illustration of both the baseline wing and the reduced sweep wing including 22 optimized 3-D SCBs. Even though the reduced sweep wing without SCBs has a drag coefficient that is roughly 13% higher than that of the baseline wing, the reduced

sweep wing with the optimized SCBs has a drag coefficient that is about 2% lower than that of the baseline wing. Hence, it was concluded that the new wing has the same level of drag yet, according to empirical relations, requires less structural weight because of the reduced sweep; eventually resulting in fuel weight reductions.

In order to see the effect on maximum lift at low speed conditions the performance of all three wings were also investigated at low speed conditions, for which the results are shown in Figure 1.6. In this image, it can be observed that the low sweep wings have a reduced maximum lift coefficient and the lift curve of the wing with bumps is shifted upward, likely due to the cambering effects of the bumps. The effect on the maximum lift was determined to be insignificant.

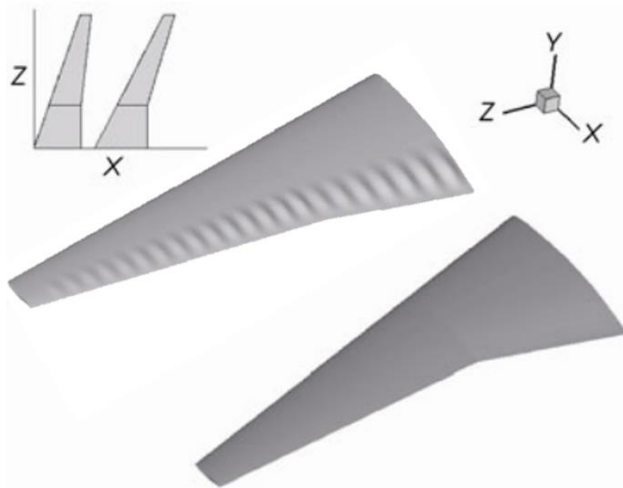


Figure 1.5: Illustration of lowering the sweep angle by an array of optimized 3-D SCBs. Reproduced from Deng, et al., [33].

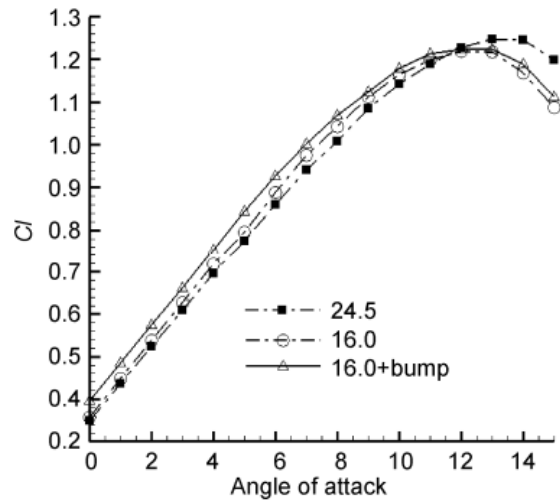


Figure 1.6: Lift coefficient vs. angle of attack at Mach 0.2. Source: Deng, et al., [33].

Neither of these papers include numerical structural or performance analysis. Instead, references are made to empirical relations, such as Howe [34], for the potential weight reduction due to a reduction in wing sweep angle; no calculations are included. Consequently, any influence the structural weight saving would have on the required lift generation of the wing, or fuel weight reduction due to improved aerodynamic performance, are also not taken into account. Additionally, only fixed reductions in sweep angle are considered, i.e. the sweep angle is not a variable in the optimization. There is even potential for larger sweep angle reductions, this can be concluded from the result of Qin [32] since the low sweep wing still experiences a 2% total drag reduction with respect to the baseline wing which could be converted into further reduced wing sweep.

1.3 Research Objective

The research definition consists of the research objective and the research question and sub-questions. First, the research objective will be defined, which can be broken down into a “what”- and a “how”-part. Then, the research question stemming from the research objective will be defined and broken down into more specific sub-questions. Answering these sub-questions provides the answer to the research question and will, in the end, achieve the research objective.

The objective of this research can be defined as follows:

Assess the feasibility of using the wave drag reduction facilitated by shock control bump implementation to reduce the sweep angle of a transonic wing while maintaining its original flight conditions by performing a multi-disciplinary design optimization on the wing with the maximum take-off weight as the objective function, sweep angle, angle of attack, and shock control bump shape parameters as design variables, and original flight conditions as constraints.

The research question stemming from the research objective then follows as:

How much weight reduction can be achieved by implementing the concept of shock control bumps on an A320-like wing, to facilitate reducing its sweep angle, while maintaining the original flight conditions?

In turn, this main question can be broken down into several sub-questions which are more tangible, namely:

1. *By what amount can the maximum take-off weight of an A320-like aircraft be reduced by a reduction in wing sweep angle whilst maintaining the original flight conditions?*
 - a. *What is the influence of sweep angle reduction on the aerodynamic performance of an A320-like wing?*
 - b. *What is the influence of the addition of shock control bumps to an A320-like wing on the aerodynamic performance?*
 - c. *What is the influence of sweep angle reduction for an A320-like wing on the wing structural weight?*
2. *By what amount can the sweep angle of an A320-like wing be reduced when shock control bumps are implemented whilst maintaining the original flight conditions?*
 - a. *How much (wave) drag reduction can be achieved for an A320-like wing by implementing shock control bumps?*
 - b. *How much sweep angle reduction for an A320-like wing can be achieved for a given increase in (wave) drag whilst maintaining the original flight conditions?*

The first set of sub-questions focuses on the relation between sweep angle reduction and MTOW and the second set of questions focuses on the relation between SCBs and sweep angle reduction.

1.4 Thesis Outline

The structure of this thesis is as follows. Chapter 2, Chapter 3, and Chapter 4 introduce and explain the aerodynamic, structural, and performance discipline analysis, respectively. Then, Chapter 5 describes the general optimization formulation and set-up. The test case applications and their results are reported in Chapter 6. Ultimately, the conclusions and recommendations of this thesis are discussed in Chapter 7.

2

Aerodynamic Analysis

The aerodynamic analysis is required to determine the aerodynamic properties of the wing model. More specifically, the aerodynamic loads acting on the wing under the critical load case are required by the structural analysis, which will be discussed in Chapter 3, and the lift and drag coefficients are required for performance analysis, discussed in Chapter 4.

For the determination of the aerodynamic coefficients a Computational Fluid Dynamics (CFD) program will be used, namely Stanford University Unstructured (SU²) [35]. This program will be used to solve the governing equations for inviscid flow, the Euler-equations, for a mesh that matches the baseline wing design. This tool also includes the capability of deforming the mesh, which is used to implement the SCB shapes and adjust the sweep angle of the wing. Naturally, the Euler-equations are also solved for these deformed meshes. Additionally, a continuous adjoint method is built into the program which allows the tool to determine the sensitivities of the drag and lift coefficients w.r.t. shape deformations and changes in angle of attack.

A separate tool will be used to estimate the aerodynamic loads acting on the wing under the critical load case which will be used for structural sizing. This tool is the quasi-3-D aerodynamic solver (Q3D-solver) which has been specifically developed in context of the structural analysis tool, EMWET, and will be discussed in Chapter 3, which discusses the details of EMWET.

The structure of this chapter is as follows. The details of SU² and the CFD code implementation are provided in Section 2.1. Then, the method used within SU² for geometry parameterization is introduced and discussed in Section 2.2. Lastly, the approach used for gradient computation is reported in Section 2.3.

2.1 Stanford University Unstructured

Stanford University Unstructured (SU²) software suite is an open-source, integrated analysis and design, C++ tool for solving complex, multi-physics analysis and optimization problems governed by PDEs on general, unstructured and structured meshes. [35] The core of the suite is a CFD solver capable of simulating the compressible, turbulent flows that are characteristic of typical problems in aerospace engineering. Yet, the framework of SU² is general and meant to be extensible to arbitrary sets of governing equations for solving multi-physics problems. Additionally, since SU² has been developed with the purpose of aerodynamic shape optimization in mind, a Free-Form Deformation (FFD) method based geometry parameterization and adjoint-based sensitivity analysis are directly built into the solver. [36] The details and implementation of these different aspects of SU² are discussed in the following sections. The validation of the CFD code used in SU² can be found in Palacios et al. [35].

Computational Fluid Dynamics

Fluid flows are governed by partial differential equations (PDEs) which represent the laws of conservation for mass, momentum, and energy. CFD is a branch of fluid mechanics that uses numerical analysis and algorithms to solve these PDEs and analyse the results. The interaction of fluid flows with surfaces defined by boundary conditions are simulated by using computers to perform the necessary calculations. CFD allows designers to analyse novel and unconventional designs before investing into expensive experimental tests such as wind tunnel tests.

Governing Equations

The Navier-Stokes (NS) equations are the governing equations for a compressible and viscous fluid. They describe the relation between velocity, pressure, temperature, and density of a fluid in motion, including the effects of viscosity and compressibility. These equations consist of the momentum equations, the mass conservation equation, and the energy equation. Converging the NS equations for a flow is extremely expensive in terms of computation power due to the inherent velocity scales, variations, and unsteadiness. Often simplified versions of the equations are used in order to improve the computation time to convergence.

By applying the Reynolds decomposition to the NS equations, the Reynolds-Averaged Navier-Stokes (RANS) equations are obtained. Here, the assumption is made that the time-dependent turbulent velocity fluctuations can be separated from the mean flow velocity. This does, however, introduce Reynolds stresses which give rise to turbulence. Thus, with the addition of a turbulence model, a closed system of solvable equations is obtained. The RANS equations have computational requirements that are orders of magnitude less than the NS equations and are also inherently steady.

With the additional assumptions of zero thermal conductivity and the flow to be inviscid the NS equations are reduced to the Euler equations. This is a significant simplification - analogous to ignoring friction forces when determining the acceleration of an object due to gravity – which improves the computational time of the analysis even further than for RANS, at the cost of reduced accuracy and completeness. Because the flow is assumed to be inviscid, the effects of viscosity and boundary layer effects can no longer be accounted for. Consequently, the Euler equations should only be used for analyses where the assumption that the flow is inviscid is appropriate and boundary layer effects can be ignored. Ultimately, when the flow is also assumed to be incompressible, the NS equations are simplified even further into the well-known Bernoulli equation.

Enhanced Convergence

The CFD module of SU² incorporates two functionalities that greatly improve the required computational time to convergence, namely the multi-grid functionality and the flow restart functionality. The multi-grid option allows the tool to split the initial grid into multiple coarser grids. This effectively reduces the distribution of low frequency errors which, in turn, increases the convergence rate of the implemented standard solvers.

The flow restart setting allows the re-use of previous solution files of the same mesh as the starting point for new CFD runs. This even allows the re-use of the converged solution of the pre-deformation mesh for a deformed mesh. This setting proves very useful for small mesh deformation, for which the pre-deformed solution is likely to be similar to the previously converged solution.

Application

For the optimizations performed in this thesis the Euler equations will be used to determine the aerodynamic properties of the model. Using the Euler model instead of the RANS model has shown to reduce the computational time to reach a solution by up to 25% with only marginal differences in coefficient values. [37] Additionally, creating a mesh that is suitable for RANS analysis is considerably more time-consuming than creating one for Euler analysis. Additionally, Ashill et al. [9] [38] have shown that SCBs can reduce wave drag without affecting viscous drag, which makes the assumption of inviscid flow reasonable.

2.2 Geometry Parameterization: Free-Form Deformation

SU² uses the Free-Form Deformation (FFD) strategy for geometry parameterization. [39] [40] In this strategy a FFD box envelops the object or surface that is to be redesigned or optimized. This box is then parameterized as a Bezier solid and the Cartesian coordinates of the surface inside this Bezier box are transformed into parametric coordinates within the box. Control points are then defined on the surface of the FFD box. Here, the number of control points is directly related to the order of the Bernstein polynomials used in the Bezier solid definition. Moving these control points influences the shape of the Bezier solid and, indirectly, the shape of the linked surface inside the box.

Using the FFD method for shape aerodynamic shape optimization provides a significant degree of freedom to the optimizer. One example of the flexibility and robustness is found in Gagnon & Zingg [41], whom performed an aerodynamic shape optimization on a sphere with the objective to maximize the lift-to-drag ratio the resulting shape produces. This optimization resulted in a shape resembling that of a blended wing body, as is shown in Figure 2.1. The numbers in this figure indicate the amount of times the objective function has been evaluated to reach the shown design. The original and optimized FFD boxes, including the surfaces, are also provided in a side-by-side comparison, see Figure 2.2.

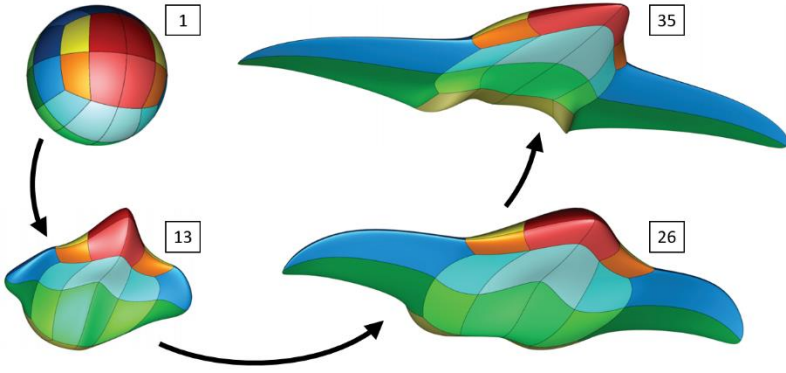


Figure 2.1: From sphere to blended wing body using the FFD method. Reproduced from Gagnon & Zingg [59].

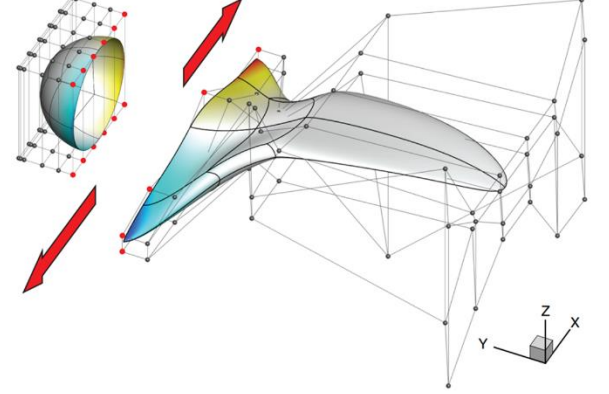


Figure 2.2: Initial and deformed surfaces. Source: Gagnon & Zingg [59]

However, the surface deformation is only the first half of any FFD implementation. Even though the surfaces are the main focus of any shape optimization, the majority of the mesh consists of a volume mesh. This volume mesh is also required to deform in order to match the deformed surface mesh, while maintaining the overall mesh quality. Hence, the second half of the FFD implementation is the method used for the volumetric deformation of the mesh. To provide the full scope of the previously used example, the associated initial and deformed grids are provided in Figure 2.3. Here, a grid-point-based volume mesh movement method [42] was used.

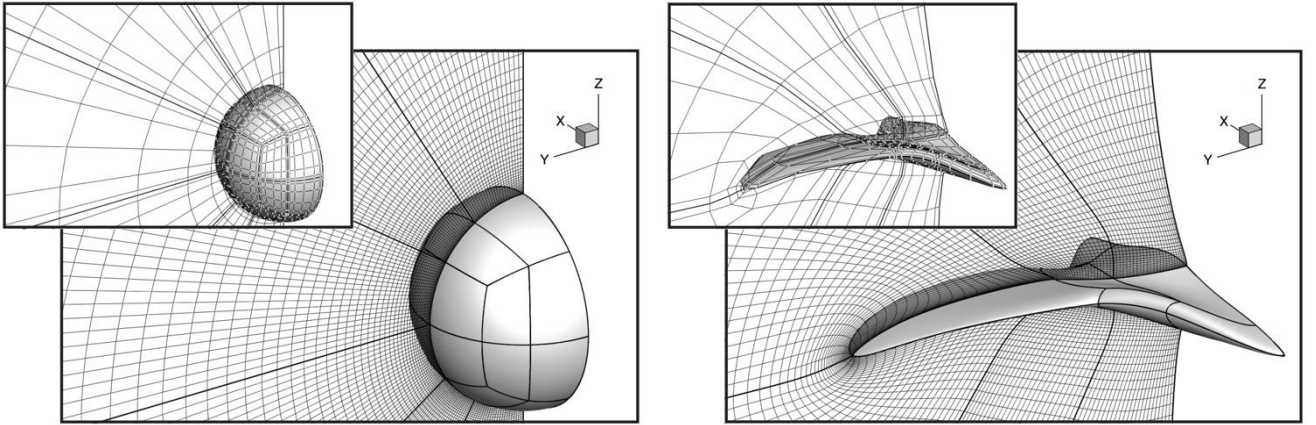


Figure 2.3: Initial and deformed grid using a grid-point-based method. Source: Gagnon & Zingg [41]

In contrast, the volumetric deformation procedure used in SU^2 is based on a classical spring method. In this approach, the mesh is treated as an elastic solid and non-uniform stiffnesses are assigned to all the elements in volume mesh. The key element is the definition of the corresponding stiffness matrix. Once this matrix has been determined, equilibrium of forces is imposed at each mesh node using Equation 2.1. [35]

$$\left(\sum_{j \in N(i)} K_{ij} \cdot \vec{e}_{ij} \cdot \vec{e}_{ij}^T \right) \cdot \vec{u}_i = \sum_{j \in N(i)} K_{ij} \cdot \vec{e}_{ij} \cdot \vec{e}_{ij}^T \cdot \vec{u}_j \quad 2.1$$

In this equation, $N(i)$ is the set of neighbouring points to node i , \vec{u}_i represents the unknown volume displacement and is computed as a function of the known surface displacements, \vec{u}_j . K_{ij} is the stiffness

matrix and \vec{e}_{ij} is the unit vector in the direction connecting both points i and j . An illustration of a volume mesh deformation performed by SU² is provided in Figure 2.4.

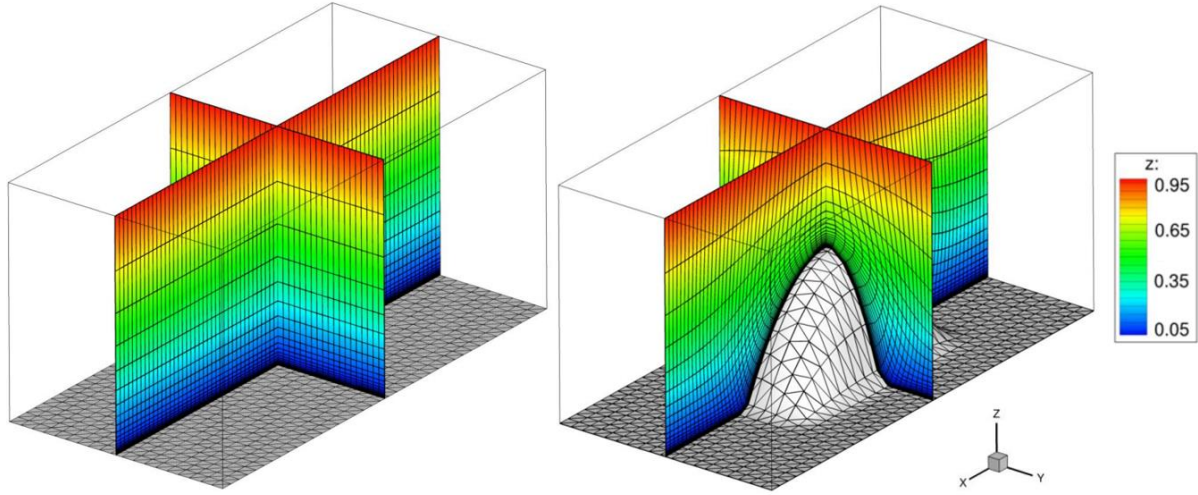


Figure 2.4: Initial and deformed grid using the spring-based volume movement method. Source: Palacios et al. [43]

FFD Implementation for Sweep Adjustment

For the geometry parameterization in this thesis, two types of FFD boxes are required: one global FFD box which deforms the planform of the wing and a series of local FFD boxes that deform part of the upper wing surface. The relation between the global box and the local boxes, from this point on respectively referred to as planform box and SCB boxes, is defined such that the planform box does not only deform the wing but also the SCB boxes. This ensures that the SCB boxes are at a constant position relative to the wing, even after performing deformations with the planform box.

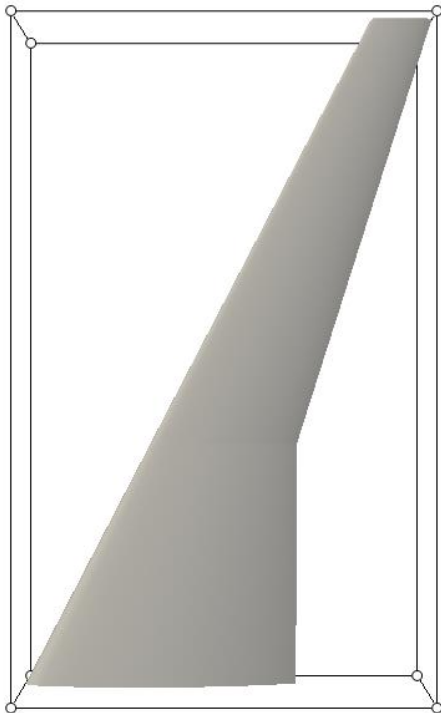


Figure 2.5: Top view of the planform FFD box.

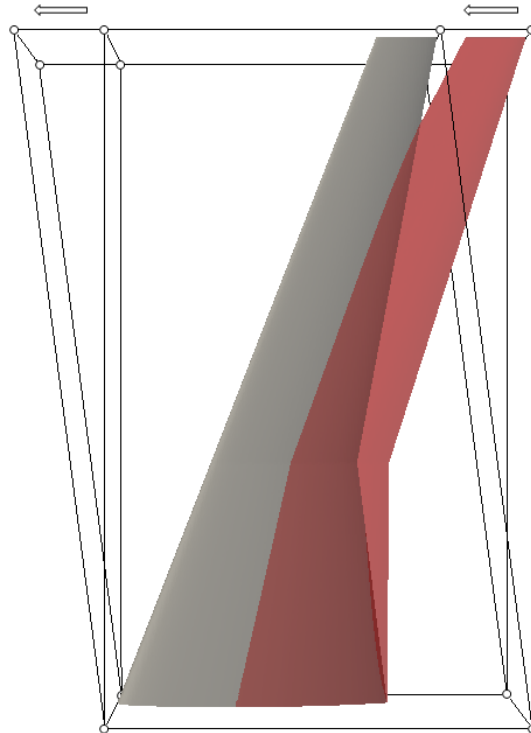


Figure 2.6: Deformation using the planform FFD box.

As the name suggests, the planform box is well suited for redefining planform variables, such as the sweep angle of the wing. An illustration of the planform box is provided in Figure 2.5. As can be seen in this figure, the corner points of the planform box are positioned such that they envelop the entire surface model, i.e. they define the bounding box of the wing. In order to adjust the sweep angle of the wing, all four control points

on the outboard side of the wing are translated either forward, for a reduction in sweep, or aft, for an increase in sweep, using a linear deformation setting. An example deformation in which a wing sweep is reduced is shown in Figure 2.6. Apart from the corner control points, no additional control points are required for this box as only the corner control points are required for the sweep deformation.

FFD Implementation for Shock Control Bump Design

The SCB boxes can be used to position and size the SCBs on the upper surface of the wing. An illustration of the most inboard SCB boxes is shown in Figure 2.7. As can be seen in this figure, and in contrast to the planform box, the SCB box cuts through the upper surface of the wing model, this allows for more refined shape control of the surface inside the box. Additionally, the control point layout for the most inboard SCB box are shown in this figure, namely five in spanwise direction and ten in chordwise direction. The layout of the control points will be discussed further into this section.



Figure 2.7: Illustration of the SCB box control point layout (top) and example 3-D SCBs (middle) and 2-D SCB (bottom) shapes.



Figure 2.8: Top view of all 20 SCB boxes, only corner control points are shown.

Because the optimal position of an SCB is relative to the shockwave position, where the shockwave position changes for different flight conditions and sweep angles, the positioning and sizing of the SCB boxes is not as straight forward as for the planform box. In order to identify the area of the upper surface that is of interest for SCB design, an approach similar to the mesh adjoint method used by Zhu & Qin [44] is followed. In the mesh adjoint method the surface sensitivities with respect to drag are visualized on the surface of interest. This visualization identifies the area which will be sensitive for SCB design, as is illustrated in Figure 2.9. In this figure, λ_{gz} is the surface sensitivity with respect to the drag coefficient when deforming the wing upper surface in positive Z-direction.

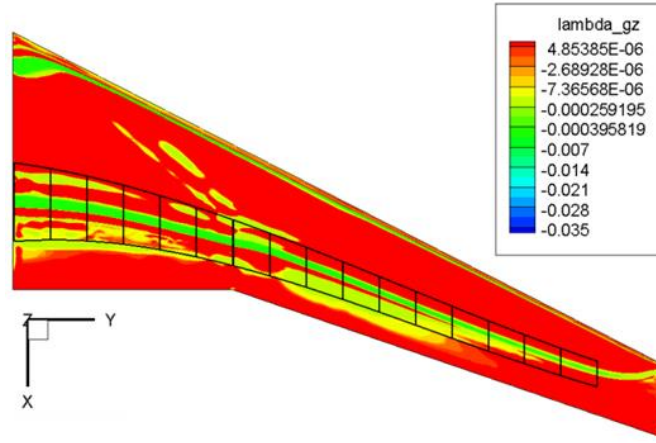


Figure 2.9: Illustration of the mesh adjoint method. Source: Zhu & Qin [44]

However, for the optimization defined in this thesis it is known beforehand that the shockwave position will be varying during the optimization, both because of the changing lift coefficient due to weight reduction and because of the reduction in sweep. Hence, in order to take these effects into account, the SCB boxes will be positioned and sized such that they envelop the most forward, and the most aft, expected shockwave positions. The resulting layout of the SCB boxes is shown in Figure 2.8.

A total number of twenty SCB boxes are used for the optimizations performed in this thesis, this number is based on the optimized wing designs from Deng et al. [33]. The reason for using a series of smaller boxes, opposed to one larger box, is the increase in shape deformation control and the improved computation time of the sensitivity information. Both of these benefits are achieved by the reduced number of elements which are assigned to a control point.

The variable position of the shockwave also requires a larger number of control points in chordwise direction, as this provides the optimizer with control over the chordwise position of the SCBs. Additionally, it has to be taken into account that in order to ensure second order geometric continuity, i.e. a smooth and continuous transition of the surface outside the box with the surface inside the box, the two outermost rows of control points have to remain unaltered. In chordwise direction it has been determined that ten control points, of which then six are allowed to be used for deformations, is enough to accurately position the bumps with respect to the shock wave location. This results in the control point layout as shown in Figure 2.7. Here, the white control points are inactive, due to the geometric continuity requirement, and both blue and red control points will be used for 2-D SCB design. For 3-D SCB design only the red control points will be active, as will be explained in the next paragraph. This layout applies to all twenty SCB boxes, here it is only shown for the most inboard box in order to maintain clarity in the other figures.

For the number of control points in spanwise direction the 3-D SCB design case is the determining factor. In order to design a 3-D SCB, at least the centre control point - in spanwise direction - needs to be available for deformation. Hence, combining this requirement with the second order geometric continuity a number of five control points is required in spanwise direction. Of course, in the case of 2-D SCB design the geometric continuity only applies at the outboard end of the bump. This does, however, not affect the required number of control points as five points is more than sufficient in the 2-D SCB design case. Figure 2.7 provides an example of 3-D SCBs and 2-D SCB using the three inboard most SCB boxes.

2.3 Sensitivity Analysis: Continuous Adjoint Method

For the majority of design variables used for shape optimization, the build-in continuous adjoint method from SU² can be used to compute the gradient information. The advantage of using the adjoint approach over using, for example, the Finite Difference Method (FDM), lies in the number of additional evaluations required. When FDM is used the number of calculations increases by the number of variables, not attractive when a large number of variables is being considered and each evaluation takes considerable resources to complete. When the continuous adjoint approach is used, only one additional calculation is required,

independent of the number of variables. The disadvantage of the continuous adjoint method is the time-consuming implementation, whereas FDM is fast and simple to implement. Of course, from a end-user point of view the disadvantage of implementation efforts is irrelevant.

Continuous Adjoint Method

The implementation of the continuous adjoint method in SU² can be explained as follows. The derivative of a general objective function is given by Equation 2.2.

$$\frac{dF}{dX} = \frac{\partial F}{\partial X} + \frac{\partial F}{\partial Y} \frac{dY}{dX} \quad 2.2$$

Here, F is the cost function, X the design vector and Y the state-variable vector. As has been mentioned earlier, the determination of dY/dX would require one converged flow solution per variable when using FDM. Instead, a more efficient method can be defined by determining the sensitivity with respect to the residual, R , as introduced in Equation 2.3.

$$\frac{dR}{dX} = \frac{\partial R}{\partial X} + \frac{\partial R}{\partial Y} \frac{dY}{dX} = 0 \quad 2.3$$

By substituting Equation 2.3 in Equation 2.2 the resulting Equation 2.4 is obtained. which can be used to determine the adjoint vector, ϕ .

$$\frac{dF}{dX} = \frac{\partial F}{\partial X} - \frac{\partial F}{\partial Y} \left(\frac{\partial R}{\partial Y} \right)^{-1} \frac{\partial R}{\partial X} \quad 2.4$$

Finally, the adjoint equation is defined in Equation 2.5 and combining this equation with Equation 2.4 gives the variation of the objective function with respect to the design variables as Equation 2.6.

$$\frac{\partial R}{\partial Y} \cdot \phi = - \frac{\partial F}{\partial Y} \quad 2.5$$

$$\frac{dF}{dX} = \phi \cdot \frac{\partial R}{\partial X} + \frac{\partial F}{\partial X} \quad 2.6$$

In this equation, the partial derivatives are less computationally expensive to compute than the derivative of dY/dX as used in Equation 2.2. The full details of the implementation can be found in Palacios et al. [35].

Gradient Projection

Following this approach will ultimately result in the sensitivity of each mesh node with respect to the aerodynamic coefficients. These sensitivities are then projected onto the FFD control points as this will limit the number of design variables; having each surface node as a design variable is sub-optimal, at the very least. This projection of the node sensitivities onto an FFD control point is given by Equation 2.7. [45]

$$\frac{\partial F}{\partial \kappa} = \int_S \left\{ \frac{\partial F}{\partial S} \right\} \frac{\partial S}{\partial \kappa} ds \approx \sum_{i \in N(S)} \left\{ \frac{\partial F}{\partial S} \right\}_i \frac{n_i \cdot \Delta x_i}{\Delta \kappa} \Delta S_i \quad 2.7$$

Here, κ represents the FFD variables, S is the affected surface, $N(S)$ is the number of nodes on S , $\partial F/\partial S$ the surface sensitivity on node i as calculated by the adjoint method, n_i is the unit vector normal to the surface at i , Δx_i is the change of node i in Cartesian coordinates after a perturbation of the FFD variable, ΔS_i is the area surrounding node i .

The process of gradient projection can be time consuming when large numbers of node sensitivities need to be projected onto control points. Hence, the choice of FFD box dimensions and number of control points has significant influence on the computation time of the gradient information.

Sensitivity Information Verification

Due to the well-known complexity of sharp edge phenomenon, the computation of sensitivity information near the trailing edge of the wing is unreliable while using SU². [46] In response, SU² offers the option to ignore the surface sensitivity information of the area effected by the sharp edge phenomenon. However,

when a planform geometrical parameter, such as sweep angle, is defined as a design variable, computing the sensitivities over the complete wing surface is a necessity. Ignoring the sensitivities of even a relatively small area, especially a critical area such as near the wing trailing edge, leads to significantly erroneous gradient information. Hence, the sensitivity information computed by SU² has been verified for the FFD implementations used in this research.

The verification data of the continuous adjoint sensitivities concerning the lift and drag coefficients is listed in Table 2.1. As already mentioned, the sensitivities computed with respect to the sweep variable are not accurate, hence it was decided to use FDM in order to compute these sensitivities accurately. As for the other sensitivities computed using the continuous adjoint, these are deemed accurate and will be used.

Table 2.1: Verification of the continuous adjoint sensitivities.

Sensitivity	Continuous Adjoint	Finite Difference	Ratio
$dC_D/d\alpha$	0.0078553	0.0080400	0.977
$dC_L/d\alpha$	0.1430200	0.1430977	0.999
$dC_D/d\Lambda$	-0.0845295	0.1092913	-1.293
$dC_L/d\Lambda$	-0.9771030	0.8941343	-0.915
$dC_D/d\kappa$	6.1918E-5	6.7800E-5	0.913
$dC_L/d\kappa$	0.0016189	0.0017120	0.946

3

Structural Analysis

Accurate estimates of the total fuel weight and wing structural weight are required for the determination of the MTOW of the aircraft model. While the total fuel weight is to be calculated by the performance analysis, discussed in Chapter 4. The wing structural weight is determined by the structural analysis, which is discussed in this chapter.

First, EMWET is introduced in Section 3.1. Then, the method used in EMWET internally to determine the loads acting on the wing is briefly explained in Section 3.2. Then the validation results of EMWET are provided, and the application of EMWET in this research are discussed, in Section 3.3 and Section 3.4, respectively.

3.1 Elham Modified Weight Estimation Technique

For the structural analysis and weight estimation of the wing the Elham Modified Weight Estimation Tool (EMWET) [47] is used. EMWET estimates the weight of the wing primary structure using analytical sizing of the wing-box structure. For the estimation of the secondary weights, e.g. high lift devices and control surfaces, a series of empirical methods are used. EMWET represents the load carrying structure of the wing, the wing box, as four equivalent panels: the upper panel, the lower panel, and two side panels. The upper and lower panels represent the skin, stringers, and spar caps at their respective side and the two vertical side panels represent the spar webs located at the front and rear sides.

The upper equivalent panel experiences compressive loads in positive load factors and is required to experience stresses lower than both the compressive yield stress and the buckling stress of its material and structure. For the determination of the buckling stress the stiffened panels efficiency method is used. The lower equivalent panel experiences tensile loads in positive load factors and is required to experience stresses lower than the tensile yield stress of its material. The two equivalent side panels experience shear loads and are required to experience stresses lower than both the yield shear stress and shear buckling stress. For sizing all the four panels a safety factor of 1.5 applies.

3.2 Load Determination

The applied aerodynamic loads required to size the wing-box structure are calculated using Athena Vortex Lattice (AVL) which uses an extended Vortex Lattice Method (VLM) to determine the forces and moments acting on lifting surfaces. In addition to the aerodynamic loads, the relief loads due to the engine, fuel, and wing structural weights are also used in the determination of the net sizing loads. Once the net sizing loads are determined the wing box weight is calculated and secondary weights, as well as non-optimum weights, are estimated using statistical weight estimation equations. [48]

3.3 Validation of EMWET

Validation of EMWET is published in Elham et al. [47]. The results of this validation can be summarized by Figure 3.1, which illustrates the accuracy of the weight calculated by EMWET versus the actual weight, and Table 3.1, which provides the error in wing weight estimation for reference aircraft over a range of MTOWs.

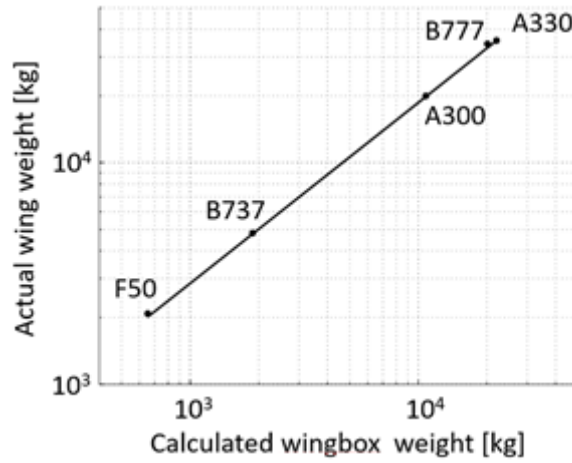


Figure 3.1: EMWET validation. Source: [47]

Table 3.1: EMWET validation data. [47]

Aircraft	Maximum take-off mass [kg]	Error of wing weight estimation [%]
Fokker 50	20 820	-0.72
Boeing 737-200	52 390	0.15
Boeing 727-300	95 028	-2.71
Airbus A300-600R	170 500	1.86
Airbus A330-300	217 000	-2.18
Boeing 777-200	242 670	2.66

3.4 Application

Ideally, for an accurate wing weight estimation a series of different load cases are analysed. However, in this research only one load case, which is assumed to be the critical load case, is analysed. More specifically, the aerodynamic loads are computed for a pull-up manoeuvre at cruise altitude with a load factor 2.5g.

The used wing planform, as well as the dimensions for the wing-box and fuel tank, are introduced and discussed in Chapter 6. For the airfoil shapes the assumption is made that the addition of the SCB has no negative effect on the wing weight and the airfoil shapes without the SCB are used as input for EMWET.

Lastly, the sensitivity information that is required from the structural analysis will be computed using FDM as EMWET, and its internal components, do not incorporate any method for gradient information computation.

4

Performance Analysis

With the details of the structural analysis explained, all that is left in order to determine the MTOW is the calculation of the total fuel weight, which is done by the performance analysis, discussed in this chapter. The performance analysis is also responsible for calculating the weight of the aircraft at the design point. This weight is then used to determine the lift coefficient that is required of the wing to maintain steady horizontal flight.

Conveniently, both the fuel weight and design point weight can be determined by the mass fractions method from Roskam [49]. This method divides the flight mission in several unique phases. With the exception of the cruise phase, these phases are each assigned mass fractions based on reference data. For the cruise phase the well-known Breguet range equations is used to determine its mass fraction. Ultimately, these mass fractions can be used to determine the start and end weights of each phase as well as the total fuel weight.

First, the mass fractions method and the Breguet range equation, which are essential to both the design weight and the fuel weight calculation, are introduced in Section 4.1. Once the Breguet range equation has been discussed, the approach used to determine the weight at a design point can be elaborated, this is done in Section 4.2. The details of the method to determine the total fuel weight can also be discussed at this point, these details are provided in Section 4.3. Lastly, the method used to obtain the sensitivity information required from the performance analysis is introduced in Section 4.4.

4.1 Mass Fractions Method and the Breguet Range Equation

In order to estimate the weight of the reference aircraft at different points during its flight profile, the mass fraction method from Roskam [49] will be used. This method separates the mission profile of the aircraft into distinct phases for which it determines the aircraft weight using mass fractions. Here, the mass fraction associated with a phase is nothing more than the ratio of the initial and final weight of the aircraft for that particular phase. Since the only change in weight during the flight profile is due to fuel burn, these mass fractions can be used to determine the fuel weight required for a typical mission with a specified cruise range.

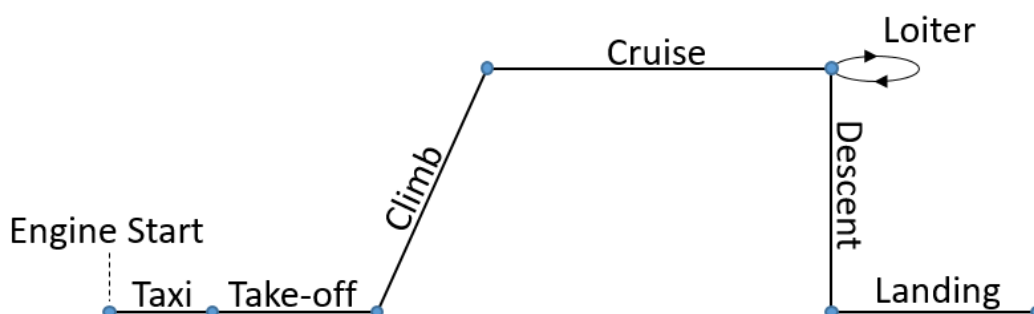


Figure 4.1: Typical mission profile for a commercial transonic passenger aircraft.

The typical, simplified, mission profile for a commercial civil air transport flight is provided in Figure 4.1. Here, the mission profile consists of seven distinct phases for which the mass fractions need to be known in order to estimate the required fuel weight. With the exception of the cruise phase, the mass fractions can be determined based on reference data provided by Roskam [49]. The mass fractions of the respective flight phases, as shown in the above figure, are listed in Table 4.1.

As can be seen in the figure and table, there is technically also an eighth phase, namely loiter and/or redirect. However, the fuel used during this phase will be included in the overall reserve fuel, which is a fraction of the total fuel weight excluding reserves. Because the fuel used during this eighth phase is already included in the reserve fuel, the fraction for this phase does not have to be determined along with the other fractions.

Table 4.1: Flight phases and their respective mass fractions. [49]

Phase	Description	Mass Fraction
1	Engine start & warm-up	0.990
2	Taxi	0.990
3	Take-off	0.995
4	Climb	0.980
5	Cruise	See equation 4.2
6	Descent	0.990
7	Landing, taxi, shutdown	0.992
*	Loiter, redirect	Included in reserves

Since the mass fraction of the cruise phase accounts for the majority of the total fuel weight, while it is also dependent on aircraft performance and the specified cruise range, it will be calculated using the Breguet range equation. The range equation determines the range, R , for a given mass fraction of phase m , f_m , specific fuel consumption (SFC), SFC , cruise velocity, V_{cr} , and lift-to-drag ratio, L/D , as is shown in Equation 4.1.

$$R = \frac{V_{cr}}{C_T} \cdot \frac{L}{D} \cdot \ln(f_m) \quad 4.1$$

In other words, this equation can be rewritten to calculate the mass fraction as a function of the cruise range, SFC, cruise flight speed, and lift-to-drag ratio. This rewritten range equation is shown in Equation 4.2.

$$f_m = \exp\left(\frac{R_{cr} \cdot SFC}{V_{cr}} \cdot \left[\frac{L}{D}\right]^{-1}\right) \quad 4.2$$

In order to use this equation, two assumptions have to be made. The first being that the wing lift coefficient as determined by the aerodynamic analysis is equal to the total lift coefficient.

The second assumption is related to the friction drag component of the total drag coefficient. As was mentioned in Chapter 2, the effects of viscosity are not incorporated by the aerodynamic analysis. Hence, the total drag that is computed by this analysis is excluding the viscosity drag component, i.e. the friction drag. In order to incorporate the friction drag, it will be computed once for the reference aircraft and this value for the friction drag coefficient is then assumed to remain constant throughout the optimization.

The definition of the lift-to-drag ratio under these assumptions is provided in Equation 4.3. In this equation, the total drag coefficient, C_D , is taken as the sum of the viscous drag component, C_{D_v} , the wave drag component, C_{D_w} , and the induced drag component, C_{D_i} . The total lift coefficient, C_L , is equal to the wing lift coefficient, $C_{L_{wing}}$.

$$\frac{L}{D} = \frac{C_L}{C_D} = \frac{C_{L_{wing}}}{C_{D_v} + C_{D_w} + C_{D_i}} \quad 4.3$$

4.2 Design Point Weight

The conditions for which the wing needs to be optimized need to be chosen carefully as these greatly affect the outcome of the optimization. A common approach is to optimize the wing for the so-called cruise design point, given by Equation 4.4. This method, however, cannot take into account variations in performance during the cruise phase and it is exactly these variations which are important to consider when designing SCBs due to potentially poor off-design performance of the bumps. Hence, a more suitable approach is to

consider multiple points spread out over the cruise phase, in order to improve the practical performance and robustness of the resulting design. To determine the aircraft weight at the design point(s) the already introduced mass fractions method will be used.

$$W_{D_{cr}} = \sqrt{W_M \cdot (W_M - W_F)} \quad 4.4$$

In order to determine the design point weight, the cruise phase will be split up into sections of equal range for each of the points. Then, the weight of the aircraft at the start of the cruise phase is determined by multiplying the MTOW with the mass fractions associated with the phases pre-cruise, as illustrated by Equation 4.5 and Equation 4.6. In these equations, the mass fraction of the i^{th} flight phase is denoted by f_i and W_4 is the weight at the end of the climb phase, i.e. the weight at the start of the cruise phase.

$$f_{1-4} = \prod_{i=1}^4 f_i \quad 4.5$$

$$W_4 = W_M \cdot f_{1-4} \quad 4.6$$

Once the weight at the start of cruise has been calculated, the mass fractions for the intermediate cruise phase sections are determined using the section ranges and the rewritten Breguet range equation, as shown in Equation 4.7. For this equation, the mass fraction, section range, lift coefficient, and drag coefficient for design point n are denoted by $f_{5,n}$, R_n , C_{L_n} , and C_{D_n} , respectively.

$$f_{5,n} = \exp\left(\frac{R_n \cdot C_T}{V_{cr}^2} \cdot \frac{C_{D_n}}{C_{L_n}}\right) \quad 4.7$$

Once all the mass fractions have been determined, the design point weight for each separate section can be calculated. Initially, the weights at the start and end of the section will have to be determined using the mass fractions. Then, the design point weight is found by taking the square root of their products. The equation illustrating these steps is shown in Equation 4.8.

$$\begin{cases} W_{start_n} = \left(W_4 \cdot \prod_{i=0}^{n-1} f_{5,i} \right), \\ W_{end_n} = \left(W_4 \cdot \prod_{i=0}^n f_{5,i} \right), \\ W_{D_n} = \sqrt{W_{start_n} \cdot W_{end_n}} \end{cases} \quad 4.8$$

4.3 Fuel Weight

The fuel weight of the design can be determined in a similar approach as the design point weight, albeit more straightforward since the fuel weight is determined by the mission start weight, mission end weight, and reserve mass fraction; it does not require any intermediate data once the mass fractions are known. The total mass fraction, f_{total} , is determined by the sum product of all flight phases, as illustrated in Equation 4.9.

$$f_{total} = \prod_{i=1}^7 f_i \quad 4.9$$

In case of the multi-point analysis, the fraction for the fifth phase, the cruise phase, is determined by taking the product of its intermediate fractions, as shown in Equation 4.10. Here, the total number of design points is denoted by n_D .

$$f_5 = \prod_{n=1}^{n_D} f_{5,n} \quad 4.10$$

Ultimately, the total fuel weight, W_F , is given by the total change in mass during the seven basic flight phases multiplied by the reserve fuel fraction, $f_{reserve}$, to account for the remaining reserve fuel, see Equation 4.11.

$$W_F = f_{reserve} \cdot (1 - f_{total}) \cdot W_M \quad 4.11$$

4.4 Sensitivity Analysis: Automatic Differentiation

For the sensitivity information computation of the methods discussed in this chapter the numerical approach of Automatic Differentiation (AD) [50] can be used. AD utilizes the fact that a computer program operates based on a set sequence of elementary arithmetic operations, e.g. addition, subtraction, multiplication, and division. Applying the chain rule to this set sequence of operations, the derivatives can be computed for an arbitrary order. Implementing AD will only slightly increase the number of operations required compared to the original program. The details of the sensitivity analysis will be discussed further in Section 5.3.

Verification

The verification data of the AD sensitivities concerning the fuel and design weights is listed in Table 4.2. As is evident from this table, the sensitivity information computed using the AD approach is very accurate and can be used for all its intended purposes.

Table 4.2: Verification of the automatic differentiation sensitivities.

Sensitivity	Automatic Differentiation	Finite Difference	Ratio
$\partial W_F / \partial C_D$	3.62985E6	3.61853E6	0.997
$\partial W_F / \partial C_L$	-2.15165E5	-2.14810E5	0.998
$\partial W_F / dW_M^*$	0.24411	0.24411	1.000
$\partial W_N / \partial C_D$	-1.94631E6	-1.94327E6	0.998
$\partial W_N / \partial C_L$	1.15371E5	1.15170E5	0.998
$\partial W_N / \partial W_M^*$	0.86423	0.86423	1.000

5

Optimization Setup

Wing design is a prime example of a multi-disciplinary problem. In order to illustrate *why*, the design problem is provided, albeit simplified, as follows. The structural discipline is responsible for sizing the wing structure such that it can withstand the aerodynamic loads introduced on the wing. The aerodynamic discipline is tasked with the determination of the aerodynamic loads acting on the wing during flight conditions. The flight conditions for a specific flight phase are provided by the performance discipline which determines the fuel weight and required lift to maintain steady flight. Here, the fuel weight is influenced by the wing structural weight and the aerodynamic performance. Evidently, all the involved disciplines are dependent on one another which is the definition of a multi-disciplinary problem. The field of research which focuses on these kind of multi-disciplinary problem definitions for optimizations is aptly named Multi-disciplinary Design Optimization (MDO).

For the proper implementation of an MDO problem the choice as to how to structure the different discipline analysis, analysis tools, and problem formulation is of paramount importance. The combination of these key elements is also referred to as the optimization architecture. This architecture defines the coupling between the different disciplines and how the optimization problem will be approached. There are many different architectures which can be used for solving MDO problems, a recent overview of which has been published by Martins & Lambe [51].

This section provides the details of the used optimization architecture as well as the general optimization problem formulation as used throughout this thesis. The choice of optimization architecture will be explained in Section 5.1, a summary of the relevant architectures will be provided and their benefits and limitations discussed. Once the architecture details have been covered, the optimization problem formulation as used for this thesis is detailed in Section 5.2. Lastly, the details and different methods used for the sensitivity analysis are discussed in Section 5.3.

5.1 Multi-disciplinary Design Optimization Architectures

For this research, the Individual Discipline Feasible (IDF) architecture will be used. In order to explain the reasoning for using this architecture, while also providing the details of the architecture, a summary of all four monolithic optimization architectures discussed in Martins & Lambe [51] is provided in this section. Distributed architectures - architectures that decompose the problem into multiple smaller sub-problems - have not been considered since the scope of the discussed optimization is already small and these architectures would have no added benefit.

The monolithic optimization architectures are summarized using the mathematical definition of the architecture, while also providing the associated eXtended Design Structure Matrix (XDSM) and stating the pros and cons of the architecture. The details on how to interpret these mathematical definitions and XDSMs will be explained in the following subsection.

5.1.1 All-At-Once

The fundamental architecture is known as the All-At-Once (AAO) approach. The AAO architecture contains the most basic definition of an optimization. It includes all coupling variables, surrogate variables, state

variables, consistency constraints, and residuals of the governing equations directly in the problem statement. The problem statement of the AAO architecture is provided in Equation 5.1. For the other architectures discussed in this section the AAO approach is used as the baseline to which adjustments are made to achieve the alternative definitions.

$$\begin{aligned}
& \text{minimize} && F(X, Y) \\
& \text{with respect to} && X, \hat{Y}, Y, \bar{Y} \\
& \text{subject to} && C_0(X, Y) \leq 0 \\
& && C_i(X_0, X_i, Y_i) \leq 0 && \text{for } i = 1, \dots, N \\
& && C_i^c = \hat{Y}_i - Y_i = 0 && \text{for } i = 1, \dots, N \\
& && R_i(X_0, X_i, \hat{Y}_{j \neq i}, \bar{Y}_i, Y_i) = 0 && \text{for } i = 1, \dots, N
\end{aligned} \tag{5.1}$$

The goal is to minimize the objective function, F , which is a function of the design variables, X , and the coupling variables, Y . The design variables are quantities in the MDO problem that are always under explicit control of the optimizer. These are the variables that the optimizer can influence to minimize the objective function. The coupling variables are determined by, and exchanged between, the various disciplines in order to model the interaction between them.

Internally, the system is also influenced by state variables, \bar{Y} , and surrogate variables, \hat{Y} . State variables, as the name suggests, define the state the system is in. The surrogate variables are used to enable the independent, and potentially parallel, analysis of the disciplines. These variables replace the coupling variables that would normally be determined by the discipline analysis and are under explicit control of the optimizer, i.e. they are an independent copy of the discipline its coupling variables. Each pair of coupling and surrogate variable is accompanied by a consistency constraint, C_i^c , which enforces that the calculated value of the coupling variable matches the surrogate variable value, i.e. consistency.

Additionally, the optimization is subject to design constraints, C , and the governing equations of the various disciplines in residual form, R_i , where i ranges from one to the total number of disciplines, N . The convention has been adopted to only consider “less than or equal to” inequality constraints to keep the mathematical definition compact. As the sign of a “greater than or equal to” constraint can simply be switched to turn it into a “smaller than or equal to” constraint there is no loss of generality by using this convention.

The above problem statement differentiates between so-called *local* and *shared* discipline variable groups. The local discipline variables are only used during the analysis of one specific discipline i . The shared discipline variables are used for multiple discipline analyses and are indicated by a subscript zero, e.g. X_0 . For the design variables, the coupling variables, the state variables, the design constraints, and the consistency constraints their respective shared and local discipline variable groups are concatenated as shown in Equation 5.2.

$$\begin{aligned}
X &= [X_0, X_1, \dots, X_N] && \text{for } i = 1, \dots, N \\
Y &= [Y_0, Y_1, \dots, Y_N] && \text{for } i = 1, \dots, N \\
\bar{Y} &= [\bar{Y}_0, \bar{Y}_1, \dots, \bar{Y}_N] && \text{for } i = 1, \dots, N \\
C &= [C_0, C_1, \dots, C_N] && \text{for } i = 1, \dots, N \\
C^c &= [C_0^c, C_1^c, \dots, C_N^c] && \text{for } i = 1, \dots, N
\end{aligned} \tag{5.2}$$

The details of the implementation of an optimization are not trivial to illustrate. The use of an algorithm or flow chart to assist in explaining the implementation of an optimization has often been found lacking as it does not describe the data flow between the different components. Hence, Lambe & Martins [52] introduced the XDMS which is an extension on the Design Structure Matrix (DSM) by Steward [53] (the DSM was later revisited by Browning [54] as well). The DSM shows the components of an optimization and the

connections between these components, the meaning of the connections is, however, not specified. To improve upon the DSM, the XDSM simultaneously communicates data dependency and process flow between computational components of MDO architectures in a single compact diagram. By providing the XDSMs, the implementation of the architectures is visualized. Hence, in addition to the previously discussed mathematical problem formulation, the associated XDSM will also be provided for each of the selected architectures.

The XDSM associated with the AAO approach is shown in Figure 5.1. As with the conventional DSM, in an XDSM the components of the architecture are positioned on the diagonal. Different block shapes are used to identify the computational analyses and the data connections: rectangles for generic processes and parallelograms for data input and data output. Unique to the XDSM, a special type of component is introduced, the so-called driver. A driver is a component which controls an iterative procedure and is identified by a rounded rectangle to distinguish it from the other components.

The data is positioned in the other fields of the matrix, where the components take input data in the vertical direction and provide output in the horizontal direction. The external input is defined on the outer edges of the matrix, i.e. the upper row and left-most column. Furthermore, the thick grey lines are used to highlight the *data* connections between components and the thin black lines are used to represent the *process* connections.

Each component is assigned a number; these identify the order in which they are executed, starting at zero. Additionally, loops can be defined using a driver component as $m \rightarrow n$, where $n > m$. The meaning behind this notation is that $m+1$ is not initiated before the sequence satisfies the conditions as set by the driver. The data blocks are also assigned a number to identify the step at which these are passed on to the next component.

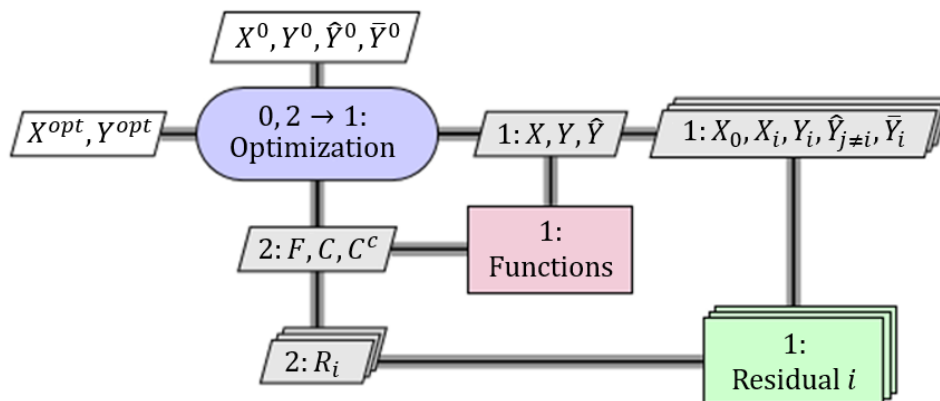


Figure 5.1: XDSM of the AAO architecture. Source: Martins & Lambe [51]

The XDSM associated with the AAO approach consists of three components: the driver, “Optimization”, which runs the components “Functions” and “Residual i ” in a loop until an optimum has been found that satisfies the constraints. The driver takes as input an initial vector containing starting values for the design variables, surrogate variables, coupling variables, and state variables. The driver is responsible for passing on these variables (updating them accordingly while the loop continues) so that the other components can determine the objective function, design constraint, consistency constraint, and discipline residual values. Once the driver criteria are met the result is an optimized design (shown in the left-most column as external data). The “Residual i ”-component referring to discipline i represent a repeated pattern for every discipline; meaning a residual block exists for every discipline and each block can be executed in parallel, this has been visualized by using a stack of components for this pattern. For the example XDSMs discussed throughout this section it has to be noted that gradient computation steps are not explicitly shown as they are not intrinsic to the architectures. [51]

5.1.2 Simultaneous Analysis and Design

Eliminating the consistency constraints from the AAO approach, by introducing a single group of coupling variables which replace the separate target and response groups, yields the Simultaneous Analysis and Design (SAND) architecture [55] which is represented by Equation 5.3. Eliminating these constraints reduces the problem size without compromising the performance of the optimization algorithm. This approach has the potential to quickly solve the optimization problem by exploring regions that are infeasible with respect to the analysis constraints, while not every iteration is required to solve any discipline analysis.

$$\begin{aligned}
 & \text{minimize} && F(X, Y) \\
 & \text{with respect to} && X, Y, \bar{Y} \\
 & \text{subject to} && C_0(X, Y) \leq 0 \\
 & && C_i(X_0, X_i, Y_i) \leq 0 \quad \text{for} \quad i = 1, \dots, N \\
 & && R_i(X_0, X_i, \bar{Y}_i, Y_i) = 0 \quad \text{for} \quad i = 1, \dots, N
 \end{aligned} \tag{5.3}$$

The XDMS associated with the SAND architecture is shown in Figure 5.2. As can be observed, the only difference with the AAO XDMS is the removal of the consistency constraints and the surrogate variables, since the surrogate variables are now replaced by a group of coupling variables, when compared to the XDMS of the AAO architecture. The data and process connections remain unaltered.

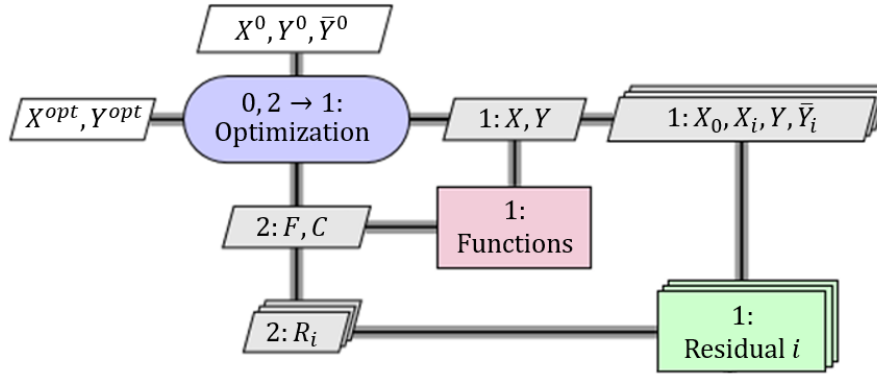


Figure 5.2: XDMS of the SAND architecture. Source: Martins & Lambe [51]

By using the SAND architecture, the discipline analyses are not required to be solved for every iteration. This allows the optimizer to consider infeasible regions in the design space which potentially solves the optimization problem faster than the AAO approach, where the discipline analyses need to be solved exactly for each iteration.

However, the problem formulation still requires all the state variables and discipline analysis equations. Problem size may still be an issue and termination of the optimization at an infeasible design, prematurely, may still occur. Additionally, because the discipline analysis equations are still included as constraints their residual values (and their derivatives in case of a gradient based optimization) need to be available. Providing the residuals and their gradient information proves difficult in practice as, in engineering design, most software for discipline analysis operates as a black-box, i.e. the coupling variables are directly computed while not providing the residuals and state variables.

5.1.3 Individual Discipline Feasible

By only removing the discipline analysis constraints from the AAO approach the Individual Discipline Feasible (IDF) architecture [56], also known as distributed analysis optimization [57] and optimizer-based decomposition [58], is achieved. The removal of these constraints is achieved by applying the implicit function theorem to the discipline analysis constraints which results in the state variables and coupling variables to become functions of the design variables and surrogate variables. The problem definition of the IDF architecture is provided in Equation 5.4.

The XDSM associated with the IDF architecture is shown in Figure 5.3. Here, the residuals for the respective disciplines are no longer required. The optimization has become a function of solely design variables and surrogate variables, while avoiding the introduction of an MDA driver.

$$\begin{aligned}
& \text{minimize} && F(X, Y(X, \hat{Y})) \\
& \text{with respect to} && X, \hat{Y} \\
& \text{subject to} && C_0(X, Y(X, \hat{Y})) \leq 0 \\
& && C_i(X_0, X_i, Y_i(X_0, X_i, \hat{Y}_{j \neq i})) \leq 0 \quad \text{for } i = 1, \dots, N \\
& && C_i^c = \hat{Y}_i - Y_i(X_0, X_i, \hat{Y}_{j \neq i}) = 0 \quad \text{for } i = 1, \dots, N
\end{aligned} \tag{5.4}$$

However, the process flow is not completely parallel; the analysis of the various disciplines is executed in parallel yet the functions can only be run once they have all been completed.

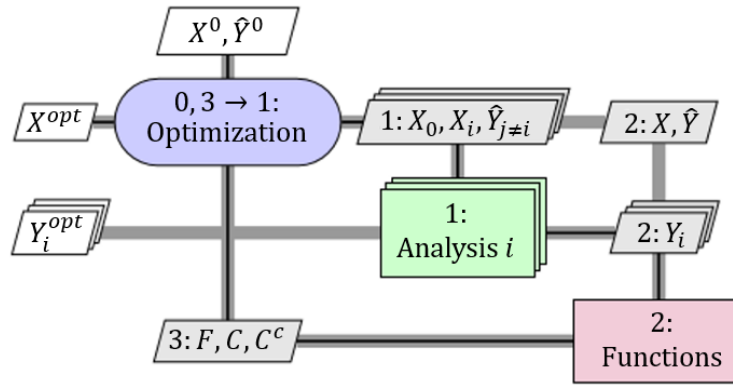


Figure 5.3: XDSM of the IDF architecture. Source: Martins & Lambe [51]

The benefit of using the IDF architecture is the elimination of all the state variables and discipline analysis equations from the problem definition. By using the IDF architecture the discipline analysis equations are solved at every iteration using surrogate variables, i.e. the coupling variables have become implicit functions of the design variables and surrogate variables. Additionally, the decoupling of the discipline analyses also allows them to be performed in parallel which can significantly improve the speed with which the problem is solved. Compared to the AAO and SAND architectures the IDF architecture results in a significantly smaller problem definition while utilizing existing discipline analyses software with minimal modifications.

It does have to be noted that the size of the problem may still be an issue. Although the discipline analyses constraints are removed, the surrogate variables and their consistency constraints are introduced. The resulting optimization may become too large to efficiently solve when too many surrogate variables are added in order to replace the discipline analyses constraints. This issue can be mitigated by strategically choosing which coupling variables to eliminate to reduce the number of coupling variables rather than completely eliminating them from the problem definition.

5.1.4 Multi-Disciplinary Feasible

In case both the analysis constraints and the consistency constraints are removed from the AAO approach the Multi-Disciplinary Feasible (MDF) approach [56], also known as fully integrated optimization [57] and nested analysis and design [59], is the resulting architecture. The problem definition of the MDF architecture is provided in Equation 5.5.

$$\begin{aligned}
& \text{minimize} && F(X, Y(X, Y)) \\
& \text{with respect to} && X \\
& \text{subject to} && C_0(X, Y(X, Y)) \leq 0 \\
& && C_i(X_0, X_i, Y_i(X_0, X_i, \hat{Y}_{j \neq i})) \leq 0 \quad \text{for } i = 1, \dots, N
\end{aligned}$$

5.5

The MDF XDSM is shown in Figure 5.4. In this XDSM the residuals for the respective disciplines are no longer required. The optimization has become a function of only design variables. Additionally, the process flow is no longer parallel and a secondary loop has been introduced for the discipline analyses; an internal Multi-Disciplinary Analysis (MDA) driver.

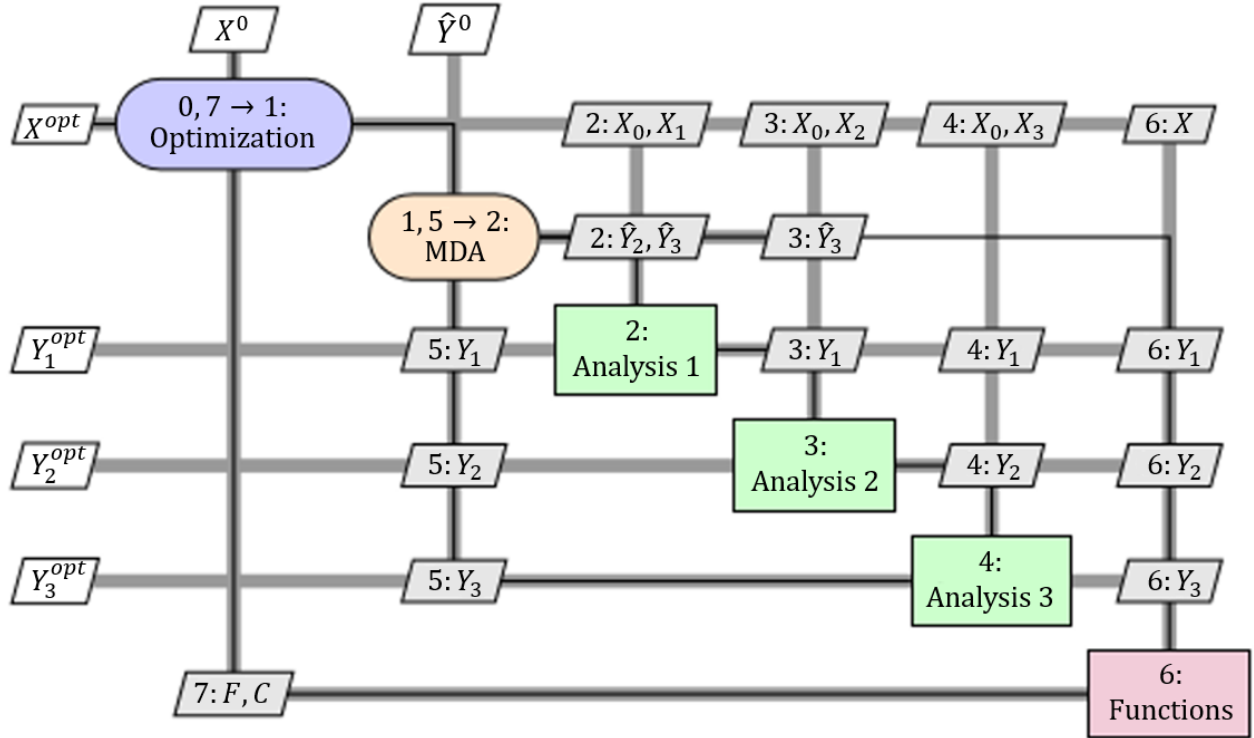


Figure 5.4: XDSM of the MDF architecture, reproduced from Martins & Lambe [51].

The advantage of this architecture is the reduced size of the optimization problem seeing as it is as small as it can be. Only the objective function, design variables, and design constraints are under the optimizer its direct control. Additionally, the optimizer always returns a feasible design which satisfies the consistency constraints, even when the process of optimization is ended prematurely.

The disadvantage of this architecture is related to the coupling variables. A consistent set of coupling variables needs to be computed for every iteration of the optimization, i.e. a full MDA is to be performed for every iteration. So, instead of running each discipline analysis only once - as is the case with the IDF architecture - they need to be evaluated until a consistent result is achieved. This process is computationally expensive and requires a specialized MDA which is also time-consuming to develop.

5.2 Optimization Problem Formulation

Now that the details of the IDF architecture have been discussed, it is time to define the optimization problem in the corresponding format. Similar to the previous section, the problem is formulated by providing the mathematical definition and the associated XDSM, only in this section they are not generalized and discussed in greater detail. The used optimizer and optimization algorithm will be discussed as well.

5.2.1 Architecture Choice

From the four discussed architectures, both the AAO and SAND architectures are computationally the fastest monolithic architectures. [60] However, the aerodynamic and structural analysis tools used in this research can be considered to be operating as black-boxes and this makes the implementation of these architectures difficult, if not impossible. The other two architectures, IDF and MDF, synergize more efficiently with this kind of black-box tools and are thus viable alternatives.

From these two architectures, the IDF architecture will ultimately be used. Previous publications, such as Hoogervorst [61], have shown that the IDF architecture is suitable for these kind of problem definitions. Another advantage, when compared to the MDF architecture, is the absence of the MDA driver; all discipline analyses only have to be performed once per design evaluation. Additionally, as long as the increase in number of design variables due to the addition of the surrogate variables is kept small, the IDF architecture has been found to be computationally cheaper than the MDF architecture. [60] For this research the number of surrogate variables can be kept to a minimum without introducing additional complications.

5.2.2 Mathematical Definition

The objective of the optimization is to minimize the MTOW, W_M , of the reference aircraft by optimizing the design variables while satisfying the design and consistency constraints. Because the IDF architecture is used and the MTOW itself is a coupling variable, the actual objective is the surrogate variable associated with the MTOW, W_M^* . The design vector consists of the wing sweep angle, Λ , the angle of attack, α , the SCB shape parameters, κ , the surrogate MTOW, W_M^* , and the surrogate fuel weight, W_F^* .

The optimization is subject to two design constraints and two consistency constraints. The first design constraint requires the calculated drag coefficient, C_D , to be equal to, or less than, the baseline drag coefficient, $C_{D,0}$, and the second ensures that the lift coefficient of the wing, C_L , is sufficient to maintain steady flight at the design point weight, W_D . Lastly, the consistency constraints are defined such that the surrogate variables are consistent with their respective coupling variables, as has been explained in Subsection 5.1.3. The resulting mathematical definition of this optimization is provided in Equation 5.6.

$$\begin{aligned} & \text{minimize} && W_M^*(X) \\ & && X = [\Lambda, \alpha, \kappa, W_M^*, W_F^*] \\ & \text{subject to} && C_D \leq C_{D,0} \\ & && C_L = W_D / (q \cdot S) \\ & && W_M^* = W_M \\ & && W_F^* = W_F \end{aligned} \tag{5.6}$$

5.2.3 Objective Function

As mentioned earlier, the surrogate variable for the aircraft MTOW, W_M^* , is used as the objective function. Because the surrogate variable is directly linked to the actual variable through a consistency constraint it behaves in an identical fashion and no distinction has to be made between them. The MTOW is defined as the sum of the structural wing weight, W_W , the fuel weight, W_F , and the aircraft-less-wing weight, W_{A-W} , as is shown in Equation 5.7.

$$W_M = W_W + W_F + W_{A-W} \tag{5.7}$$

Here, the wing weight is determined by the structural analysis (discussed in Chapter 3) and the fuel weight is calculated by the performance analysis (discussed in Chapter 4). Additionally, the performance analysis requires the aerodynamic coefficients of the wing, determined by the aerodynamic analysis (discussed in Chapter 2). The aircraft-less-wing weight is the weight of the aircraft without any fuel and excluding the wing structure. This weight is assumed to be constant and is determined only once, for the reference aircraft, as will be mentioned in Chapter 6. Because the MTOW has these dependencies on the different disciplines it is a suitable parameter to use for the objective function of this MDO.

Lastly, all parameters used by the optimizer are normalized because the convergence rate is better bounded when the ratio of largest and smallest eigenvalues of the Hessian is small and, typically, when the parameters are normalized this ratio is close to 1 (which would be optimal). The normalized objective function is shown in Equation 5.8.

$$F(X) = \frac{W_M^*}{W_{M,0}} \quad 5.8$$

5.2.4 Design Variables

The design vector of this optimization consists of three groups of variables. The first being all variables defining the flight conditions, which for this optimization consists solely of the angle of attack. The variables that influence the geometry of the wing belong to the second group, these are the sweep and SCB shape design variables. Lastly, there is the group of the surrogate variables which have been introduced to decouple the disciplines, as was explained in Subsection 5.1.3. The surrogate MTOW and surrogate fuel weight belong to this last category.

Angle of Attack

The angle of attack, a local design variable to the aerodynamic analysis, determines the orientation of the wing with respect to the incoming flow and is the only flight condition that is allowed to be varied during the optimization. By including it as a design variable, control of the aerodynamic coefficients at the design point is given to the optimizer. It is mainly used to ensure that sufficient lift is being generated by the wing to maintain steady flight at the design point, while taking into account the corresponding drag that is being generated at this point.

During the determination of the loads for the structural analysis, the orientation of the wing is based on the required lift at the chosen load case. Hence, no additional angle of attack variable is required for the load determination.

Sweep

The sweep variable is a global design variable which is being used for both the aerodynamic analysis and the structural analysis. By including the sweep as a design variable, the optimizer is able to directly influence the resulting structural wing weight while also accounting for the influence the variable has on the aerodynamic coefficients of the wing.

For the aerodynamic analysis, this variable is used to set the leading edge sweep of the wing mesh by deforming the mesh using the Free-Form Deformation (FFD) strategy. The details of this FFD strategy are provided in Section 2.2.

During the structural analysis, the sweep variable is used to update the wing planform definition so that it matches the wing mesh. Consequently, the planform determines the dimensions of the wing box and the fuel tank, the engine location, and the location of the airfoil sections that are being used for the load determination using the Q3D-solver.

Shock Control Bump Shape Parameters

The SCB shape variables, local to the aerodynamic analysis, are used to specify the location, shape, and number of the SCBs positioned on the upper surface of the wing. The shape of the SCB(s) is introduced to the mesh by deforming the wing upper surface of the mesh using the FFD strategy, the details of which are discussed in Section 2.2. Due to the nature of the FFD format a large degree of freedom can be given to the optimizer in terms of possible SCB shapes. The inclusion of the shape variables allows the optimizer to add, position, and size 2-D and/or 3-D SCBs while keeping track of any beneficial, or detrimental, effects they may have on the aerodynamic coefficients of the wing. The main goal of these shape variables is to allow the optimizer to size the SCB(s) such that they decrease the drag coefficient as much as possible while keeping track of the influence the addition of the SCBs have on the lift coefficient.

Surrogate Variables

The surrogate variables for this optimization are limited to two, one for the fuel weight and one for the MTOW. These variables have been strategically chosen in order to avoid any unnecessary increase in problem size. Both the wing lift and wing drag coefficients would also be replaced by surrogate variables if all coupling variables were to be replaced. The purpose of these surrogate variables has been explained in Section 5.1.3.

5.2.5 Design Constraints

As has been stated earlier, this optimization is subject to two design constraints. The first design constraint is related to the wing drag coefficient and will, from now on, be referred to as the *drag constraint*. The other design constraint is related to the lift produced by the wing and the lift required to maintain steady flight at the design point, this constraint will be referred to as the *lift constraint* from this point forward.

Drag Constraint

The drag constraint is an inequality constraint that has been added to ensure that the optimized wing design has an equal, or even improved, drag coefficient when compared to the baseline wing. This requirement on the optimized design ensures that it is similar to the reference design. For example, there will be no need for more powerful engines to overcome an increase in drag because the drag levels will be similar between the two designs. Since, generally speaking, more powerful engines weigh more and would inevitably result in a weight increase which has to be avoided as it will not be taken into account in this optimization. The normalized definition of the drag constraint is provided in Equation 5.9.

$$C^{drag} = \frac{C_D}{C_{D,0}} - 1 \leq 0 \quad 5.9$$

Here, the normalized value of the drag constraint is obtained by dividing the wing drag coefficient, C_D , with the wing drag coefficient of the reference wing, $C_{D,0}$.

Lift Constraint

The lift constraint is an equality constraint which states that the lift generated at the design point needs to be equal to the design weight. The addition of this constraint ensures that the steady horizontal flight condition at the design point is maintained, while taking into account the weight reduction at the design point due to potential wing and fuel weight decreases. The lift generated by the wing is calculated using Equation 5.10.

$$L = \left(\frac{1}{2} \cdot \rho_{cr} \cdot V_{cr}^2 \cdot S_{wing} \right) \cdot C_L \quad 5.10$$

Here, the air density at cruise altitude, ρ_{cr} , the cruise flight speed, V_{cr} , and the wing wetted area, S_{wing} , are constants; none of the defined design variables influence them. Hence, the lift generated by the wing is only a function of the wing lift coefficient, C_L . Consequently, the normalized lift constraint is obtained by dividing the generated lift, L , with the design weight, W_D , as shown in Equation 5.11.

$$C^{lift} = \frac{L}{W_D} - 1 = 0 \quad 5.11$$

5.2.6 Consistency Constraints

In addition to the design constraints, there are also two consistency constraints. Both these constraints are, by definition, of the equality form. The first consistency constraint ensures that the surrogate and actual values of the fuel weight, W_F , are equal and the second ensures the same for the MTOW, W_M , and surrogate MTOW, W_M^* . The normalized constraints for the fuel and maximum take-off weights are illustrated in Equation 5.12 and Equation 5.13, respectively.

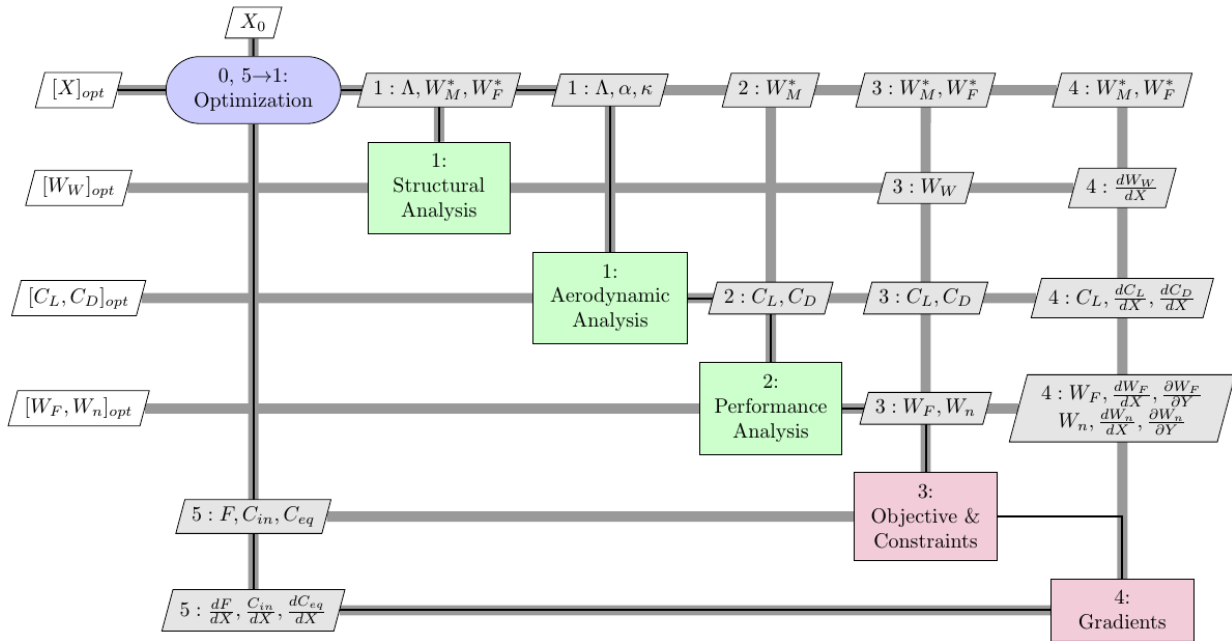
$$C_c^{W_F^*} = \frac{W_F^*}{W_F} - 1 = 0 \quad 5.12$$

$$C_c^{W_M^*} = \frac{W_M^*}{W_M} - 1 = 0 \quad 5.13$$

Here, both constraints have been normalized by dividing the surrogate values with the respective calculated values.

5.2.7 Extended Design Structure Matrix

Now that the details of the IDF architecture and the optimization problem formulation have been discussed, the corresponding XDSM can be introduced, see Figure 5.5. In this XDSM the flow of design variables is illustrated in the top most row. Apart from the design variables there are still two coupling variables, these are being passed down from the aerodynamic analysis to the performance analysis. Because these coupling variables have not been converted to sets of surrogate variables and consistency constraints, the performance analysis cannot be executed in parallel with the other disciplines. However, the analysis of the performance is extremely cheap in terms of computational cost, which was evident from Chapter 4. Hence, the impact of the loss of parallel execution for this particular discipline is minimal.



It has to be noted that this XDSM, in contrast to the previously discussed XDSMs, does include the component for the gradient computation. The previously discussed XDSM were generalized examples and including a component for the gradient information was obsolete; it would not assist in highlighting the unique aspects of each architecture. However, for this optimization the implementation of the gradient computation is of paramount importance and that is why the component has been included.

Lastly, in order to further enhance computational efficiency, the optimizer skips the *Gradient*-component when it has already determined - based on the results from the *Objective & Constraints*-component - that the objective and constraint values of the current design are not within acceptable limits. Instead, the step size is updated using the gradient information of the previous iteration and the next loop continues at the first step of the optimization loop.

5.2.8 Optimizer

The MATLAB-function *fmincon* will be used as optimizer. This function is described as a non-linear programming solver; it finds the minimum of a constrained, non-linear, and multi-variable function. It expects a problem in the form of Equation 5.14 for which it will find the minimum.

Here, the objective function, F , can be subject to inequality constraints, C , equality constraints, Ceq , linear inequality constraints, $A \cdot X$, and linear equality constraints, $Aeq \cdot X$. Additionally, the design variables, X , can be bound by both lower bounds, lb , and upper bounds, ub .

$$\begin{aligned}
& \text{minimize} && F(X) \\
& \text{subject to} && C(X) \leq 0 \\
& && Ceq(X) = 0 \\
& && A \cdot X = b \\
& && Aeq \cdot X = beq \\
& && lb \leq X \leq ub
\end{aligned} \tag{5.14}$$

As an additional requirement, the optimizer needs to be capable of gradient-based optimization. The *fmincon*-function is capable of gradient-based optimization in two approaches. Either the gradient information for all constraints and the objective function are provided by a user defined function, or the function determines the gradient by itself using either a forward or central finite difference method. For this research the gradient information will be determined by user defined functions, the specifics of the sensitivity analysis will be discussed in Section 5.3.

Sequential Quadratic Programming

For this optimization, the Sequential Quadratic Programming (SQP) algorithm, which is one of the algorithms *fmincon* is familiar with, will be used. This algorithm is one of the most successful algorithms for solving non-linear constrained optimization problems. [62] The SQP algorithm is a procedure that generates iterates converging to a solution of the problem by solving quadratic programs that are approximations to Non-Linear Problems (NLPs). In its many implemented forms, this method has been shown to be a very useful tool for solving non-linear programs, especially where a significant degree of non-linearity is present. The SQP algorithm is typically gradient based and applicable to all sizes of non-linear programming problems.

Optimality Conditions

When a gradient based algorithm such as SQP is being used, there is a set of conditions which can be checked in order to confirm if a candidate for an optimum is a local optimum. These are the Karush-Kuhn-Tucker (KKT) conditions. The KKT conditions can be divided into the stationary point condition, the feasibility condition, and the complementarity condition. Each of these conditions will be discussed briefly.

The stationarity condition uses the auxiliary Lagrangian function which is provided in Equation 5.15. Here, the Lagrange multiplier vector, λ , is the concatenation of the Lagrange multiplier for inequality constraints, λ_{in} , and the Lagrange multiplier for equality constraints, λ_{eq} . Hence, the length of this vector is equal to the total number of constraints. Following this definition, the stationarity condition is given by Equation 5.16.

$$L(X, \lambda) = F(X) + \sum \lambda_{in} \cdot C_{in}(X) + \sum \lambda_{eq} \cdot C_{eq}(X) \tag{5.15}$$

$$\nabla_X L(X, \lambda) = 0 \tag{5.16}$$

The feasibility condition is provided in Equations 5.17. This condition simply requires that both the inequality and the equality constraints are met at the candidate optimum and the Lagrange multiplier associated with the inequality constraints is equal to, or greater than, zero.

$$\begin{cases} C_{in}(X) \leq 0, \\ C_{eq}(X) = 0, \\ \lambda_{in} \geq 0 \end{cases} \tag{5.17}$$

The complementarity condition is provided in Equation 5.18. In order to be satisfied, this condition requires that the Lagrange multipliers do not increase the optimality condition further.

$$\lambda_{in} \cdot C_{in}(X) = 0 \tag{5.18}$$

When all the KKT conditions are satisfied, the sufficient condition will need to be satisfied in order to verify that the candidate is not only a feasible stationary point but also an optimum. The sufficient condition is provided in Equation 5.19. This condition checks whether the objective and the feasible domain are locally convex.

$$\partial X \cdot \frac{\partial^2 L}{\partial X^2} \cdot \partial X > 0 \quad 5.19$$

5.3 Sensitivity Analysis

Using a gradient based optimization, the computational cost of the optimization can be drastically improved by providing additional information to the optimizer to improve the search direction. There are various options for determining the sensitivity information of the design variables. For this research the methods used consist of: AD for the performance analysis (previously discussed in Section 4.4), continuous adjoint method for the aerodynamic analysis (previously discussed in Subsection 2.3), and FDM for the structural analysis (as mentioned in Chapter 3).

Objective Function

The sensitivity of the objective function, defined earlier in Equation 5.8, with respect to the design vector is given by Equation 5.20. This sensitivity can be determined mathematically as the derivative of a surrogate variable with respect to the design vector is simply zero, except for the surrogate variable itself which, of course, has a one-to-one relationship.

$$\frac{dF(X)}{dX} = \frac{1}{W_{M0}} \cdot \frac{dW_M^*}{dX} \quad 5.20$$

Drag Constraint

The sensitivity of the drag constraint, defined earlier in Equation 5.9, with respect to the design vector is given by Equation 5.21. The surrogate variables have no influence on the value of the drag coefficient. The angle of attack, sweep, and SCB shape variables do influence the drag coefficient and their sensitivities can be computed using the continuous adjoint approach. However, an exception is made for the sensitivity with respect to the sweep variable because of an issue with the continuous adjoint implementation in SU². This issue results in erroneous gradient information, which has already been discussed in detail in Section 2.3. Because of this issue, the sensitivity with respect to the sweep variable will be determined using FDM.

$$\frac{dC_D}{dX} = \frac{1}{C_{D0_n}} \cdot \frac{dC_{D_n}}{dX} \quad 5.21$$

Lift Constraint

The sensitivity of the lift constraint, defined earlier in Equation 5.11, with respect to the design vector is given by Equation 5.22 in combination with Equation 5.23. The sensitivities of the lift coefficient are determined using the same approach as for the drag coefficient. The partial derivatives of the design weight with respect to the lift coefficient, drag coefficient, and surrogate MTOW are determined using AD.

$$\frac{dC_L}{dX} = \frac{q_{cr} \cdot S_{wing}}{W_n} \cdot \left(\frac{dC_{L_n}}{dX} - \frac{C_{L_n}}{W_n} \cdot \frac{dW_n}{dX} \right) \quad 5.22$$

$$\frac{dW_n}{dX} = \frac{\partial W_n}{\partial C_{L_n}} \cdot \frac{dC_{L_n}}{dX} + \frac{\partial W_n}{\partial C_{D_n}} \cdot \frac{dC_{D_n}}{dX} + \frac{\partial W_n}{\partial W_M^*} \cdot \frac{dW_M^*}{dX} \quad 5.23$$

Consistency Constraints

The sensitivity of the surrogate fuel weight constraint, defined earlier in Equation 5.12, with respect to the design vector is given by Equation 5.24 and Equation 5.25.

$$\frac{dC_c^{W_F^*}}{dX} = \frac{1}{W_F} \cdot \frac{dW_F^*}{dX} + \frac{W_F^*}{W_F^2} \cdot \frac{dW_F}{dX} \quad 5.24$$

$$\frac{dW_F}{dX} = \frac{\partial W_F}{\partial C_{L_n}} \cdot \frac{dC_{L_n}}{dX} + \frac{\partial W_F}{\partial C_{D_n}} \cdot \frac{dC_{D_n}}{dX} + \frac{\partial W_F}{\partial W_M^*} \cdot \frac{dW_M^*}{dX} \quad 5.25$$

The sensitivity of the surrogate MTOW constraint, defined earlier in Equation 5.13, with respect to the design vector is given by Equation 5.26 and Equation 5.27.

$$\frac{dC_c^{W_M^*}}{dX} = \frac{1}{W_M} \cdot \frac{dW_M^*}{dX} + \frac{W_M^*}{W_M^2} \cdot \frac{dW_M}{dX} \quad 5.26$$

$$\frac{dW_M}{dX} = \frac{dW_F}{dX} + \frac{dW_W}{dX} \quad 5.27$$

As mentioned earlier, the sensitivity of surrogate variables can simply be determined mathematically. The partial derivatives of the fuel weight are determined using AD. For the wing weight the sensitivities are computed using FDM.

6

Test Case Application

Now that the MDO formulation has been explained and all the discipline analysis have already been discussed, the aircraft model and characteristics that will be used to perform the optimizations can be introduced as well as the details and results of the various optimizations that have been executed using this model.

In this chapter the details of the test case aircraft are first introduced in Section 6.1. Then, the formulations of the various optimizations will be reported in Section 6.2 and, once the optimization definitions have been covered, their respective results will be discussed in Section 6.3.

6.1 Test Case Aircraft

The Airbus A320 has been chosen as the reference aircraft, which is a medium range civil air transport aircraft operating in the transonic flight speed regime. Beyond these requirements, this aircraft also meets the criteria of having a moderately swept wing. Additionally, the planform, airfoil, and operating data is readily available in Obert [63] and IHS [64].

6.1.1 Aircraft Characteristics

Each of the discipline analysis requires additional data regarding the reference aircraft to accurately perform the analysis. For example, the structural discipline requires the never to exceed Mach number in order to compute the loads acting on the wing, the aerodynamic discipline needs the cruise Mach number so that the analysis is performed for the appropriate conditions, and the performance discipline requires the MTOW in order to determine the fuel weight. The aircraft characteristics of the A320 that will be used throughout this research are provided in Table 6.1.

Table 6.1: Characteristics of the Airbus A320. [63] [64]

Characteristic	Symbol	Value	Unit
MTOW	W_M	721 035	[N]
Never exceed Mach number	M_{NE}	0.89	[-]
Cruise Mach number	M_{cr}	0.78-0.80	[-]
Cruise altitude	h_{cr}	11 280	[m]
Lift-to-drag ratio at mid-cruise	L/D_{cr}	16.81	[-]
Mission range	R	4 800 000	[m]
Engine weight	W_E	24 082	[N]

6.1.2 Baseline Wing

The wing of the reference aircraft is defined by the planform data as presented in Table 6.2, in this table the X-, Y-, and Z-coordinates are defined at the leading edge of the respective spanwise locations. Using the geometric data from this table the planform of the wing can be generated, which is shown in Figure 6.1. For this research the twist angle will not be considered in order to maintain consistency with a related thesis project that is running in parallel.

Table 6.2: Geometric definition of the A320 wing. [63]

Location	X _{LE} [m]	Y _{LE} [m]	Z _{LE} [m]	Chord [m]	Twist [°]
Root	0.0	0.0	0.0	7.0518	0.0
Kink	3.3006	6.3403	0.5547	3.7584	-2.5
Tip	8.8306	16.9635	1.4841	1.4958	-2.5

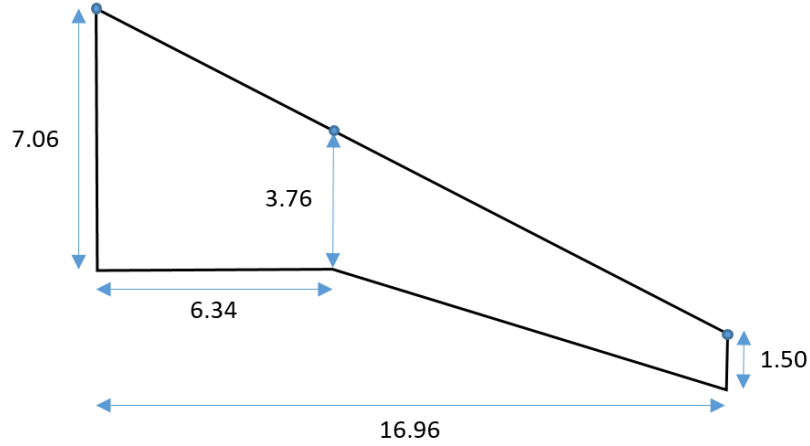


Figure 6.1: Planform of the reference A320 wing, dimensions in meter.

In order to model the entire reference wing, the airfoil shapes at several spanwise locations are also required in addition to this planform data. The airfoil sections are defined at four span-wise positions using ten CST coefficients for each airfoil: five coefficients for the upper and five coefficients for the lower curve. These CST coefficients are shown in Table 6.3 and the corresponding airfoil shapes are presented in Figure 6.2.

Table 6.3: CST coefficients defining the airfoil shapes at four span-wise stations.

Location	Upper CST Coefficients					Lower CST Coefficients				
0.00 η	0.2021	0.1175	0.2342	0.2067	0.2841	-0.1265	-0.1101	-0.3012	-0.1164	0.1813
0.33 η	0.1849	0.1072	0.2216	0.1780	0.2817	-0.1529	0.0026	-0.4241	0.1435	-0.0779
0.66 η	0.1635	0.1116	0.1996	0.1664	0.2751	-0.1617	0.0170	-0.4009	0.1635	-0.0979
1.00 η	0.1542	0.1051	0.1955	0.1603	0.2673	-0.1410	-0.0371	-0.2335	-0.0791	0.1702

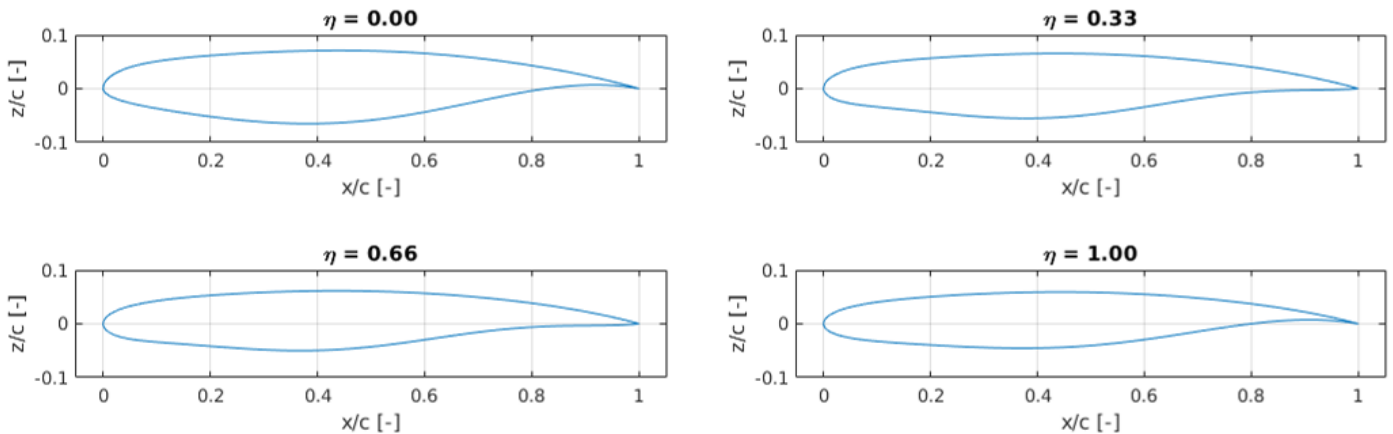


Figure 6.2: Airfoil shapes of the reference A320 wing at four spanwise stations.

6.1.3 Wing box Dimensions

In addition to the wing model, the layout of the wing box and fuel tank, the engine weight, and the engine location need to be determined in order to be able to estimate the weight of the wing structure accurately. The wing box dimensions are determined by the location of the front and rear spar; these are provided in

Table 6.4. These locations also determine the dimensions of the fuel, combined with a spanwise start and end point. The fuel tank is assumed to start at 0.10η and end at 0.90η . As for the engines, they have been determined to weigh 2454.8 kilograms each and are positioned at 0.35η ; one per wing. The wing box dimensions, fuel tank dimensions, engine weight, and engine location are kept constant with respect to the wing throughout the optimizations.

Table 6.4: Chord-wise position of the front and rear spar.

Location	Front spar position	Rear spar position
Root	$0.10c_{root}$	$0.61c_{root}$
Kink	$0.16c_{kink}$	$0.63c_{kink}$
Tip	$0.22c_{tip}$	$0.55c_{tip}$

6.1.4 Surface & Volume Mesh

The initial surface and volume mesh consists of the domain surfaces, the wing surfaces, and the volume grid. The domain consists of upper wall, lower wall, outer wall, inlet, outlet, and symmetry plane surfaces. It is sized such that the lift and drag coefficients can be assumed to be independent of the domain dimensions, i.e. an increase in one of the domain dimensions by 10% does not influence the coefficients by more than 0.1%. The resulting domain dimensions are found to be a length of 650 meter, a width of 250 meter, and a height of 600 meter. Here, the wing is positioned so that the wing its root leading edge, coinciding with the origin, is on the symmetry plane, 150 meter from the inlet, and equidistant from the upper and lower. An illustration of the volume mesh is provided in Figure 6.3. Cross-sections of the volume mesh at the wing root and tip are provided in Figure 6.4 and Figure 6.5, respectively.

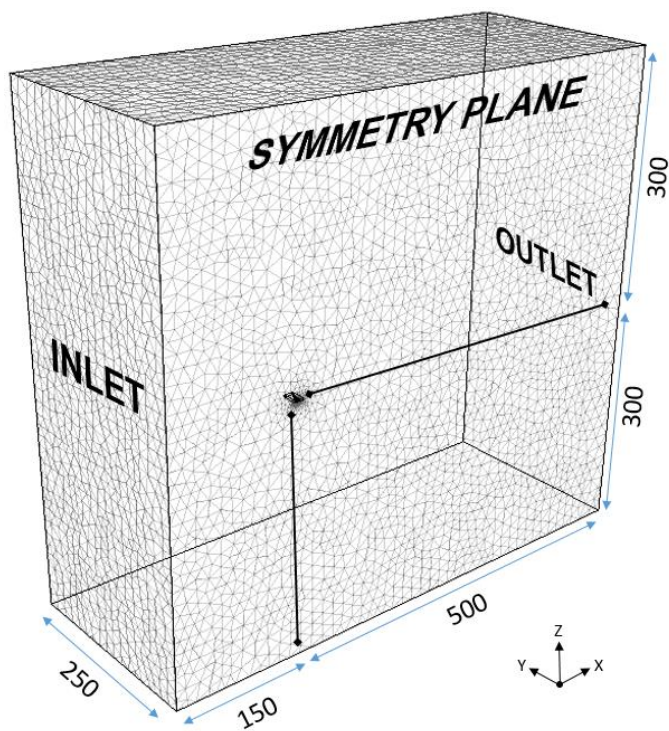


Figure 6.3: Illustration of the volume mesh, dimensions in meter.

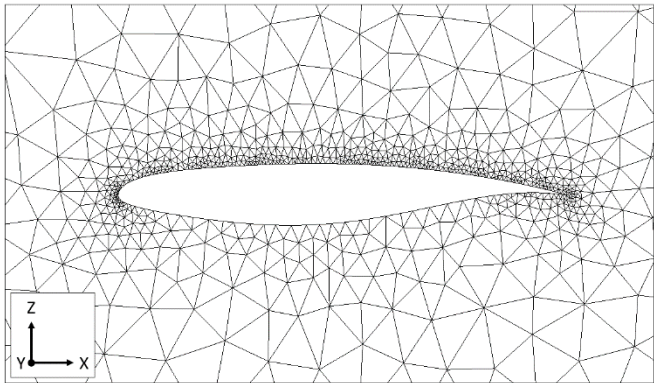


Figure 6.4: Cross-section of the volume mesh at the root.

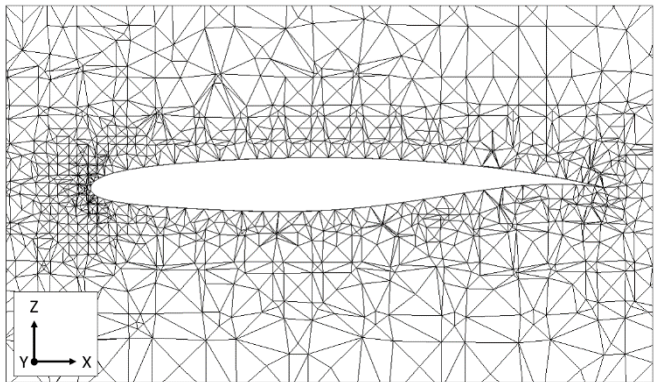


Figure 6.5: Cross-section of the volume mesh at the tip.

The surface mesh of the wing consists of an upper surface, lower surface, tip surface, and trailing edge curve. These entities are constructed using the airfoil shapes at the root, kink, and tip positions and the corresponding leading edge locations. The maximum element size for each of the surfaces associated with either the domain or wing is determined in a similar fashion as used for the domain dimensions, i.e. for a

given increase in maximum element size for a surface the influence on the aerodynamic coefficients is less than 0.1%. Additionally, after determining the maximum element size for the upper surface it is consequently pre-emptively lowered in order to ensure the mesh quality once an arbitrary SCB shape deformation has been applied. Illustrations of the upper and lower surface meshes are respectively provided in Figure 6.6 and Figure 6.7. The tip surface mesh is shown in Figure 6.8.

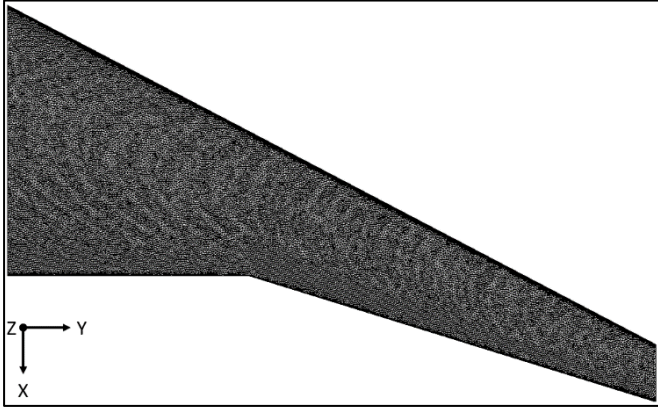


Figure 6.6: Top view of the upper surface mesh.

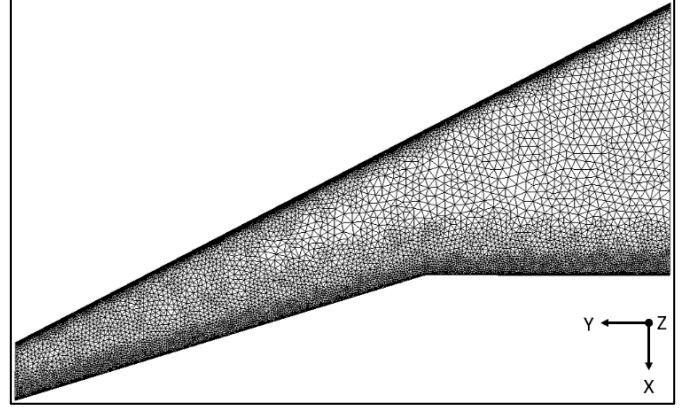


Figure 6.7: Bottom view of the lower surface mesh.

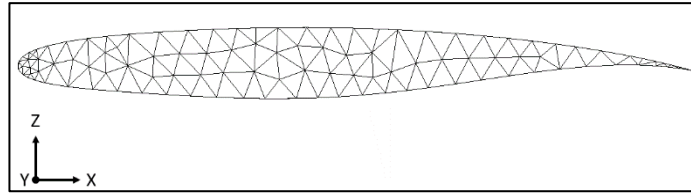


Figure 6.8: Side view of the tip surface mesh.

6.2 Optimization Formulations

At this point the optimization architecture, definition, and model have been introduced and the details of the various discipline analyses have also been discussed. Now, a series of optimizations will be introduced which will be executed in order to answer the research questions associated with the research objective that were defined in Chapter 1. A total of seven optimizations will be executed, these are discussed in the following subsections. Please note that, although the formulation of the mentioned optimization may be adjusted, the XDSM as discussed in Subsection 5.2.7 still applies to all of the optimizations.

For all sets of optimizations considering both 2-D and 3-D SCB designs the only difference between the 2-D SCB and 3-D SCB definition is the set of active SCB shape variables, κ . The details of this difference were discussed earlier in Section 2.2.

6.2.1 Shock Control Bump Shape Optimization

The first two optimizations, referred to as the 2-D and 3-D SCB *shape optimizations*, focus on verifying the geometry parameterization for the 2-D and 3-D SCB shapes, respectively. To this end, a simplified version of the optimization formulation from Section 5.2 is performed. The definition is simplified by removing the sweep angle from the design variables and, as a consequence, also removing the drag constraint from the design constraints. The surrogate variable constraints are, of course, still required in order to maintain consistency between surrogate and coupling variable sets. The final mathematical definition for the SCB shape optimization is shown in Equation 6.1. The shape optimizations consider a single design point.

$$\begin{aligned}
& \text{minimize} && W_M^*(X) \\
& && X = [\alpha, \kappa, W_M^*, W_F^*] \\
& \text{subject to} && C_L = W_D / (q_{cr} \cdot S_{wing}) \\
& && W_M^* = W_M \\
& && W_F^* = W_F
\end{aligned} \tag{6.1}$$

The sweep angle has been removed from the design variables in order to isolate the influence of the SCB shape variables. Since the sweep variable is the only variable that requires the FDM for gradient computation, removing it has the added benefit of reducing the computational cost of the optimization as well. It is also the only variable which directly influences the structural wing weight. Hence, an improved aerodynamic performance is the only approach to reduce the objective function. The only structural weight reduction will be through the snowball-effect, e.g. improved aerodynamic performance reduces the total fuel weight and MTOW which results in lower loads acting on the wing during the critical load case.

Because an improvement in aerodynamic performance is the only means to reduce the objective function, and the lift constraint is still required to ensure steady horizontal flight, the drag constraint becomes redundant since reducing the drag coefficient is the only feasible approach to achieve improved performance.

6.2.2 Single-point Low Sweep Design Optimizations

The next set of optimizations, referred to as the 2-D and 3-D SCB *variable sweep optimizations*, follow the complete optimization formulation from Section 5.2. Thus, the formulation once again includes the sweep angle in the design variables and the drag constraint as active design constraint. The goal of these optimizations is to show the potential in weight reductions when considering a single design point, for both 2-D and 3-D SCB designs. Equation 6.2 shows the mathematical definition used for these optimizations.

$$\begin{aligned}
& \text{minimize} && W_M^*(X) \\
& && X = [\Lambda, \alpha, \kappa, W_M^*, W_F^*] \\
& \text{subject to} && C_D \leq C_{D,0} \\
& && C_L = W_D / (q_{cr} \cdot S_{wing}) \\
& && W_M^* = W_M \\
& && W_F^* = W_F
\end{aligned} \tag{6.2}$$

Once the variable sweep optimizations have been performed they will be repeated with a minor adjustment to the formulation: the sweep angle will no longer be considered to be a variable. Instead, the sweep angle will be reduced by a fixed value in order to investigate the effect of reducing the sweep angle by a fixed value as opposed to including it as a design variable. The initial and fixed value for the reduced sweep angle will be the optimized value found in the variable sweep optimizations. This second set of low sweep design optimizations will be referred to as the 2-D and 3-D SCB *fixed sweep optimizations*. The used mathematical definition for the fixed sweep optimizations is shown in Equation 6.3.

$$\begin{aligned}
& \text{minimize} && W_M^*(X) \\
& && X = [\alpha, \kappa, W_M^*, W_F^*] \\
& \text{subject to} && C_D \leq C_{D,0} \\
& && C_L = W_D / (q_{cr} \cdot S_{wing}) \\
& && W_M^* = W_M \\
& && W_F^* = W_F
\end{aligned} \tag{6.3}$$

As can be seen, the wing sweep angle has been removed from the design variables as it is now a fixed value during the optimizations. It has to be noted that, since the wing sweep angle will be drastically reduced compared to the baseline wing, the drag constraint is still required to ensure the resulting design is optimized with respect to the baseline wing.

6.2.3 Multi-point Low Sweep Design Optimization

Ultimately, a multi-point optimization will be performed with the sweep angle, once again, included as a design variable. This seventh and final optimization takes the off-design conditions into consideration by optimizing for three design points spread out evenly over the cruise phase, investigating the potential of the SCB designs when confronted with variations in shock wave position across the design points. Because this optimization considers three times as many design points it also becomes significantly more expensive in terms of computational time. This increase in computational cost is the reason for performing only one multi-point optimization which will consider 3-D SCB designs. The 3-D SCB design is chosen over the 2-D SCB design since these have shown to result in improved off-design performance. [13] [28] [29]

For the multi-point optimization, an extended version of the mathematical definition from Section 5.2 is used in order to incorporate the three design points. For each design point, an angle of attack is added to the design variables as well as a lift constraint and a drag constraint to the design constraints. The final mathematical definition for the multi-point optimization is shown in Equation 6.4.

$$\begin{aligned}
 &\text{minimize} && W_M^*(X) \\
 &&& X = [\Lambda, \alpha_1, \alpha_2, \alpha_3, \kappa, W_M^*, W_F^*] \\
 &\text{subject to} && C_{D_1} \leq C_{D_1,0} \\
 &&& C_{D_2} \leq C_{D_2,0} \\
 &&& C_{D_3} \leq C_{D_3,0} \\
 &&& C_{L_1} = W_{D_1} / (q_{cr} \cdot S_{wing}) \\
 &&& C_{L_2} = W_{D_2} / (q_{cr} \cdot S_{wing}) \\
 &&& C_{L_3} = W_{D_3} / (q_{cr} \cdot S_{wing}) \\
 &&& W_M^* = W_M \\
 &&& W_F^* = W_F
 \end{aligned} \tag{6.4}$$

6.3 Optimization Results

The results from the optimizations discussed in the previous section are shown and interpreted in this section. For each optimization: the convergence results are provided; the initial and optimized designs are compared; the spanwise load distribution and Mach number distributions for the wing are discussed; the shapes of the airfoils and SCBs are shown and interpreted along with the associated pressure distributions; and the lift-to-drag ratios are investigated over a range of lift coefficient values.

The results of the SCB shape optimizations are discussed first in Subsection 6.3.1. Then, the results from the variable and fixed sweep optimizations are discussed in Subsection 6.3.2 and Subsection 6.3.3, respectively. Finally, the results of the multi-point optimization are shown in Subsection 6.3.4.

6.3.1 Shock Control Bump Shape Optimizations

The goal of the SCB shape optimizations is to verify that the geometry parameterization for the 2-D and 3-D SCB designs can be used by the optimizer to achieve a reduction in MTOW. The results of these optimizations are discussed in this section.

Convergence Results

The convergence results for the 2-D and 3-D SCB shape optimizations are listed in Table 6.5 and Table 6.6, respectively. For both optimizations, the stopping criteria was the tolerance on the objective function. This tolerance is a lower bound on the change in the value of the objective function during an iteration. The reduction in objective function is roughly 1.1% for both optimizations.

The ratio between the number of evaluations and iterations is relatively high for these optimizations, nearly 90% of all proposed design steps were accepted by the optimizer. This can be interpreted as an indication of efficacy for the optimization setup.

Table 6.5: Convergence results for the 2-D SCB shape optimization.

Parameter	Value
Objective function value	0.98872
Number of evaluations	31
Number of iterations	27
Maximum constraint violation	3.29E-5

Table 6.6: Convergence results for the 3-D SCBs shape optimization.

Parameter	Value
Objective function value	0.98938
Number of evaluations	25
Number of iterations	23
Maximum constraint violation	-4.05E-5

The maximum constraint violation for the 2-D SCB shape optimization applied to the lift constraint and the maximum violation for the 3-D SCB shape optimization was on the surrogate MTOW constraint. Since the maximum constraint violations are well within acceptable limits, all other constraints are also satisfied to a similar, or even higher, degree.

Initial & Optimized Designs

The main characteristics of the initial and both optimized designs are compared in Table 6.7. From this table, it can be seen that the optimized designs have an improved lift-to-drag ratio compared to the initial design. This higher ratio results in a fuel weight reduction which directly reduces the MTOW as well. Ultimately, the wing weight is also reduced due to the snowball-effect.

Table 6.7: Characteristics of the initial and optimized designs from the SCB shape optimizations.

Design	α [°]	Λ_{LE} [°]	W_M [N]	W_F [N]	W_W [N]	W_D [N]	C_L [-]	C_D [-]	L/D [-]
Initial	0.8655	32.85	720 789	175 949	80 987	622 929	0.54317	0.032197	16.870
Optimized 2-D	0.6485	32.85	712 658	168 559	80 304	618 792	0.53958	0.030496	17.693
Optimized 3-D	0.6834	32.85	713 134	168 964	80 346	619 049	0.53977	0.030587	17.647

Although the optimized designs show very similar characteristics, the 2-D SCB design does outperforms the 3-D SCB design by a small margin.

Spanwise Load Distribution

The spanwise load distributions for the designs are shown in Figure 6.9. From this figure, it can be seen that the load distributions are nearly identical. The baseline wing has a slightly increased loading near the root and tip areas, near the kink area the 2-D and 3-D SCB designs have a marginally higher loading. Because the distributions are similar, no drastic differences in terms of induced drag contribution are to be expected between these designs.

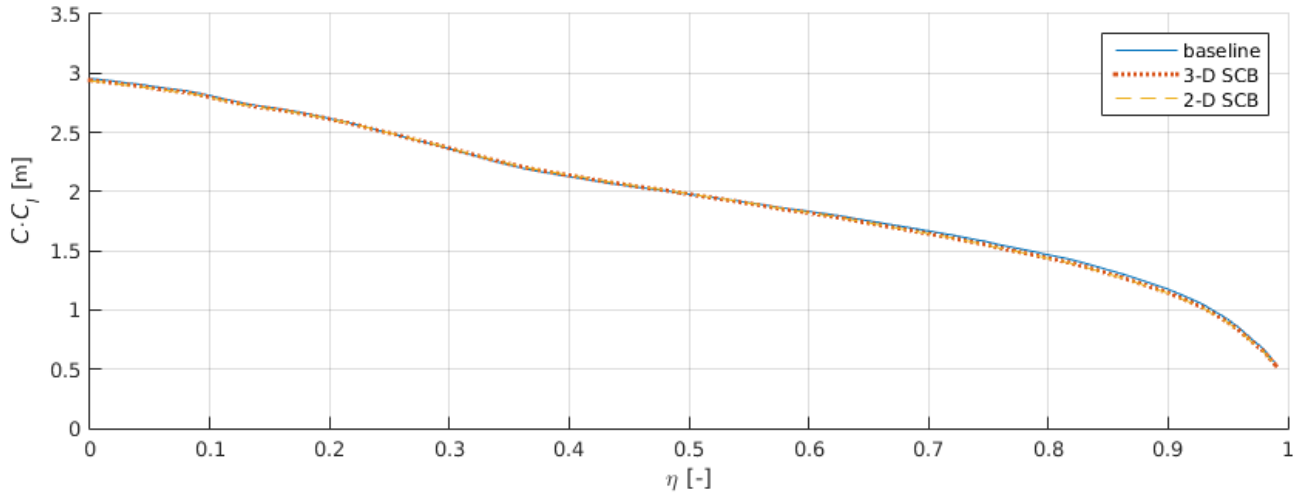


Figure 6.9: Load distribution for the baseline, 2-D SCB, and 3-D SCB wings from the SCB shape optimizations.

Mach number Distribution

A top view of the Mach number distribution on the upper surface of the wing is shown in Figure 6.10 for the baseline wing, 2-D SCB wing, and 3-D SCB wing at the corresponding lift coefficients from Table 6.7. Clearly, both 2-D and 3-D SCB designs reduce the local Mach number at the original shock wave position, especially near the root of the wing. Further outboard there are signs of flow re-acceleration which is causing secondary shock structures. This effect is concentrated near the kink area of the wing. Moving passed the kink, further towards the tip, there are no signs of secondary shock structures in the 2-D SCB design, for the 3-D SCBs design a larger extend of flow re-accelerations is present.

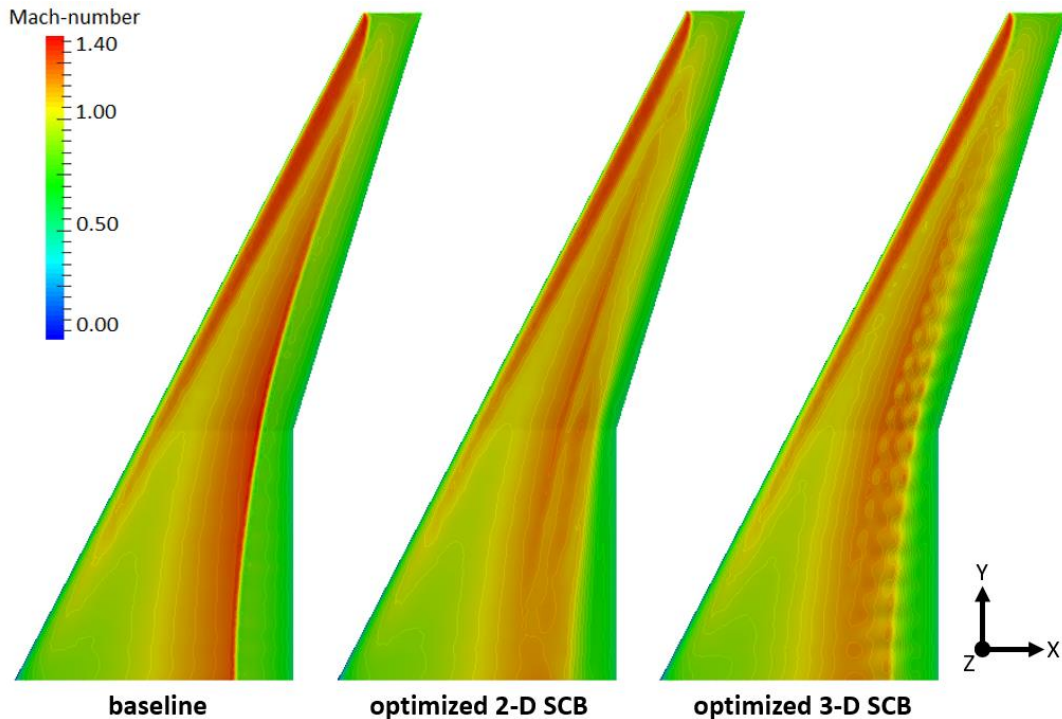


Figure 6.10: Mach-distributions of the initial and optimized designs from the SCB shape optimizations.

Airfoil Shapes & Pressure Distributions

Figure 6.13 shows the airfoil shapes at four spanwise sections along with their associated pressure distributions at the design point conditions, a detailed view of the SCB shapes is also included. Do note the

difference in axes limits used for the detailed view of the SCB shapes. The spanwise sections are chosen such that they occur at the crest - the highest point - of the 3-D SCBs.

From the detailed SCB shape views it can be seen that the 3-D SCB crests are significantly higher at every section than for the 2-D SCB. Additionally, the crests of the 3-D SCBs are also positioned further forward than those for the 2-D SCB. As far as the start and end points are considered they appear to coincide at each section for both bump designs.

Although difficult to observe, careful inspection at the $\eta = 0.31$ section shows a small concave area interrupting the smooth bump design, more visibly for the 3-D SCB than the 2-D SCB design. It seems the optimizer has placed smaller bumps at the ramp of the main bump. This occurrence of a double bump is likely to be the cause of the flow re-acceleration that is occurring in the kink region.

The pressure coefficient distributions are, overall, typical for SCB designs: an increase in aft loading by reducing and delaying the pressure peak, resulting in a decrease in wave drag while maintaining a similar lift coefficient. At the $\eta = 0.31$ and $\eta = 0.56$ sections the flow re-acceleration observed in Figure 6.10 is also visible through the occurrence of multiple pressure peaks across the SCB length.

Lift-to-Drag Ratio

The performance of the initial and optimized designs is shown in Figure 6.11 by plotting the lift-to-drag ratio over a range of lift coefficients. To highlight the differences in performance near the design point, a detailed view of the performance near the design point is given in Figure 6.12.

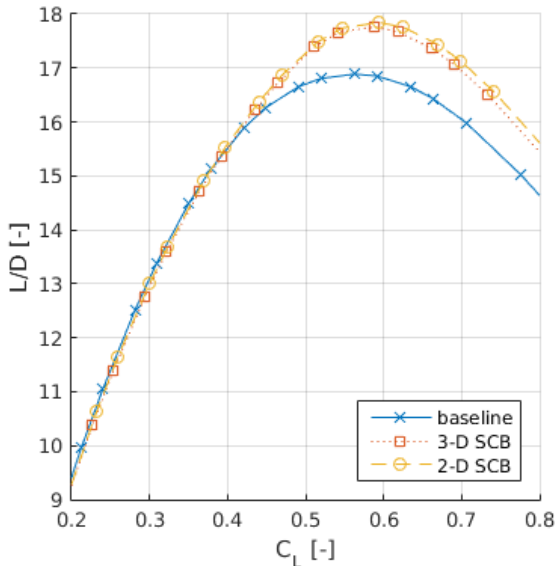


Figure 6.11: Performance of the initial and optimized designs from the SCB shape optimizations.

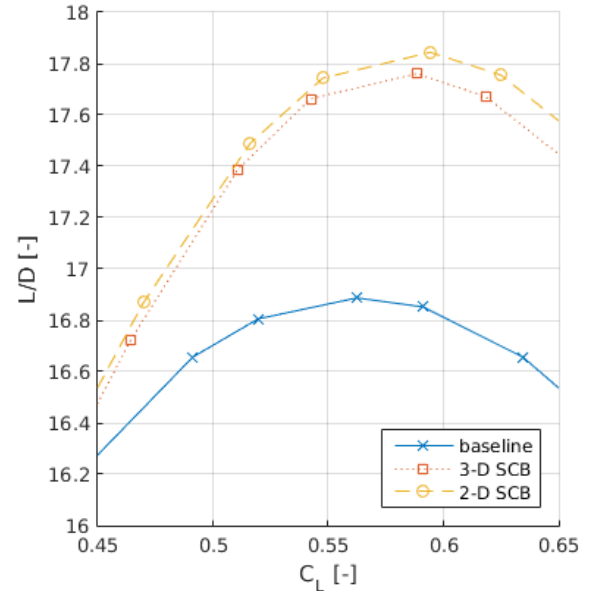


Figure 6.12: Performance near the design lift coefficient of the initial and optimized designs from the SCB shape optimizations.

When comparing the performance of the optimized designs with that of the baseline design, they show similar characteristics for lift coefficient values up to 0.4. Beyond this point, the optimized designs start to show improved ratios compared to the baseline, reaching a peak in difference near the lift coefficient value of 0.58. Beyond the peak the difference in ratios remains almost constant. Interestingly, the highest lift-to-drag ratios for the optimized designs occur at a lift coefficient that is larger than the design lift coefficient.

Lastly, when looking at the optimized 2-D and 3-D SCB designs separately, it is clear that the wing with the 2-D SCB has a higher lift-to-drag ratio than the wing with 3-D SCBs, across the entire range of lift coefficients.

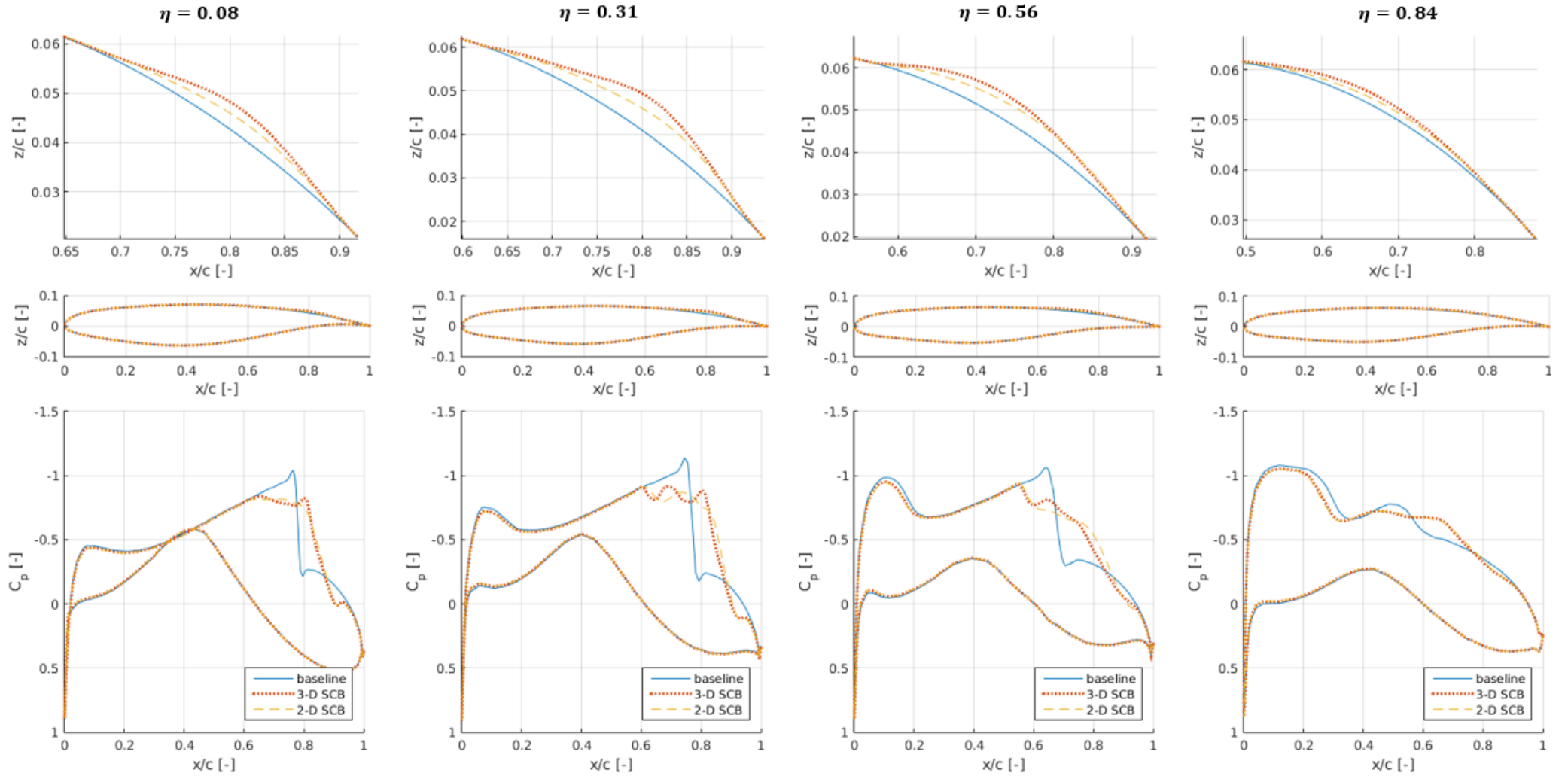


Figure 6.13: Pressure distributions (bottom), airfoil shapes (middle), and SCB shapes (top) for the baseline, 3-D SCBs, and 2-D SCB wings, from the SCB shape optimizations at four spanwise sections.

6.3.2 Variable Sweep Optimizations

The results of the 2-D and 3-D SCB variable sweep optimizations are discussed in this subsection. The goal of these optimizations is to show how much weight reduction can be achieved by implementing SCB to facilitate low sweep wing design while considering a single design point. The performance of the variable sweep designs are discussed the next subsection, together with the performance of the fixed sweep designs.

Convergence Results

The convergence results for the 2-D and 3-D SCB variable sweep optimizations are listed in Table 6.8 and Table 6.9, respectively. For both sweep optimizations, the stopping criteria was the tolerance on the objective function and reductions in objective function of over 3.1% were achieved.

Table 6.8: Convergence results for the 2-D SCB variable sweep optimization.

Parameter	Value
Objective function value	0.96849
Number of evaluations	60
Number of iterations	40
Maximum constraint violation	2.62E-5

Table 6.9: Convergence results for the 3-D SCBs variable sweep optimization.

Parameter	Value
Objective function value	0.96869
Number of evaluations	68
Number of iterations	60
Maximum constraint violation	-1.05E-5

For the 3-D SCB design the ratio between evaluations and iterations is similar to those mentioned in the previous section. However, for the 2-D SCB design there is a large drop in efficacy to 66%, where the only difference is the addition of the sweep design variable and drag constraint to the problem formulation. Interestingly, the number of evaluations between both optimizations are still relatively similar.

For the 2-D SCB sweep optimization the maximum constraint violation was found to apply to the lift constraint. For the 3-D SCB sweep optimization the maximum constraint violation applied to the surrogate fuel weight constraint. The values are, once again, well within acceptable limits and thus the same is true for all other design and consistency constraints.

Optimization Results

A comparison of the characteristics associated with the baseline wing and both optimized 2-D and 3-D SCB wings is listed in Table 6.10. The most noteworthy difference between the initial and optimized designs is the change in sweep angle, both optimized designs have no leading-edge sweep. This reduction in wing sweep is the main cause for the large weight reduction in wing structural weight, which in turn is the leading component in the MTOW reduction.

Table 6.10: Characteristics of the initial and optimized designs from the variable sweep optimizations.

Design	α [°]	Λ_{LE} [°]	W_M [N]	W_F [N]	W_W [N]	W_D [N]	C_L [-]	C_D [-]	L/D [-]
Initial	0.8655	32.85	720 789	175 949	80 987	622 929	0.54317	0.032197	16.870
Optimized 2-D	0.8914	0.00	698 074	172 321	61 901	602 270	0.52517	0.031658	16.589
Optimized 3-D	0.8988	0.00	698 222	172 459	61 910	602 342	0.52521	0.031689	16.574

In contrast with the SCB shape optimizations, the lift-to-drag ratios for the optimized designs has actually decreased, slightly. Yet, even though the aerodynamic efficiency has dropped, the fuel weight is still reduced compared to the baseline design due to the effect the reduced wing weight has on the MTOW, i.e. due to the large MTOW reduction and its snowball-effect on the fuel weight.

Spanwise Load Distribution

The load distributions for the designs are shown in Figure 6.14. In this figure the load distribution associated with the baseline, straight, 2-D SCB, and 3-D SCB wings are compared. Here, the straight wing is the wing with the optimized sweep angle but without SCBs. Between the straight, 2-D SCB, and 3-D SCB wings only minor differences can be observed: between the three, the inboard loading is higher for the wings with SCB and the outboard loading is lower.

However, comparing the designs with the reduced sweep angle with the baseline wing, a larger difference is clearly visible. The baseline wing has a higher loading in general, especially near the tip; the only location where the baseline has a lower loading is near the root of the wing.

Hence, among the straight, 2-D SCB, and 3-D SCB wings the contribution to the drag from the induced and wave drag components are, more or less, equal. Compared to the baseline wing the three straight leading edge wings are expected to show an increase in induced drag contribution due to the decrease in ellipticity of the lift distribution.

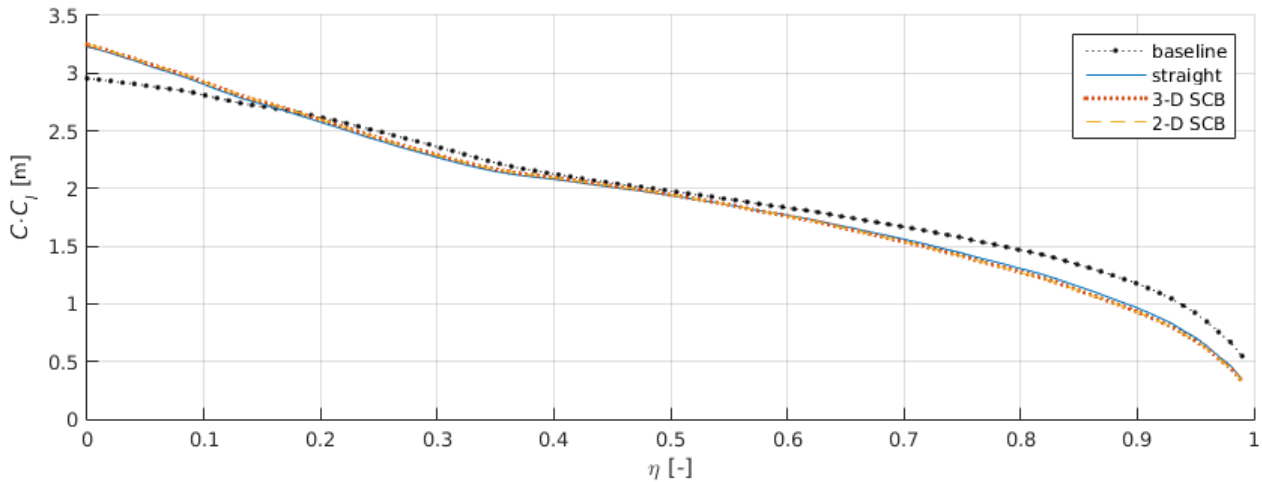


Figure 6.14: Load distribution for the baseline, straight, 2-D SCB, and 3-D SCB wings from the variable sweep optimizations.

Pressure Coefficient Distribution

Figure 6.15 shows the airfoil shapes at four spanwise sections along with their associated pressure distributions at the design point conditions, a detailed view of the SCB shapes is also included. Do take into account the difference in axes limits used for the detailed view of the SCB shapes.

In agreement with the results from the SCB shape optimizations, the detailed SCB shape shows that the 3-D SCB crests are significantly higher than for the 2-D SCB at every section and the crests of the 3-D SCBs are also positioned further forward than those for the 2-D SCB. The start and end points are, again, identical for both bump designs.

Lastly, the earlier observed double bump occurrence is visible at the first three spanwise sections, namely $\eta = 0.08$, $\eta = 0.31$, and $\eta = 0.56$. These occurrences of double bumps are likely generated due to the misposition of the main SCB. Because the main SCB is lagging behind in position it is causing unwanted secondary shock structures. The optimizer identifies these secondary shock structures as areas suitable for SCB designs and adds the secondary bump to further reduce the wave drag.

Mach number Distribution

The Mach number distributions for the straight, 3-D SCB, and 2-D SCB designs are shown in Figure 6.16 at the design lift coefficient listed in Table 6.10. Here, the straight wing, i.e. the wing without SCB, is shown at the same lift coefficient. Similar to the distributions shown for the optimizations of the previous section, the difference in Mach number near the original shock wave position is clearly visible for the wings with SCB.

However, for the inboard area the position of the resulting SCB designs does not appear to match the shock wave position of the wing without SCB, as is evident in distribution of the 3-D SCB wing. The inboard area is also the area where the shock wave position has moved along the wing surface the most between the baseline wing, which was shown earlier in Figure 6.10, and the wing without SCB, shown here. It appears that the SCB position is lagging behind due to the earlier experienced shock wave positions when the sweep angle was larger, i.e. due to the sweep angle acting as a design variable in the optimization process.

Similar to the distributions shown in the previous section, there are some occurrence of flow re-acceleration but the flow re-accelerations visible in this figure are more irregular for the optimized designs.

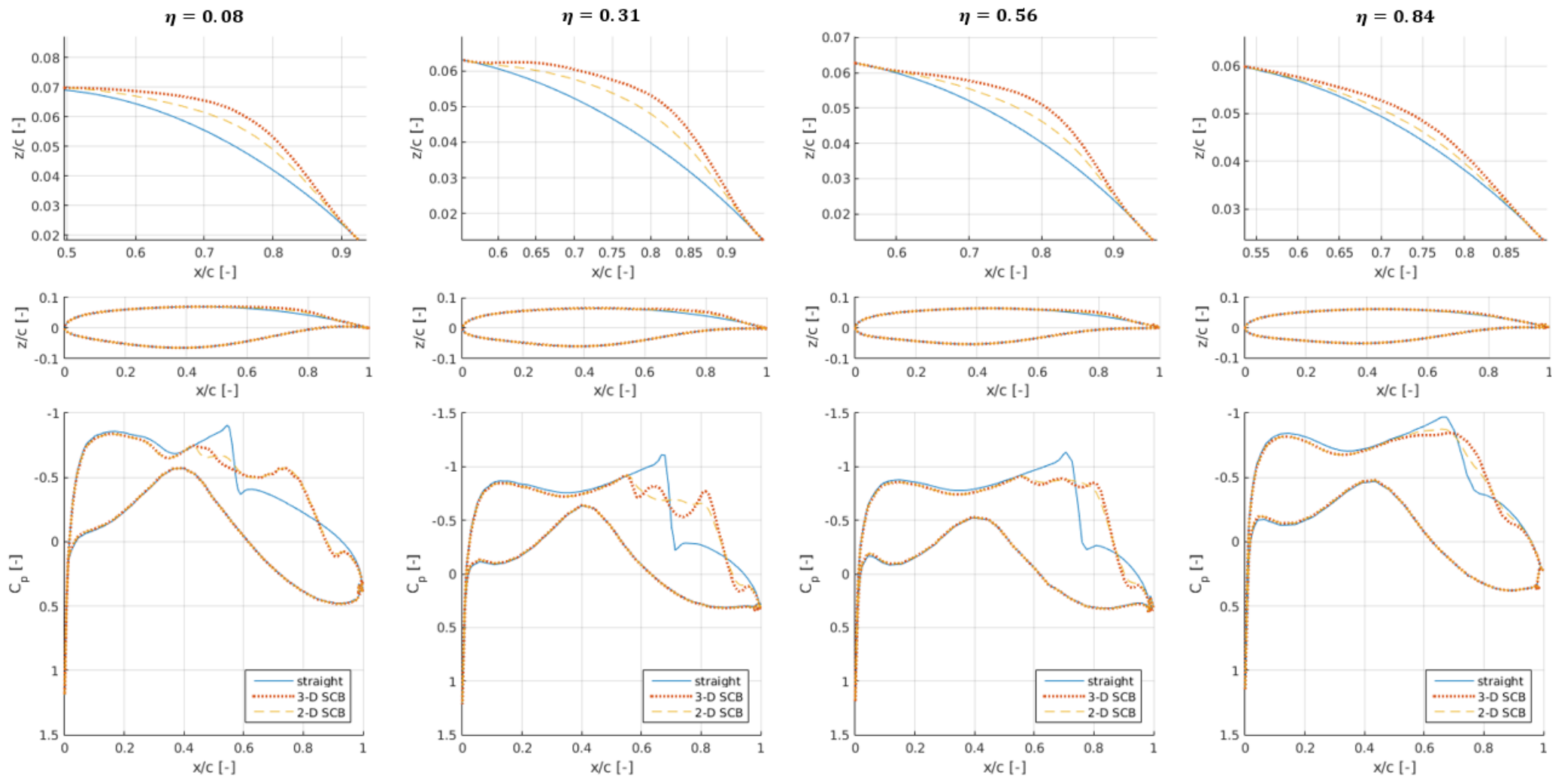


Figure 6.15: Pressure distributions (bottom), airfoil shapes (middle), and SCB shapes (top) for the straight, 3-D SCBs, and 2-D SCB wings from the variable sweep optimization at four spanwise sections.

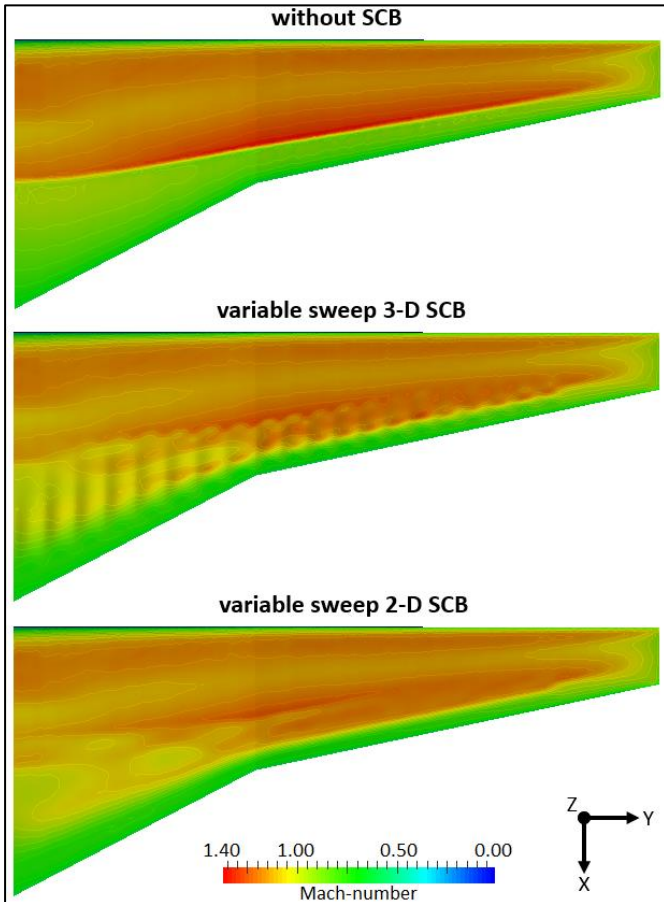


Figure 6.16: Mach-distributions of the variable sweep wings.

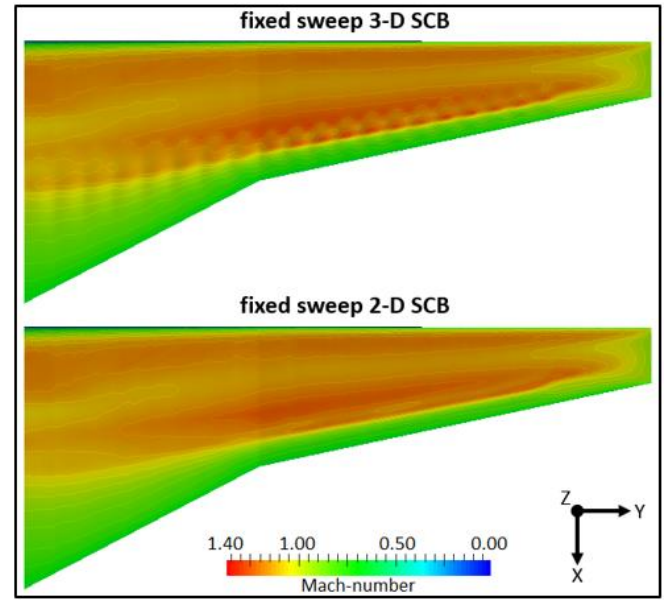


Figure 6.17: Mach distributions of the fixed sweep wings.

6.3.3 Fixed Sweep Optimizations

The results of the 2-D and 3-D SCB fixed sweep optimizations are discussed in this subsection. The aim of these optimizations is to investigate the influence of excluding the sweep angle as a variable and using a fixed sweep angle reduction. Here, the sweep angle is reduced by the same amount as the optimized results from the variable sweep optimizations.

Convergence Results

The convergence results for the 2-D and 3-D SCB fixed sweep optimizations are listed in Table 6.11 and Table 6.12, respectively. For both optimizations, the stopping criteria was the value of the objective function, i.e. when equal or smaller than the obtained objective values by the variable sweep optimizations the stopping criteria will be met.

Table 6.11: Convergence results for the 2-D SCB fixed sweep optimization.

Parameter	Value
Objective function value	0.96852
Number of evaluations	15
Number of iterations	15
Maximum constraint violation	1.43E-4

Table 6.12: Convergence results for the 3-D SCB fixed sweep optimization.

Parameter	Value
Objective function value	0.96853
Number of evaluations	29
Number of iterations	28
Maximum constraint violation	-1.67E-5

For both optimizations, the ratio between evaluations and iterations is even higher than for the SCB shape optimizations; only a single evaluation was not accepted, for the 3-D SCB fixed sweep optimization to be specific. The total number of evaluations required to reach a similar optimum are, however, very different. The 3-D SCB variant required almost twice as many evaluations and iterations as the 2-D SCB setup.

For the 2-D SCB sweep optimization the maximum constraint violation was found to apply to the lift constraint. For the 3-D SCB sweep optimization the maximum constraint violation applied to the surrogate fuel weight constraint. The maximum constraint values are, yet again, well within acceptable limits, thus all other design and consistency constraints are also satisfied.

Optimization Results

The characteristics associated with both optimized 2-D SCB and 3-D SCB fixed sweep designs are listed in Table 6.13, along with the characteristics from the variable sweep designs. Comparing the results with the optimized designs from the variable sweep optimizations they appear to be almost identical. The only notable difference is the lift-to-drag ratio for the 3-D SCB optimized design which is slightly higher for the fixed sweep design compared to the variable sweep design. The fixed sweep optimizations also resulted in a higher angle of attack in order to maintain steady horizontal flight.

Table 6.13: Characteristics of the optimized designs from the variable and fixed sweep optimizations.

Design	α [°]	Λ_{LE} [°]	W_M [N]	W_F [N]	W_W [N]	W_D [N]	C_L [-]	C_D [-]	L/D [-]
Variable 2-D	0.8914	0.00	698 074	172 321	61 901	602 270	0.52517	0.031658	16.589
Variable 3-D	0.8988	0.00	698 222	172 459	61 910	602 342	0.52521	0.031689	16.574
Fixed 2-D	0.9342	0.00	698 098	172 343	61 918	602 380	0.52525	0.031662	16.589
Fixed 3-D	0.9349	0.00	698 106	172 350	61 905	602 269	0.52516	0.031665	16.585

Mach number Distribution

The Mach number distributions for the straight, 3-D SCB, and 2-D SCB fixed sweep designs are shown in Figure 6.17 alongside the Mach number distributions of the variable sweep designs. The difference between the variable and fixed sweep optimizations is immediately clear: for the fixed sweep optimizations, the bumps are positioned near the location of the original shockwave position of the straight wing without SCB. The distributions from the optimized designs also show reduced amounts of flow re-acceleration at the inboard half of the wings compared to the variable sweep Mach number distributions. Though, it has to be noted that the outboard half of the wing shows an increase in the amount of flow re-acceleration.

Pressure Coefficient Distribution

Figure 6.18 shows the airfoil shapes at four spanwise sections along with their associated pressure distributions at the design point conditions, a detailed view of the SCB shapes is also included. Do observe the difference in axes limits used for the detailed view of the SCB shapes.

Comparing the detailed SCB shapes with those from the variable sweep designs (Figure 6.15) several observations can be made: the length of the bump is shorter; the crests are positioned further forward; the crest height is roughly identical; the overall height of the bump has been reduced; and, lastly, there are no double bump designs.

The pressure distributions tell the same story. They no longer show the multiple pressure peaks associated with the flow re-accelerations yet still show the typical SCB characteristics. Namely, a delayed and reduced pressure peak which increases the aft loading of the section, maintaining the original lift coefficient while reducing the wave drag.

Lift-to-Drag Ratio

The performance of the initial and optimized designs is shown in Figure 6.19 by plotting the lift-to-drag ratio over a range of lift coefficients. In order to compare the results of the variable and fixed sweep optimizations, all relevant designs from these optimizations are included. Additionally, because the performances of the various optimized designs are similar, a more detailed view of the performance of the designs near the design lift coefficient is given in Figure 6.20.

When comparing the performance of the optimized designs with that of the baseline it becomes clear that the baseline wing has improved performance across the entire range of lift coefficients. At high and low lift coefficient values this difference in performance is most notably, near the design lift coefficient value the performance of the optimized designs approach that of the baseline wing. Interestingly, the performances of

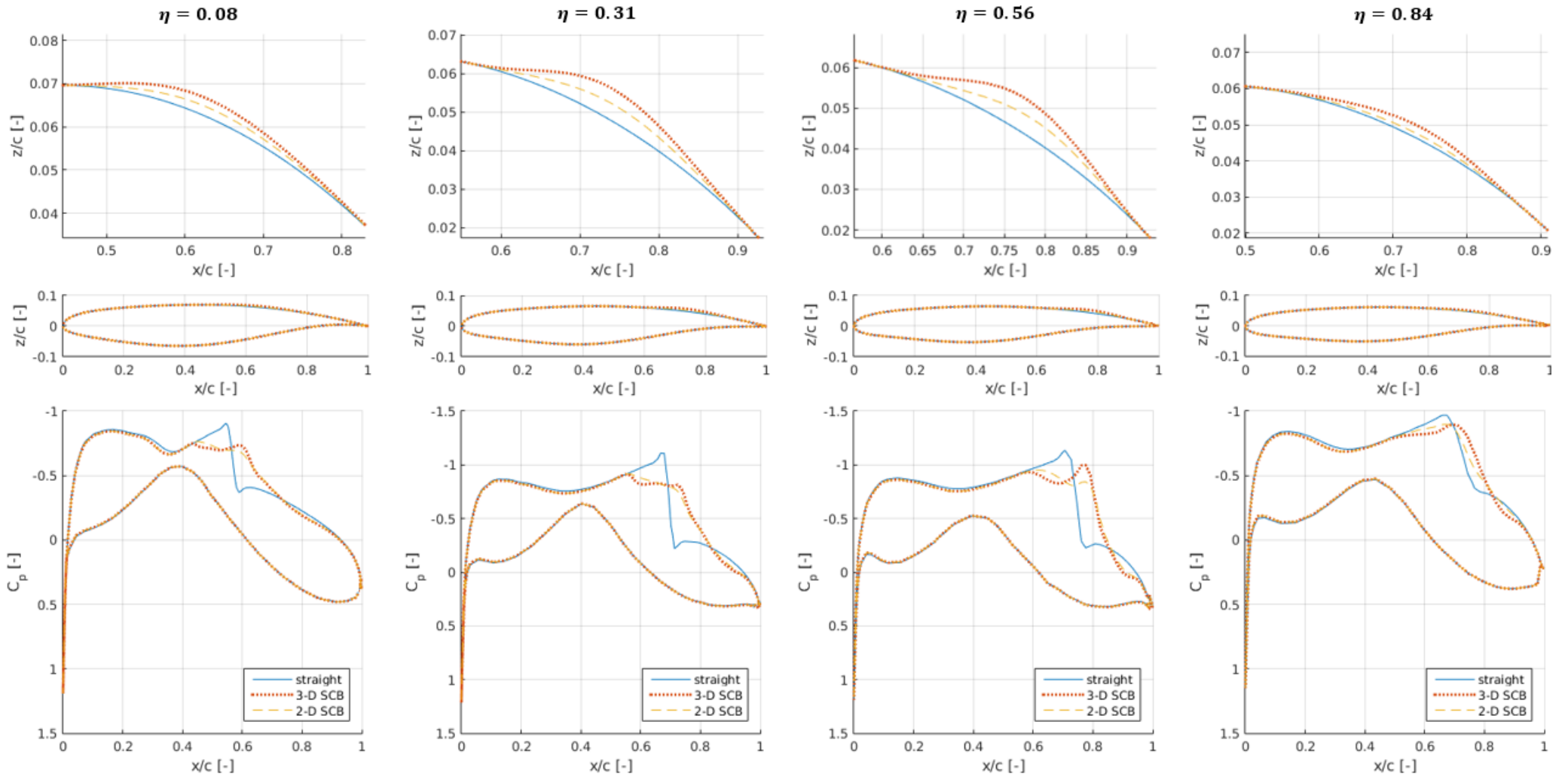


Figure 6.18: Pressure distributions (bottom), airfoil shapes (middle), and SCB shapes (top) for the straight, 3-D SCBs, and 2-D SCB wings from the fixed sweep optimization at four spanwise sections.

both fixed and variable sweep designs experience the maximum lift-to-drag ratio at a higher lift coefficient than the design lift coefficient.

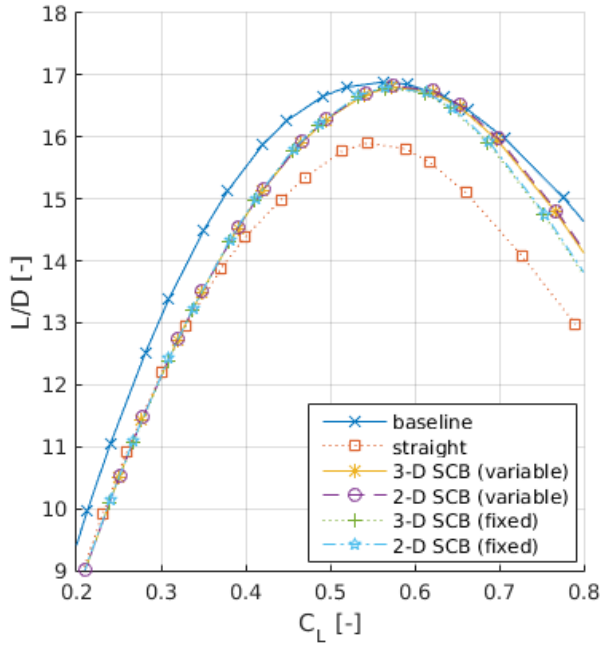


Figure 6.19: Performance of the various designs related to the sweep optimizations.

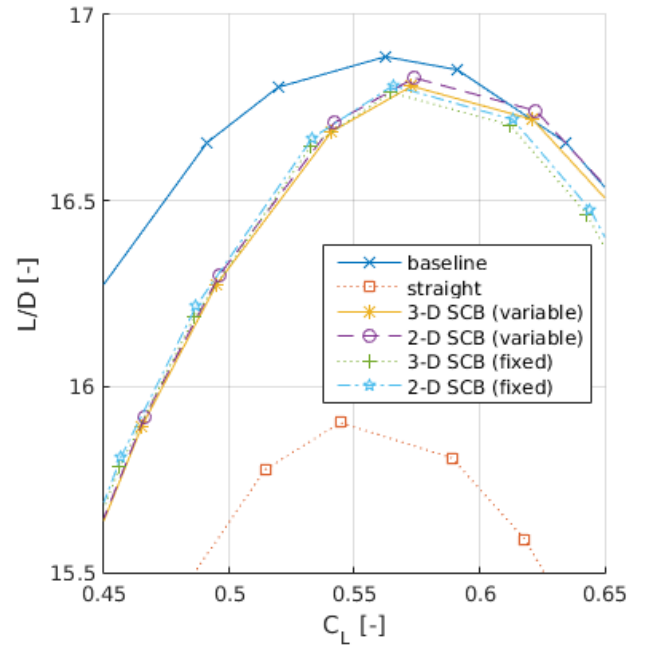


Figure 6.20: Performance near the design lift coefficient of the various designs related to the sweep optimizations.

Comparison between the variable and fixed sweep designs shows that both have similar performance up to a lift coefficient value of 0.575, beyond this point the optimized designs from the variable sweep optimization produce higher lift-to-drag ratios with increasing lift coefficient compared to the fixed sweep optimized designs. For both variable and fixed sweep optimizations, the 2-D SCB variant shows slightly higher lift-to-drag ratios than the 3-D SCB variant.

Lastly, from these figures it can be seen that comparing the straight wing with the optimized designs shows similar results as the comparison made during the discussion of the performance of the SCB shape optimization designs in Subsection 6.3.1. The wings with SCBs show similar performance to that of the straight wing up to a lift coefficient of 0.35. Beyond this point they show improved performance, reaching a peak in increased performance near the design lift coefficient.

6.3.4 Multi-Point Low Sweep Design Optimization

The outcome of the multi-point optimization is discussed in this section. The aim of this optimization is to investigate the effect of considering three design points, spread out evenly across the cruise phase in terms of flight range, instead of only a single point. Because of the extensive computational cost of this optimization, only one optimization is performed using the 3-D SCB setup with a maximum number of 60 iterations as added stopping criteria.

Convergence Results

The convergence results for the multi-point optimization is listed in Table 6.14. The stopping criteria for this optimization was the maximum number of evaluations, which was specifically set for this optimization due to its increased computational cost, and the objective function was reduced by 1.24% at this point.

Table 6.14: Convergence results for the multi-point optimization.

Parameter	Value
Objective function value	0.98760
Number of evaluations	60
Number of iterations	17
Maximum constraint violation	2.23E-4

The ratio between evaluations and iterations is very poor for the multi-point optimization. With a reduction in efficacy to 28.3%, nearly three quarters of all evaluations were not accepted by the optimizer as reasonable steps.

The maximum constraint violation of this optimization applied to the lift constraint at the first design point. Naturally, all other constraints were also satisfied to the same, or an even higher, degree.

Optimization Results

The characteristics of the baseline and optimized multi-point designs are compared in Table 6.15. The wing sweep has been reduced by more than 11° which resulted in the structural wing weight reduction of 10.2%. This wing weight reduction is the largest component of the 1.24% MTOW reduction. The fuel weight has also been reduced, but from the lift-to-drag ratios it can be determined that this is purely due to the snowball-effect that the MTOW has on the fuel weight since the aerodynamic efficiency has actually decreased for the optimized design.

Table 6.15: Characteristics of the initial and optimized design from the multi-point optimization.

Parameter	Initial	Optimized	Unit
Λ_{LE}	32.85	21.71	[$^\circ$]
W_M	720 789	711 856	[N]
W_F	175 961	175 248	[N]
W_W	80 987	72 713	[N]
α_1	1.1283	0.8263	[$^\circ$]
α_2	0.8655	0.5731	[$^\circ$]
α_3	0.6179	0.3373	[$^\circ$]
W_{D_1}	666 141	657 641	[N]
W_{D_2}	622 928	614 491	[N]
W_{D_3}	582 514	574 102	[N]
C_{L_1}	0.58085	0.57331	[-]
C_{L_2}	0.54317	0.53569	[-]
C_{L_3}	0.50793	0.50049	[-]
C_{D_1}	0.03442	0.03435	[-]
C_{D_2}	0.03220	0.03216	[-]
C_{D_3}	0.03032	0.03031	[-]
$(L/D)_1$	16.875	16.690	[-]
$(L/D)_2$	16.870	16.657	[-]
$(L/D)_3$	16.752	16.512	[-]

Mach number Distributions

The Mach number distributions for the reduced sweep wing without SCB at the first design point and the optimized wing at all three design points are shown in Figure 6.21. The presence of the optimized 3-D SCBs still lowers the local Mach number near the original location of the shockwave, albeit to a lesser extent than observed in the four single-point sweep optimizations. There is no sign of any unfavourable flow re-accelerations at any of the design points.

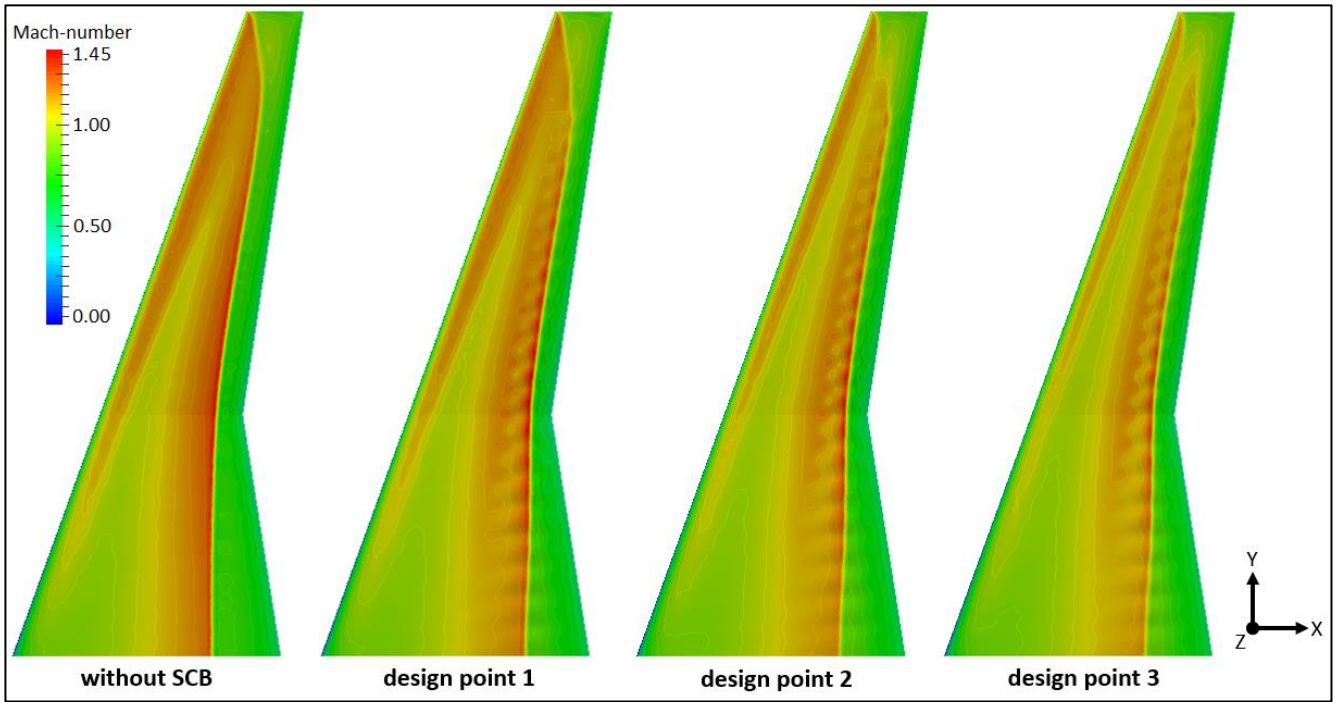


Figure 6.21: Mach distributions of the optimized multi-point wing, with and without SCBs.

By comparing the variation of the shock wave location between the baseline (Figure 6.10) and optimized wing without SCB it can easily be said that the variation in location is only minimal, especially when comparing the shift in position between the straight and baseline wings from the single-point sweep optimizations. Hence, the issue which was observed for the single-point variable sweep optimizations, the SCB lagging behind with the new shock wave locations, does not seem to be applicable to the optimized multi-point design.

Lift-to-Drag Ratio

The performance of the initial and optimized designs from the multi-point optimization is shown and compared in Figure 6.22 by plotting the lift-to-drag ratio over a range of lift coefficients. A detailed view of the performance near the design points of the multi-point optimization is given in Figure 6.23.

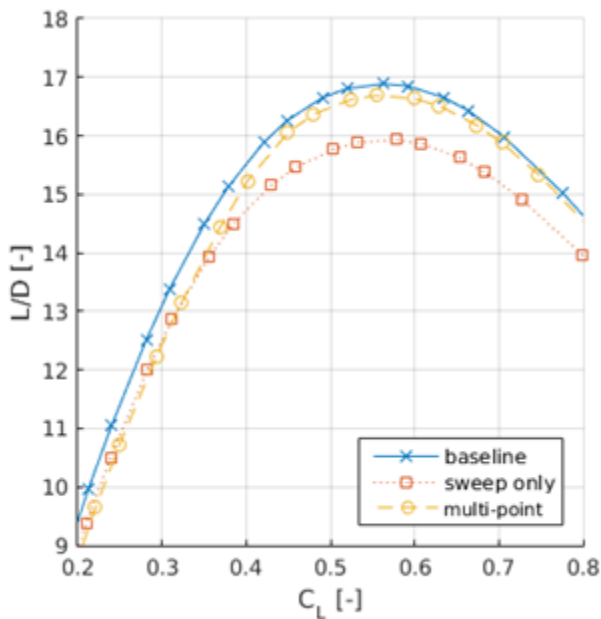


Figure 6.22: Performance of the initial and optimized designs from the multi-point optimizations.

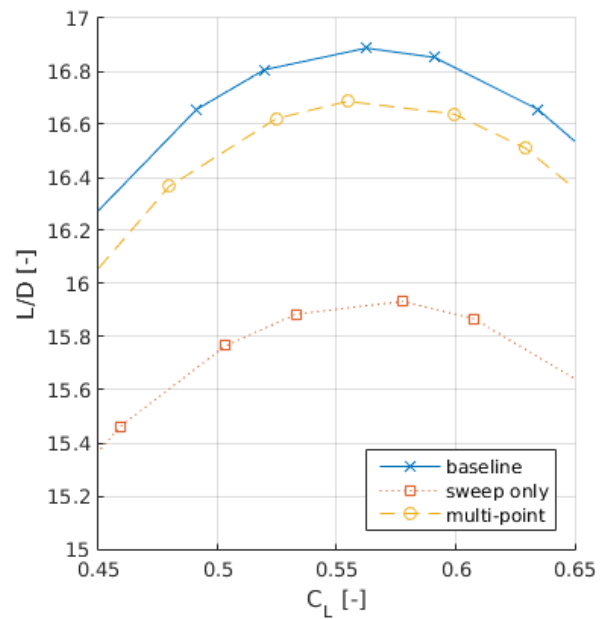


Figure 6.23: Performance near the design lift coefficients of the initial and optimized designs from the multi-point optimizations.

These figures show similar behaviour as the results from previously discussed optimizations: compared to the wing without SCB the optimized wing shows identical performance up to the lift coefficient value of 0.35, beyond this point the optimized wing has improved performance; and compared to the baseline wing the optimized wing generates a lower lift-to-drag ratio across the whole range of lift coefficients.

However, the previously discussed designs all experienced their peak ratio at a higher lift coefficient than the design point, yet the multi-point design experiences its peak in performance well within the range of design lift coefficients. The performance at the lower values for the lift coefficient is also closer to that of the baseline than for the other optimized designs.

Pressure Coefficient Distributions

Figure 6.24 shows the airfoil and detailed SCB shapes for the initial and optimized designs. In Figure 6.25 the pressure distributions for the wing without SCB and the optimized wing are shown, the distribution for the wing without SCB is shown for the first design point and the distributions for the optimized wing are shown for all three points.

From the detailed SCB shape in Figure 6.24 it can be seen that the SCB shapes are similar to those found from the fixed sweep optimization. Both the length and height of the bump are similar, but the crests of the bumps are positioned slightly more aft.

The pressure distributions shown in Figure 6.25 once again show the, now familiar, characteristics of the SCB implementation. For these distributions, the presence of the SCB is, however, less pronounced than for the other optimizations. The increase in aft loading and the reduction in pressure peak are less when compared to the results from any of the single-point optimizations.

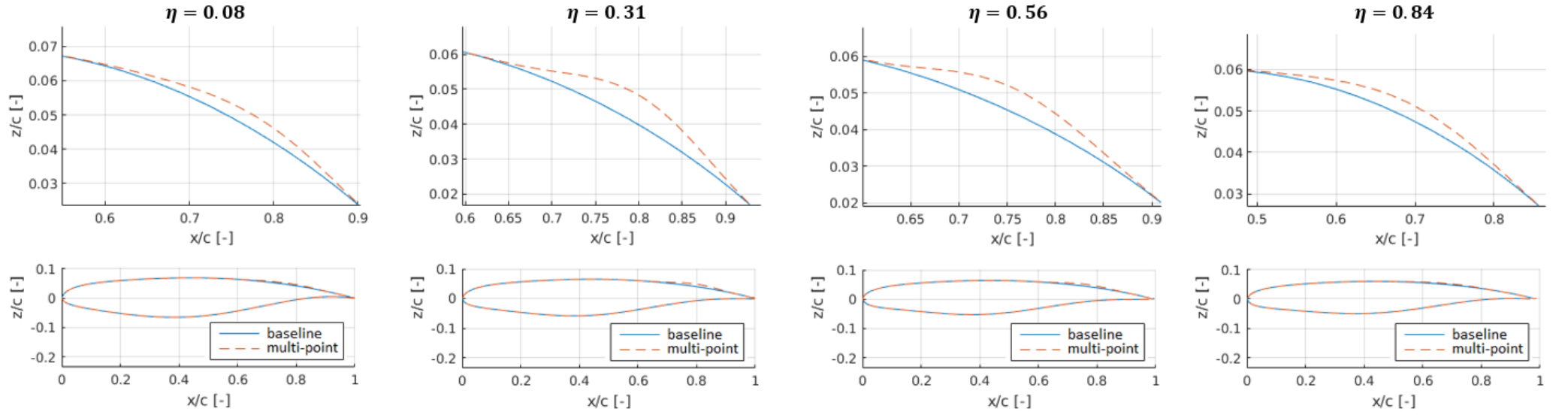


Figure 6.24: Airfoil (bottom) and SCB (top) shapes for the initial and optimized designs from the multi-point optimization.

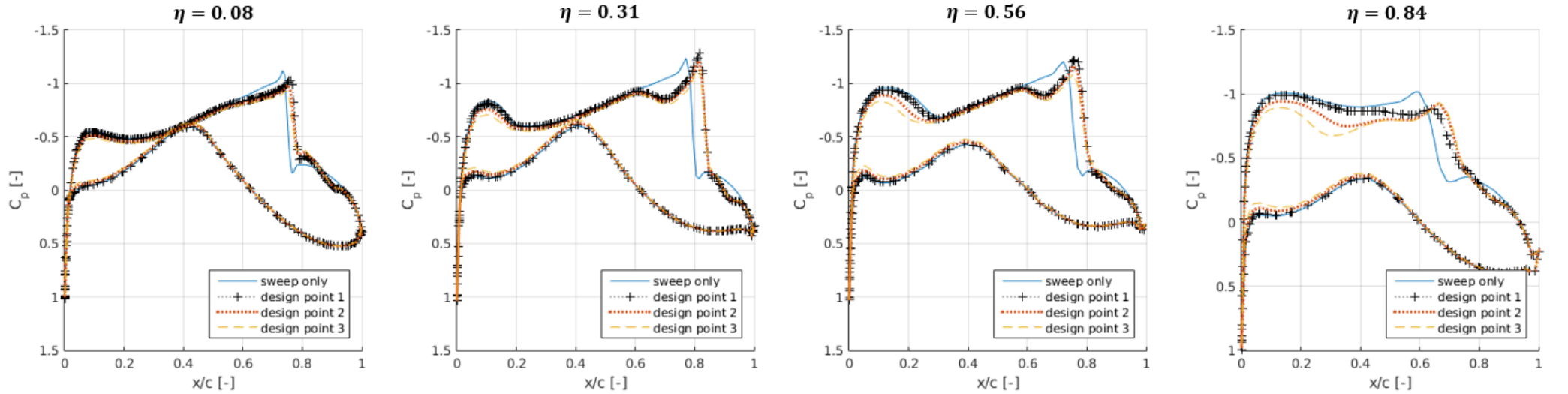


Figure 6.25: Pressure distributions for the sweep only wing, and the optimized wing at the three design points, for four spanwise sections.

Conclusions and Recommendations

This chapter discusses the conclusions and recommendations that can be made based on the results from the previous chapter.

7.1 Conclusions

The conclusions that can be drawn from the results of this research will first be discussed per set of optimizations that were performed. Once all the optimizations have been covered, the overlapping conclusions will be mentioned.

For the optimization only considering the SCB shape variables, i.e. excluding the wing sweep design variable, a reduction of fuel weight by 4.2% was achieved. This reduction can be attributed to the increase in lift-to-drag ratio by 4.9%. Because the MDO considers interdisciplinary effects, the wing weight was also slightly reduced, by 0.84% to be specific. Ultimately, a MTOW reduction of 1.2% was achieved by purely optimizing for aerodynamic performance. Although higher improvements in lift-to-drag ratios have been reported in literature, the improvement achieved with this optimization is significant and the parameterization of the SCB shape can be concluded to function as intended. In contrast to literature, the 2-D SCB design outperformed the 3-D SCB design by a small margin.

The goal of the single-point sweep optimizations, both variable and fixed, was to determine how much MTOW reduction is possibly by converting the lee-way in wave drag, generated via the improved lift-to-drag ratio as shown from the SCB shape optimization, into additional structural wing weight reductions by lowering the wing sweep angle. Ultimately, reductions in the order of 3.1% reduction in MTOW were achieved. This reduction in MTOW consists predominantly of savings in structural wing weight, the aerodynamic efficiency actually decreased compared to the reference design. A 2% fuel weight reduction was achieved, which is less than the fuel weight reduction found for the SCB shape optimizations.

The results from the fixed sweep optimization show that including the sweep angle as a design variable may have detrimental effects on the optimization process. The first indication is the difference in efficacy between the variable and fixed sweep optimizations. Whereas the fixed sweep optimizations have a more uniform success rate ranging from 85 to 100% for evaluations, the single-point variable sweep optimization shows a larger variation in success rate; ranging from 34 to 90% (for the multi-point optimization the success rate dropped even lower, to 28%). The second indication is the position of the SCBs with respect to the original shock wave position for the wing design without SCBs present. When the sweep angle is included as a design variable the optimizer seems to struggle with moving the SCB in chord wise direction, i.e. they are lagging behind at the older shock wave positions from wing designs with higher sweep.

It has to be noted that, despite the misplacement of the SCB the characteristics of the variable sweep optimization are better than those from the fixed sweep optimization, both for on- and off-design conditions. However, the fixed sweep optimizations were not allowed to fully convert, due to time constraints they were interrupted as soon as they reached MTOW reductions similar to those of the optimized variable sweep designs. This also showed that the fixed sweep optimizations required fewer iterations to reach an optimum of similar quality of the variable sweep optimizations.

The multi-point optimization aims to provide a more realistic result by incorporating the off-design performance in the analysis. Although this optimization was stopped before converging naturally (due to computation time constraints), the optimization was a success with a design achieving a MTOW reduction of 1.24% with a reduction in leading edge sweep angle of 11 degrees. The lift-to-drag ratio also showed improved performance at lower lift coefficients, relative to the optimized single-point designs.

The smaller optimized sweep angle for the multi-point optimizations seems to be due to the inclusion of the design point which has a lower lift coefficient, i.e. the smallest lift coefficient is the dominant factor in determining the possible sweep reduction. This can be concluded from the general trend from the analysis of the performance results: for each of the single-point optimized designs the lift-to-drag ratio is even higher for lift coefficient values larger than at the design point and the ratios at lower values of lift coefficient are increasingly worse compared to the baseline design.

Although the literature review showed that 3-D SCBs outperform 2-D SCBs in off-design performance, this cannot be verified by the results from these optimizations. Instead, the 2-D SCBs seem to outperform the 3-D SCBs for all optimized designs. This may be due to the fact that the viscosity effects and boundary layer effects are being ignored by the aerodynamic analysis. Another explanation could be the limitation in potential SCB shapes due to the lower bounds and limited number of control points that are being used for the 3-D SCB shapes. That the potential 3-D SCB shapes are limited is also evident from the efficacy of the sweep optimizations since the 3-D variant requires a greater amount of iterations than the 2-D SCB variant while reaching similar results.

The detrimental effects the secondary shock structures have on the boundary layer are not incorporated due to the Euler equations not including viscosity and boundary layer effects. This may be the reason why 2-D SCBs with significant flow re-acceleration are outperforming 3-D SCBs.

Because the performance of the optimized wings uniformly show improved aerodynamic performance beyond the design lift coefficient compared to the same wing without SCB, it can be concluded that optimizing for the lowest lift coefficient value results in better performance across the cruise phase. The optimized designs show drastically decreasing aerodynamic performance for lower lift coefficients than the design lift coefficient, when compared to the baseline wing. However, compared to the baseline wing, the designs which incorporate reduced wing sweep uniformly have reduced aerodynamic efficiency. This is the result of the structural wing weight contributing more to the MTOW reduction than the fuel weight, forcing the optimizer to focus on wing sweep reduction rather than improved aerodynamic performance. However, in reality it may be more appropriate to optimize more towards improved aerodynamic efficiency, i.e. improved fuel economy, dependent on the costs of fuel, the impact on the environment, and the effects on the direct operating costs.

7.2 Recommendations

After performing the optimizations of this research and having analysed the results, the following recommendations are made for future efforts on the topic of low sweep transonic wing design in combination with shock control bumps:

- Incorporate the effects of viscosity and the boundary layer during the aerodynamic analysis. In this research the CFD solver has been used to solve the Euler equations. However, the Euler equations are a simplified form of the NS equations and ignore both viscosity and boundary layer effects. By using the same CFD solver to instead solve the RANS equations the effects of viscosity and the boundary layer can be incorporated in the aerodynamic analysis.
- Increase the fidelity of the structural analysis by using a finite element based tool. The structural analysis tool that has been used for this research partly relies on empirical data. By upgrading the structural analysis tool to a finite element analysis based method, for example FEMWET [1], the accuracy of the weight estimation is improved. This could potentially be combined with the inclusion of aero-elasticity effects during the MDO.
- Upgrade SU² versions to enable switching from the continuous adjoint implementation to the discrete adjoint method. Due to issues with the continuous adjoint implementation in SU² the FDM had to be used for computing the gradient information with respect to the sweep variable. However, during the development of this thesis a newer version of SU² has been released which incorporates the discrete adjoint method. This discrete adjoint method is supposedly more robust and should be capable of providing accurate gradient information for variables such as the sweep angle as defined in this research.
- Combined with the previous recommendation, utilizing the discrete adjoint implementation in newer versions of SU², it is recommended to include more planform variables as design variables. This would, for example, allow the optimizer to maintain, or even improve, the ellipticity of the load distribution which would contribute to reducing the induced drag component. This would have to be combined with the use of the discrete adjoint method in order to avoid excessive use of the computationally expensive FDM for gradient information computation of these planform variables.
- Define the SCB shape parameterization in such a way that it is less restricting in terms of potential SCB shapes. This would allow for a much larger variation in shapes, including wedge shapes, which are currently not part of the design space due to the bounds on the SCB shape variables. It may even be worth it to investigate fixed SCB shapes which are sized by the optimizer, instead of designing arbitrary bump shapes during the optimization.
- Redefine the optimization to a multi-level optimization. Here, the top-level optimization focuses on optimizing the sweep angle, in terms of weight reduction, based on wave drag reductions provided by the low-level optimization. The low-level optimization focuses on SCB shape design at a given sweep angle, maximizing lift-to-drag ratio for a specific lift coefficient value.
- Switch from the local optimization algorithm to a global algorithm. By switching to a global algorithm, the computational cost of the optimization may increase drastically but the obtained optimum is more likely to be a global optimum and be of higher quality.

References

- [1] A. Elham and M. van Tooren, "Beyond Quasi-analytical Method for Preliminary Structural Sizing and Weight Estimation of Lifting Surfaces," Kissimmee, Florida, 2015.
- [2] M. Drela, "Development of the D8 Transport Configuration," in *29th AIAA Applied Aerodynamics Conference*, Honolulu, 2011.
- [3] European Commission, "Flightpath 2050 Europe's Vision for Aviation - Maintaining Global Leadership & Serving Society's Needs," European Union, 2011.
- [4] M. Brunet, R. Lafage, S. Aubry, A. Juniar and J. Catros, "The Clean Sky Programme: Environmental Benefits at Aircraft Level," in *AIAA*, Dallas, Texas, 2015.
- [5] R. Liebeck, D. Andrastek, J. Chau, R. Girvin, R. Lyon, B. Rawdon, P. Scott and R. Wright, "Advanced Subsonic Airplane Design & Economic Studies," National Aeronautics and Space Administration, Cleveland, Ohio, 1995.
- [6] P. Bruce and S. Colliss, "Review of Research into Shock Control Bumps," *Shock Waves*, vol. 25, no. 5, pp. 451-471, 2014.
- [7] T. Tai and D. Taylor, "Theoretical Aspects of Dromedaryfoil," Naval Air Systems Command, 1977.
- [8] T. Tai, G. Huson, R. Hicks and G. Gregorek, "Transonic Characteristics of a Humped Airfoil," *Journal of Aircraft*, vol. 25, no. 8, pp. 673-674, 1988.
- [9] P. Ashill, J. Fulker and A. Shires, "A Novel Technique for Controlling Shock Strength of Laminar-flow Aerofoil Sections," *DGLR Bericht*, vol. 6, pp. 175-183, 1992.
- [10] E. Stanewsky, J. Dlery, J. Fulker and P. de Matteis, "Drag Reduction by Shock and Boundary Layer Control," in *Notes on Numerical Fluid Mechanics and Multidisciplinary Design*, E. Stanewsky, J. Dlery, J. Fulker and P. de Matteis, Eds., Berlin, Heidelberg, Springer Berlin Heidelberg, 2002.
- [11] A. McGowan, "AVST Morphing Project Research Summaries in Fiscal Year 2001," NASA, Hampton, Virginia, 2002.
- [12] J. Eastwood and J. Jarrett, "Toward Designing with Three-dimensional Bumps for Lift/Drag Improvement and Buffet Alleviation," *AIAA Journal*, vol. 50, no. 12, pp. 2882-2898, 2012.
- [13] N. Qin, W. Wong and A. Le Moigne, "Three-dimensional Contour Bumps for Transonic Wing Drag Reduction," *Journal of Aerospace Engineering*, vol. 222, no. G5, pp. 619-629, 2008.
- [14] Y. Tao, G. Liu, Y. Wang and Z. Zhao, "On Drag Reduction Effect of Contour Bump of Supercritical Airfoil," Qingdao, 2013.
- [15] B. Yagiz, O. Kandil and Y. Pehlivanoglu, "Drag Minimization using Active and Passive Flow Control Techniques," *Aerospace Science and Technology*, vol. 17, no. 1, pp. 21-31, 2012.
- [16] S. Kim and D. Song, "A Numerical Analysis on Three-dimensional Flow Field in a Supersonic Bypass-type Inlet," *Journal of Mechanical Science and Technology*, vol. 21, no. 2, pp. 327-335, 2007.

- [17] K. Mazaheri, K. Kiani, A. Nejati, M. Zeinalpour and R. Taheri, "Optimization and Analysis of Shock Wave/Boundary Layer Interaction for Drag Reduction by Shock Control Bump," *Aerospace Science and Technology*, vol. 42, pp. 196-208, 2015.
- [18] P. Bruce and H. Babinsky, "Experimental Study into the Flow Physics of Three-dimensional Shock Control Bumps," *Journal of Aircraft*, vol. 49, no. 5, pp. 1222-1233, 2012.
- [19] P. Bruce, S. Colliss and H. Babinsky, "Three-dimensional Shock Control Bumps: Effect of Geometry," Maryland, 2014.
- [20] P. Bruce, S. Colliss, H. Babinsky, K. Nübler and T. Lutz, "An Experimental Investigation of Three-dimensional Shock Control Bumps applied to Transonic Airfoils," Nashville, 2012.
- [21] S. Colliss, H. Babinsky, K. Nübler and T. Lutz, "Joint Experimental and Numerical Approach to Three-dimensional Shock Control Bump Research," *AIAA Journal*, vol. 52, no. 2, pp. 436-446, 2014.
- [22] S. Colliss, H. Babinsky, K. Nübler and T. Lutz, "Vortical Structures on Three-dimensional Shock Control Bumps," Grapevine, 2013.
- [23] B. Knig, M. Paetzold, T. Lutz, E. Krämer, H. Rosemann, K. Richter and H. Uhlemann, "Numerical and Experimental Validation of Three-dimensional Shock Control Bumps," *Journal of Aircraft*, vol. 46, no. 2, pp. 675-682, 2009.
- [24] K. Nübler, S. Colliss, T. Lutz, H. Babinsky and E. Krämer, "Numerical and Experimental Examination of Shock Control Bump Flow Physics," in *High Performance Computing in Science and Engineering '12*, W. Nagel, D. Kröner and M. Resch, Eds., Berlin, Heidelberg, Springer Berlin Heidelberg, 2012, pp. 333-349.
- [25] W. Wong, N. Qin, N. Sellars, H. Holden and H. Babinsky, "A Combined Experimental and Numerical Study of Flow Structures over Three-dimensional Shock Control Bumps," *Aerospace Science and Technology*, vol. 12, no. 6, pp. 436-447, 2008.
- [26] S. Kim and D. Song, "Numerical Study on Performance of Supersonic Inlets with Various Three-dimensional Bumps," *Journal of Mechanical Science and Technology*, vol. 22, no. 8, pp. 1640-1647, 2009.
- [27] J. Birkemeyer, H. Rosemann and E. Stanewsky, "Shock Control on a Swept Wing," *Aerospace Science and Technology*, vol. 4, no. 3, pp. 147-156, 2000.
- [28] H. Ogawa, H. Babinsky, M. Paetzold and L. T., "Shock-wave/Boundary-layer Interaction Control using Three-dimensional Bumps for Transonic Wings," *AIAA Journal*, vol. 46, no. 6, pp. 1442-1452, 2008.
- [29] B. König, M. Pätzold, T. Lutz and E. Krämer, "Numerical and Experimental Validation of Three-Dimensional Shock Control Bumps," *Journal of Aircraft*, vol. 46, no. 2, pp. 675-682, 2009.
- [30] H. Ogawa and H. Babinsky, "Wind-tunnel Setup for Investigations of Normal Shock Wave/Boundary Layer Interaction Control," *AIAA Journal*, vol. 44, no. 11, pp. 2803-2805, 2006.
- [31] W. Milholen and L. Owens, "On the Application of Contour Bumps for Transonic Drag Reduction," 2005.
- [32] N. Qin, "Drag Reduction for Transonic Wings combining Reduced Wing Sweep with Shock Control," in *28th International Symposium on Shock Waves: Vol 1*, K. Kontis, Ed., Berlin, Heidelberg, Springer Berlin Heidelberg, 2012, pp. 45-53.

- [33] F. Deng, N. Qin, X. Liu, X. Yu and N. Zhao, "Shock Control Bump Optimization for a Low Sweep Supercritical Wing," *Science China Technological Sciences*, vol. 56, no. 10, pp. 2385-2390, 2013.
- [34] D. Howe, "Aircraft Conceptual Design Synthesis," London, Professional Engineering Publishing Limited, 2000, pp. 158-159.
- [35] F. Palacios, J. Alonso, K. Duraisamy, M. Colonno, J. Hicken, A. Aranake, A. Campos, S. Copeland, T. Economon, A. Lonkar, T. Lukaczyk and T. Taylor, "Stanford University Unstructured: An Open-source Integrated Computational Environment for Multi-physics Simulation and Design," Grapevine, Texas, 2013.
- [36] C. Castro, C. Lozano, F. Palacios and E. Zuazua, "A Systematic Continuous Adjoint Approach to Viscous Aerodynamic Design on Unstructured Grids," *AIAA Journal*, vol. 45, no. 9, pp. 2125-2139, 2007.
- [37] Z. Lyu, G. Kenway, C. Paige and J. Martins, "Automatic Differentiation Adjoint of the Reynolds-averaged Navier-Stokes Equations with a Turbulence Model," in *21st AIAA Computational Fluid Dynamics Conference*, San Diego, CA, 2013.
- [38] P. Ashill, J. Fulker and M. Simmons, "Simulated Active Control of Shock Waves in Experiments on Aerofoil Models," in *Second International Conference on Experimental Fluid Mechanics*, Turin, Italy, 1994.
- [39] J. Samarah, "Aerodynamic Shape Optimization Based on Free-form Deformation," in *10th AIAA/ISSMO Multidisciplinary Analysis and Optimization Conference*, Albany, 2004.
- [40] T. Sederberg and S. Parry, "Free-form Deformation of Solid Geometric Models," *Proceedings of SIGGRAPH 89 (Computer Graphics)*, vol. 20, no. 4, pp. 151-159, 1986.
- [41] H. Gagnon and D. Zingg, "Two-Level Free-Form Deformation for High-Fidelity Aerodynamic Shape Optimization," *AIAA Journal*, vol. 53, no. 7, pp. 2015-2026, 2015.
- [42] J. Hicken and D. Zingg, "Aerodynamic Optimization Algorithm with Integrated Geometry Parameterization and Mesh Movement," *AIAA Journal*, vol. 48, no. 2, pp. 400-413, 2010.
- [43] F. Palacios, T. Economon, T. Carrigan and T. Lukaczyk, "Supersonic Aircraft Shape Design Powered by SU2 and Pointwise," 29 April 2015. [Online]. Available: http://su2.stanford.edu/documents/Pointwise-Stanford-Webinar-Slides_20140429.pdf. [Accessed 31 October 2016].
- [44] F. Zhu and N. Qin, "Using Mesh Adjoint for Shock Bump Deployment and Optimisation on Transonic Wings," Kissimmee, Florida, 2015.
- [45] T. Economon, F. Palacios and J. Alonso, "An Unsteady Continuous Adjoint Approach for Aerodynamic Design on Dynamic Meshes," in *15th AIAA/ISSMO Multidisciplinary Analysis and Optimization Conference*, Atlanta, 2014.
- [46] F. Palacios, T. Economon, J. Alonso and A. Wendorff, "Large-scale Aircraft Design using SU2," Kissimmee, Florida, 2015.
- [47] A. Elham, G. La Rocca and M. van Tooren, "Development and Implementation of an Advanced, Design-sensitive Method for Wing Weight Estimation," *Aerospace Science and Technology*, vol. 29, pp. 100-113, 2013.

- [48] M. Torenbeek, "Development and Application of a Comprehensive, Design Sensitive Weight Prediction Method for Wing Structures of Transport Category Aircraft," Delft University of Technology, Delft, Netherlands, 1992.
- [49] J. Roskam, *Airplane Design*, Kansas: DARcorporation, 1985.
- [50] M. Bartholomew-Biggs, S. Brown, B. Christianson and L. Dixon, "Automatic Differentiation of Algorithms," *Journal of Computational and Applied Mathematics*, vol. 124, no. 1-2, pp. 171-190, 2000.
- [51] R. Martins and B. Lambe, "Multidisciplinary Design Optimization: A Survey of Architectures," *AIAA Journal*, vol. 51, no. 9, pp. 2049-2075, 2013.
- [52] A. Lambe and J. Martins, "Extensions to the Design Structure Matrix for the Description of Multidisciplinary Design, Analysis, and Optimization Processes," *Structural and Multidisciplinary Optimization*, vol. 46, no. 2, pp. 273-284, 2012.
- [53] D. Steward, "The Design Structure Matrix: A Method for Managing the Design of Complex Systems," *IEEE Transactions on Engineering Management*, vol. 28, pp. 71-74, 1981.
- [54] T. Browning, "Applying the Design Structure Matrix to System Decomposition and Integration Problems: A Review and New Directions," *IEEE Transactions on Engineering Management*, vol. 48, no. 3, pp. 292-306, 2001.
- [55] R. Haftka, "Simultaneous Analysis and Design," *AIAA Journal*, vol. 23, no. 7, pp. 1099-1103, 1985.
- [56] E. Cramer, J. Dennis Jr, P. Frank, R. Lewis and G. Shubin, "Problem Formulation for Multidisciplinary Optimization," *SIAM Journal on Optimization*, vol. 4, no. 4, pp. 754-776, 1994.
- [57] N. Alexandrov and R. Lewis, "Analytical and Computational Aspect of Collaborative Optimization for Multidisciplinary Design," *AIAA Journal*, vol. 40, no. 2, pp. 301-309, 2002.
- [58] I. Kroo, "MDO for Large-Scale Design," in *Multidisciplinary Design Optimization: State-of-the-Art*, SIAM, 1997, pp. 22-44.
- [59] R. S.-S. J. Balling, "Optimization of Coupled Systems: A Critical Overview of Approaches," *AIAA Journal*, vol. 34, no. 1, pp. 6-17, 1996.
- [60] E. Cramer, J. Dennis, P. Frank, R. Lewis and G. Shubin, "Problem Formulation for Multidisciplinary Optimization," *SIAM Journal on Optimization*, vol. 4, no. 4, pp. 754-776, 1994.
- [61] J. Hoogervorst, "Wing Aerostructural Optimization using the Individual Discipline Feasible Architecture," Delft, 2016.
- [62] P. Boggs and J. Tolle, "Sequential Quadratic Programming for Large-scale Nonlinear Optimization," *Journal of Computational and Applied Mathematics*, vol. 124, pp. 123-137, 2000.
- [63] E. Obert, *Aerodynamic Design of Transport Aircraft*, Delft: Delft University Press, 2009.
- [64] "Jane's All the Worlds Aircraft: Development & Production," IHS, [Online]. Available: <https://janes.ihs.com>. [Accessed 07 November 2016].
- [65] B. Timmer and A. Elham, "Aerostructural Optimization of a Low Sweep Transonic Wing with Shock Control Bump," in *AIAA*, San Diego, California, 2016.
- [66] StanfordUniversity, "SU2 - The Open-source CFD Code," 2016. [Online]. Available: <https://github.com/su2code/SU2/wiki>. [Accessed 11 April 2016].

- [67] F. Palacios, J. Alonso, K. Duraisamy, A. Aranake, S. Copeland, T. Economon, A. Lonkar, T. Lukaczyk, K. Naik and S. Padron, "Stanford University Unstructured (SU2): Analysis and Design Technology for Turbulent Flows," National Harbor, Maryland, 2014.
- [68] S. Kim, "Aerodynamic Design of a Supersonic Inlet with a Parametric Bump," *Journal of Aircraft*, vol. 46, no. 1, pp. 198-202, 2009.
- [69] European Commission, "Flightpath 2050 Europe's Vision for Aviation," Publications Office of the European Union, Luxembourg, 2011.
- [70] A. Elham, "Weight Indexing for Multidisciplinary Design Optimization of Lifting Surfaces," 2014.
- [71] A. Elham and M. van Tooren, "Coupled Adjoint Aerostructural Wing Optimization Using Quasi-three-dimensional Aerodynamic Analysis," Dallas, Texas, 2015.
- [72] A. Elham, "Adjoint Quasi-three-dimensional Aerodynamic Solver for Multi-fidelity Wing Aerodynamic Shape Optimization," *Aerospace Science and Technology*, vol. 41, pp. 241-249, 2015.
- [73] T. Economon, F. Palacios, J. Alonso, G. B. Bansal, D. Mudigere, A. Deshpande, A. Heinecke and M. Smelyanskiy, "Towards High-performance Optimizations of the Unstructured Open-source SU2 Suite," Kissimmee, Florida, 2015.
- [74] M. Drela and M. Giles, "Viscous-inviscid Analysis of Transonic and Low Reynolds Number Airfoils.," *AIAA*, vol. 25, no. 10, pp. 1347-1355, 1987.
- [75] M. Drela, "Pros and Cons of Airfoil Optimization," in *Frontiers of Computational Fluid Dynamics*, D. Caughey and M. Hafez, Eds., Singapore, World Scientific, 1998, pp. 363-380.
- [76] M. Drela, "Multi-element Airfoil Design/Analysis Software - Summary," 1994. [Online]. Available: raphael.mit.edu/drela/msessum.ps. [Accessed 19 June 2015].
- [77] A. Jameson and S. Kim, "Reduction of the Adjoint Gradient Formula for Aerodynamic Shape Optimization Problems," *AIAA Journal*, vol. 41, no. 11, pp. 2114-2129, 2003.
- [78] W. Anderson and V. Venkatakrishnan, "Aerodynamic Design Optimization on Unstructured Grids with a Continuous Adjoint Formulation," in *35th AIAA Aerospace Science Meeting & Exhibit*, Reno, 1997.
- [79] G. Ruijgrok and D. van Paassen, *Elements of Aircraft Polution*, Delft University Press, 2005.
- [80] M. Drela and H. Youngen, "AVL (Athena Vortex Lattice) 3.26," Massachusetts Institute of Technology, 2006.
- [81] M. Drela and H. Youngren, "XFOIL: Subsonic Airofil Development System," Massachusetts Institute of Technology, [Online]. Available: <http://web.mit.edu/drela/Public/web/xfoil/>. [Accessed October 2016].
- [82] "VGK Method for Two Dimensional Aerofoil Sections, Technical Report 69028," ESDU, 1996.
- [83] J. Hoogervorst, "Wing Aerostructural Optimization using the Individual Design Feasible Architecture," Delft University of Technology, Delft, 2016.